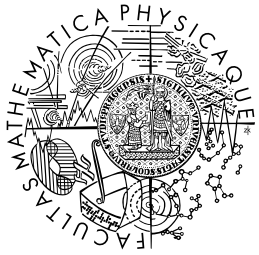

FACULTY
OF MATHEMATICS
AND PHYSICS
Charles University

DOCTORAL THESIS

João Pedro Martins Godinho

Electro and thermal magnetotransport in antiferromagnetic systems

Institute of Physics of the Czech Academy of Sciences

Supervisor of the doctoral thesis: prof. Jörg Wunderlich

Study programme: Physics

Study branch: Physics of Nanostructures and Nanomaterials

Prague 2023

I declare that I carried out this doctoral thesis independently, and only with the cited sources, literature and other professional sources. It has not been used to obtain another or the same degree.

I understand that my work relates to the rights and obligations under the Act No. 121/2000 Sb., the Copyright Act, as amended, in particular the fact that the Charles University has the right to conclude a license agreement on the use of this work as a school work pursuant to Section 60 subsection 1 of the Copyright Act.

In ..... date ....

Author's signature

This is the conclusion of a long and arduous journey, made possible by the many people I have met along the way. Here, I do hope to acknowledge and thank everyone who helped me throughout my doctoral studies.

Firstly, I would like to show my gratitude to prof. Jörg Wunderlich for taking me as a Ph.D. student and entrusting me with the different projects I worked on. Thank you for your constant support, guidance and readiness to talk and discuss.

A great thanks also goes to the whole group of prof. Tomáš Jungwirth at the Institute of Physics at the Academy of Sciences in Prague, who significantly contributed to the success of this work. I have greatly benefited from the individual expertise within the group. Also my gratitude to everyone in the group regarding the help with any administrative process for which my Czech skills were not enough. I would like to acknowledge who, besides my supervisor, advised me during my Ph.D. work - Tomáš Jungwirth, Vít Novák and Kamil Olejník. Kamil, thank you for your patience every time I would go to your office with "I have one question".

To Helena Reichlová and Dominik Kriegner, for all your tireless help during the beginning of the Ph.D. and your support with my first publication, a special thank you.

I want to thank Zbyněk Šobáň for fabricating most of the devices I measured and his availability to always help solving any issue I ran into in the labs; Rubén Otxoa for his help on simulating the dynamics of antiferromagnetically coupled systems, as well as for providing me with a license for Mathematica to run the simulations; Jakub Železný and Jungwoo Koo for the insightful discussions on symmetries.

I am particularly grateful to Eva Matuszná for all the help with paperwork and most importantly her friendship. Eva, thank you for always being supportive and cheerful and for the small non-physics related discussions over coffee / tea breaks. A special mention also goes to Milan Mašek, Tomáš Janda and Pradeep Kumar Rout for all their help and friendship.

To my friends Almeno Fernandes, André Cunha, André Farinha, Bruno Morais and Daniel Magro, even though scattered around Europe, thank you for the company throughout all this time and the emotional support. Obrigado patos.

Por fim, gostaria de deixar um especial obrigado à minha família, aos meus pais e aos meus avós Rosalina e Francisco. Obrigado por todo o apoio.

Title: Electro and thermal magnetotransport in antiferromagnetic systems

Author: João Pedro Martins Godinho

Department: Institute of Physics of the Czech Academy of Sciences

Supervisor: prof. Jörg Wunderlich, Institute of Physics of the Czech Academy of Sciences

Abstract:

How to electrically identify the Néel vector reversal in $\mathcal{PT}$ symmetric systems? The detection of magnetic order reversal has been one open problem in antiferromagnetic spintronics. More so, in systems like the tetragonal CuMnAs which preserve the combined $\mathcal{PT}$ symmetry, since the combined $\mathcal{PT}$ symmetry renders odd magnetoresistance effects such as the anomalous Hall effect to be zero. This thesis focuses on trying to provide an answer to the question above. We present the measurement of second-order magnetotransport effects as a mechanism to identify the reversal of the Néel order. We show it in two different systems, firstly on an out-of-plane synthetic antiferromagnet and later in the tetragonal CuMnAs. We also introduce a scanning thermal gradient microscopy which allows us to exploit different thermoelectric effects depending on the symmetries of the chosen material. For instance, in the collinear CuMnAs we take advantage of the magneto-Seebeck effect to image changes in the magnetic structure due to the application of electrical current pulses. In the case of the noncollinear antiferromagnetic Mn_3Sn, the anomalous Nernst response is used to map the magnetic order.

Keywords: Antiferromagnetic spintronics, $\mathcal{PT}$ symmetric systems, Second-order magnetotransport effects, Scanning thermal gradient microscopy

Contents

1. Motivation and Goals

The field of spin transport electronics, or spintronics for short, aims to bring new functionalities to electronic devices by taking advantage of the electron's magnetic moment.

The spin is a quantum property of elementary particles and represents an intrinsic angular momentum. In quantum mechanics, there are two angular momentum types: orbital angular momentum and intrinsic angular momentum. The first corresponds to the classical mechanics' counterpart. Despite the fact that the latter has no analog in classical mechanics, it is often associated with a rotation of the particle around some axis. Thus, it has been known as spin. In classical electrodynamics, a rotating electrical charge induces a magnetic dipole moment. Similarly, the electron possesses a nonzero magnetic moment due to its intrinsic angular momentum and electrical charge. The quantization of angular momentum was demonstrated in experiments like the Stern-Gerlach, and the existence of intrinsic momentum was proposed by Uhlenbeck and Goudsmit in 1926. They inferred the two possible quantized values of the electron's spin, and thereby nowadays we say its spin quantum number is 1/2.

Spintronics might be described as the attempt to use the spin of the electron in addition to or even instead of its electric charge. Technologically, exploiting the electron's spin brings two main advantages. Firstly, for memory applications, the information can be stored in the magnetic moment, which is non-volatile. Secondly, the notion of a pure spin current is interesting since it can transport information without Joule dissipation.

The first breakthrough that established the spintronics field was the development of magnetoresistive read heads in magnetic hard drives. Such technology was based on the 1988 discovery of giant magnetoresistance (GMR) by Albert Fert and Peter Grünberg. For their discovery, they were awarded the Physics Nobel prize in 2007. Also noteworthy was the discovery of spin-transfer torque (STT) in 1996 by Luc Berger and John Slonczewski. This phenomenon led to the development of magnetic random access memories (MRAM). An MRAM memory cell consists of a spin-valve device, two ferromagnetic layers separated by a spacer layer, where both operations, reading and writing, are realized by electrical currents of different magnitudes. For instance, the reading could be done with GMR and the writing with STT.

Spintronic devices have traditionally only relied on ferromagnetic (FM) materials as the active element. On the other hand, antiferromagnets (AFM) were only used to stabilize a reference layer via the exchange bias between an AFM and an FM layer. This narrow view of the possible applications of AFM has recently broadened, and a new subfield of spintronics has emerged - antiferromagnetic spintronics. The advantages brought by this class of magnetic materials include faster dynamics, almost no response to external magnetic perturbations, and their lack of stray fields. These are all highly sought-after properties for storage applications. However, the rigidity offered by this type of magnetic order is a double-edged sword. From a memory application point of view, it makes the memory cells more robust against external fields, but at the same time, it hinders the manipulation of the magnetic order or the process of writing new

information. The manipulation of the antiferromagnetic order with an external field would require a strong field of up to several Tesla. This hurdle has delayed the use of AFM as the main element in spintronic devices.

In 2014, it was proposed that in a collinear antiferromagnetic crystal with its two magnetic sublattices sitting at locally non-centrosymmetric lattice sites, an electrical current would induce a staggered effective field [1]. The resulting field offers an efficient way to manipulate the AFM order due to its staggered nature, which means that the induced field alternates between magnetic sublattices. Two years later, the first demonstration of electrical manipulation of AFM order was shown in the semimetallic AFM CuMnAs, highlighting the functionality of an AFM memory cell [2]. Later it has also been verified in the metallic AFM Mn_2Au [3]. While the writing is achieved via the spin-orbit torque, the readout is done by measuring the change in resistance. This change comes from the re-orientation of the magnetic moments, which, due to the anisotropic magnetoresistance (AMR), modifies the device's resistance.

From a technological standpoint, using the AMR as a readout has a significant drawback. Compared to traditional spintronic devices such as magnetic tunnel junctions, the readout signal is much smaller. Secondly, from a more academic perspective, the AMR is even in magnetization; therefore, the AMR alone can detect the axis defined by the AFM moments but not their direction. The same issue also occurs for the most used technique for imaging AFM, X-ray magnetic linear dichroism (XMLD). The detection of magnetic order reversal has been one open problem in AFM spintronics. More so, in systems like the tetragonal CuMnAs which preserve the combined $\mathcal{PT}$ symmetry. In order to identify reversed magnetic states, we need an odd effect in magnetization. The most commonly used is the anomalous Hall effect (AHE). However, when the $\mathcal{PT}$ symmetry is present the anomalous Hall response is zero.

How to electrically identify the Néel vector reversal in $\mathcal{PT}$ symmetric systems?

The work carried out during this Ph.D. thesis mainly addresses the detection of the antiferromagnetic order employing electrical and thermoelectrical methods. It focuses on trying to provide an answer to the question above, and on thermally imaging changes in the magnetic structure due to the application of electrical current pulses.

This thesis consists of six parts. After the brief motivation, the next chapter addresses basic concepts of magnetism and the manipulation of magnetic moments. The third chapter is dedicated to magnetotransport. In it, we review the relevant magnetoresistance effects and their thermal counterpart. In chapter number four, we present the systems used throughout this work. At the center of this work is the tetragonal CuMnAs. We go over the work done on this material and discuss the main findings. Neither the manipulation nor the detection of the antiferromagnetic order is as accessible as in ferromagnets, and thereby working with them is challenging. Thus we propose a multilayered system, comprising a synthetic antiferromagnet (SAF) in-between two Pt layers as a CuMnAs model system. High tunability is one of the major advantages of a SAF system. We can choose the respective composition and thickness of individual layers. And with it, we may fine-tune the net moment, anisotropy and exchange strengths.

Furthermore, it is still possible to grow heavy metal layers bordering the ferromagnets on the SAF, so that there is a staggered spin accumulation. Therefore, these systems are a good candidate to study effects present in AFM, while its manipulation via external means is still easily achievable due to weaker exchange interactions. In last, we also present the Mn_3Sn and the class of noncollinear antiferromagnets. This is an interesting class of materials that harness properties usually associated with ferromagnets and antiferromagnets. Even with a zero magnetization, or a vanishing small one, effects such as AHE and spin-polarized currents are expected in these systems.

The key results obtained during the Ph.D. work are summarized in the fifth chapter. We start by describing the higher-order magnetoresistance term and we argue that exploiting such nonlinear responses might be one possible answer to the core question. That is, the nonlinear response of the even AMR effect can detect the reversal of the Néel order. We initially demonstrate it in the SAF and later apply the same concept to the bulk AFM CuMnAs.

The last two sections of chapter five are dedicated to imaging the antiferromagnetic magnetic order. We present a scanning thermal gradient microscopy, where a local thermal gradient probes the local magnetic structure and develops a net global voltage. Two different methods to generate the local thermal gradient are shown. One using a far-field and the second a near-field optical microscope. Once we are able to generate a local thermal gradient in our samples, we can exploit different thermoelectric effects in order to image the magnetic order. The $\mathcal{PT}$ symmetry in CuMnAs prevents the AHE response, and likewise, the thermal counterpart anomalous Nernst effect (ANE) is also zero. Hence, we propose the magneto-Seebeck effect as a mechanism to probe the domain walls in CuMnAs, and their motion after applying electrical pulses. The near-field optical microscopy method is used to investigate the narrow 180° domain walls on a CuMnAs film with uniaxial anisotropy. Despite its negligible net moment, the finite Berry curvature allowed by the broken $\mathcal{PT}$ symmetry in Mn_3Sn gives rise to a nonzero ANE response. By recording the ANE voltage while scanning the thermal gradient over the sample, we can image the distribution of magnetic domains. Finally, we also show that by combining a laser beam with higher power and an external field, we can set a magnetic pattern at will via heat-assisted writing.

To wrap up, we conclude with an outlook and a conclusion chapter. The outlook chapter offers a forward-looking perspective by outlining possible future experiments that could extend and build upon the presented results. The concluding chapter, on the other hand, offers a reflective summary of the work's main findings.

2. Manipulation of Magnetic Moments

2.1 Magnetic Moments

In classical electromagnetism the magnetic field is generated due to motion of charged particles, as described in Biot-Savart Law. Shortly after Biot and Savart, Ampere suggested that the magnetic moment in matter is correlated with current loops within the material. The resulting magnetic field of a current loop, resembles the electric field of an electric dipole. Thus, a current loop is associated with a magnetic dipole. The magnetic moment μ will be proportional to the current and the area enclosed by the loop, or $\mu = IA$. Since the electrons that generate the current are particles with mass, it is usual to correlate the dipole moment with the angular momentum. These two quantities are then proportional and expressed as:

$$\mu = \gamma L \ , \tag{2.1}$$

γ is the gyromagnetic ratio connecting the magnetic moment to the angular momentum L. This relation has been proven by the experiment of Einstein-de Haas.

When in a uniform magnetic field, a magnetic dipole behaves differently compared to the electric counterpart. An electric dipole in an uniform electric field experiences a zero net force, since the electric force acting on the two charged particles cancel out. Hence, its center of mass does not accelerate. However, there is a net torque that aligns the dipole along with the field. In the magnetic case, when integrating the magnetic force along the particle's orbit, it also averages to zero. The torque however, will act differently. While the electric force points along the electric field, the magnetic force points perpendicular to the magnetic field. Recall that the electromagnetic force acting on a charge particle is given by:

$$F = q\left(E + v \times B\right) \ . \tag{2.2}$$

As a consequence, instead of aligning along the magnetic field the magnetic dipole will precess around it. The torque is given by $\tau = \mu \times B$, and recalling equation 2.1 and that $\tau = \frac{\mathrm{d}L}{\mathrm{d}t}$, then:

$$\frac{\mathrm{d}\mu}{\mathrm{d}t} = \gamma\mu \times B \ . \tag{2.3}$$

Here, it becomes clear that the magnitude of μ does not change but only its direction. The energy of the dipole moment is:

$$E = -\mu \cdot B \ . \tag{2.4}$$

In atoms the total magnetic moment is determined by the total angular momentum of its electrons. The total angular momentum of an electron bound to an atom has two contributions. The first, which is intuitive from a classical approach is the orbital angular momentum. In other words, it is due to the periodic motion around the nucleus. The second contribution is the intrinsic angular momentum, or spin. It was first proposed by Uhlenbeck and Goudsmit in 1925 and three

years later its relativistic and quantum nature was shown in Dirac's equation. In hindsight, Stern-Gerlach experiment was the first experiment demonstrating the electron's spin. Its correct explanation only came later.

The expressions classically derived correspond to the orbital angular momentum and also hold for the spin angular momentum. However, the spin gyromagnetic ratio is approximately twice as large. This result can only be explained in a quantum relativistic model.

At a macroscopic scale, the magnetization M of a given material is the vector sum of the magnetic moments over the material's volume. Despite useful, this quantity should not be the only deciding factor to determine if a given material is magnetic. The total magnetization might average to zero even though there is magnetic order in the material. For instance, a ferromagnetic material which is divided into multiple magnetic domains; or if we are in presence of a antiferromagnetic material where the magnetization is vanishing small or zero. A better description of the different magnetic orders will be given in the next chapter. An additional possible case for a perceived zero magnetization is a temperature above the critical temperature. That is, when the thermal fluctuations are strong enough to fully randomize the magnetic order.

2.2 LLG equation

For now we will consider a ferromagnet, whose magnetization is saturated, meaning that there is only one single magnetic domain. Here we can describe the magnetic order as one global magnetization vector, M. The focus of this chapter is on how to manipulate this magnetic moment.

The most intuitive way to control the magnetic order is via external magnetic fields. When in the presence of a magnetic field, the magnetization vector behaves similar to the magnetic dipole previously described. The equation 2.3 is then modified to:

$$\frac{\mathrm{d}M}{\mathrm{d}t} = \gamma\mu_0 M \times H \ , \tag{2.5}$$

where μ_0 denotes the vacuum permeability and H is the field strength. As before for the magnetic dipole case, similarly here the magnetization vector indefinitely precesses around the field with a constant energy of $E_{zee} = -\mu_0 M \cdot H$. This energy term coupling the magnetization with an applied magnetic field is also known as Zeeman energy.

Besides an external field, there are "effective" magnetic fields within the material. The "built-in" fields reflect the crystal field environment and the sample structure. These fields add to the external field to a total effective field around which the magnetization will precess. Here, we will draw attention to two phenomena, anisotropy and exchange interaction.

The main type of anisotropy is the magneto crystalline anisotropy which reflects the crystal symmetry. This term describes the preferred axes for the magnetization to point along. In a simple uniaxial anisotropy, the energy term associated with it can be expressed by:

$$E_a = -VK\left(u \cdot m\right)^2 \ , \tag{2.6}$$

where $m = M/|M|$ denotes the magnetization direction, V material's volume, K is the anisotropy constant and u is the easy-axis direction. This same expression also describes an easy-plane anisotropy when $K < 0$, where u is the vector normal to the easy plane.

The ferromagnet produces its own magnetic field at its boundaries, as the divergence of the magnetization $\nabla \cdot M$ acts as a sink or source of magnetic field lines. This field is known as stray field and the magnetization interacts with it via the Zeeman term. There are two main mechanisms to achieve a minimization of the Zeeman energy of this interaction. One option is to break the single magnetic domain into multiple domains oriented along different directions. In doing so, the total magnetization of the sample decreases and consequently the stray field also weakens. This is the reason multidomain states are observed in ferromagnetic materials and why this field is also called demagnetizing field. The second is to favor the magnetization to lie along certain directions that minimize the total interaction between the stray field and the magnetization. In other words, it acts as another source of magnetic anisotropy that depends on the geometry of the sample, and thus it is known as shape anisotropy. This contribution is of special relevance for thin films applications, as in such geometry the shape anisotropy favors an in-plane magnetization.

A third source of anisotropy is the magnetostriction effect. This phenomenon couples the strain (or stress) of the material and its magnetization. When under stress, the unit cell deforms and this displacement influences the electronic bonds between neighboring atoms which can in turn change the magnetic anisotropy of the material. In thin films, this effect might introduce an additional anisotropy when the magnetic layers grows on top of a material with a significant lattice mismatch.

As mentioned above, the magnetocrystalline anisotropy arises from the crystal symmetry. However, at the surface or interface of the crystal where the symmetry is broken, new anisotropy terms may arise. Since it is an interfacial effect, it is only relevant for samples with a small volume to surface ratio. The interfacial anisotropy can be engineered by tuning the layer's thickness and the material grown next to the ferromagnet. Exploiting this phenomenon, it is possible to compete against the shape anisotropy and observe out-of-plane easy axis in thin films samples.

Exchange interaction is the phenomenon behind the long range magnetic order. The dipole-dipole interaction between two electrons can be estimated to be equivalent to 1 K in temperature. With materials exhibiting magnetic order up to temperatures several orders of magnitude higher, the magnetic dipole interaction is too weak to explain such observations. Instead, the exchange interaction is the mechanism responsible for the magnetic order. It is purely a quantum effect with no classical counterpart arising from the Coulomb interaction and Pauli exclusion principle. If the interaction between two electrons happens without the need for an intermediary it is called a direct exchange, and indirect exchange otherwise. The general way to describe this interaction is via the following energy expression:

$$E_{ex} = -2Jm_1 \cdot m_2 \ , \tag{2.7}$$

where m_i denote the two magnetic moments and J denotes the strength of the interaction, also known as exchange constant or exchange integral. The sign

of J defines a parallel or antiparallel arrangement, hence the two moments are ferromagnetically or antiferromagnetically coupled.

Among the family of exchange interactions, we will briefly describe two observable interactions in multilayers systems. Broadly used in technological applications, coupling together a ferromagnetic and an antiferromagnetic layers results in the exchange bias. This phenomenon was discovered by Meiklejohn and Bean when studying ferromagnetic cobalt particles covered by antiferromagnetic cobalt oxide [4]. They realized that the hysteresis loop is shifted, not being centered around zero anymore. It can be said that the antiferromagnet is providing an exchange field to the ferromagnet, an extra field that adds to the external field. This effect has been exploited to stabilize the magnetization and pin a reference layer in spin-valve devices. The second phenomenon is an indirect exchange interaction in metals mediated by conduction electrons known as RKKY interaction. It is named after Ruderman, Kittel, Kasuya and Yosida who proposed and developed the model. The model describes the oscillations observed between the ferro and antiferromagnetic coupling of two ferromagnetic multilayers as a function of the distance between them. This effect is of special interest when tuning the thickness of the spacer layer between two ferromagnets such that an antiferromagnetic coupling is favored, and hence the overall system behaves as a ferri or antiferromagnet. These multilayer structures are called synthetic antiferromagnets. Alternatively to exchange bias, synthetic antiferromagnets are also used as reference layers in spintronic devices.

The exchange interaction does not have to uniquely promote adjacent moment to be collinear, either parallel or antiparallel to each other. Crystals with low symmetry may exhibit Dzyaloshinski-Moriya interaction, or DMI for short [5, 6]. This interaction is quite particular for favoring an orthogonal configuration of the moments. It is an indirect interaction mediated by non-magnetic atoms, which can take place in bulk or be induced at the interfaces. It can be expressed by:

$$E_{DMI} = -D \cdot (m_1 \times m_2) \ , \tag{2.8}$$

where the vector D is defined by the crystal symmetry. This rather weak effect is responsible for the weak ferromagnetism, the presence of a small net magnetic moment in antiferromagnets. Furthermore, it gives a sense of chirality to the magnetic system and it is behind the intensively studied topological structures in ferromagnets such as skyrmions [7].

The equation 2.5 only took into account the Zeeman interaction. In order to consider all the interactions described above, the equation can be modified where the field H is replaced by an effective field H_{eff} comprising all the interactions. Thus, we have:

$$\begin{aligned} \mu_0 H_{eff} &= -\frac{\partial E}{\partial M} \\ E &= E_{zee} + E_a + E_{ex} + E_{DMI} + ... \end{aligned} \tag{2.9}$$

where E denotes the total energy of the system, and hence the dynamics equation now reads:

$$\frac{\mathrm{d}M}{\mathrm{d}t} = \gamma \mu_0 M \times H_{eff} \ . \tag{2.10}$$

From experience, we know that when subjected to a field the magnetization ends up aligning with it instead of indefinitely precessing around it. For instance,

with a strong enough field a ferromagnet can be saturated, meaning that all magnetic domains point in the same direction as the field. Thus, the equation 2.10 is missing a term which over time aligns both vectors M and H_{eff}. With it, the equation becomes:

$$\frac{\mathrm{d}M}{\mathrm{d}t} = \gamma\mu_0 M \times H_{eff} - \alpha m \times \frac{\mathrm{d}M}{\mathrm{d}t} \ . \tag{2.11}$$

The second term, the dissipative term was added in a phenomenological way where α is the damping parameter or Gilbert damping. The damping parameter comprises all mechanisms through which the system can dissipate energy. Under a more extensive analysis it can be decomposed into intrinsic and extrinsic mechanisms. The former being material specific such as spin-orbit interaction and dissipation into the crystal lattice via phonons. Meanwhile, the latter depends on the particular sample under study, with for example interfacial contributions and lattice defects.

The equation 2.11 is the well known Landau-Lifshitz-Gilbert (LLG) equation. It is widely used on the field of micromagnetic simulations in order to study the effect of an external field on a magnetic material. Throughout the literature this expression might be written differently where the damping term is written $\lambda m \times (M \times H_{eff})$, which in that case is often referred to as the Landau-Lifshitz (LL) equation. This alternative is particularly advantageous when numerically solving the equation.

2.3 Spin-Transfer Torque

So far we have seen how an external magnetic field can manipulate the magnetization vector and how to describe such dynamics. Such an approach is not ideal for practical applications though. For instance with magnetic memories in mind, a global external field would act on all memory cells simultaneously, rendering the multi-bit memory into a single-bit. Instead of a global field, a more localized field can be generated by a local electrical current, that is an Oersted field. Despite this generated field being localized and close to the memory cell, this approach still faces a twofold problem. It restricts the memory density by setting a minimum distance between bits such that the Oersted field does not affect neighboring cells. Secondly, the Oersted field is proportional to the current flowing in the material, which hinders the miniaturization of the devices since the same current would have to flow through smaller and smaller devices.

The angular momentum carried by a spin-current can be transferred to the magnetization of a ferromagnet, a phenomenon known as spin-transfer torque (STT). Berger and Slonczewski pioneered the excitation and manipulation of the magnetization via a spin current [8, 9, 10]. The torque acting on the magnetic moments arise from the interaction between spin-polarized itinerant electrons and the local moments due to the s-d exchange interaction.

A simple descriptive model to get a broader picture of the STT mechanism is to consider the spin-split bands in a ferromagnet. When a spin-polarized current flows into a ferromagnet and the spin polarization is collinear with the magnetization, electrons with both spins can be transmitted through the ferromagnet via the respective spin channels. On the other hand, if the spin polarization

is noncollinear relatively to the magnetization, then the projection of the spin angular momentum perpendicular to the magnetization has to be absorbed so that the electrons can be transmitted into the conduction bands. The perpendicular momentum is then transferred to the magnetization, acting as a torque. The perpendicular projection of spin current can be expressed as $I_s - (I_s \cdot m)m$, which noting the mathematical identity of the double cross product might be rewritten as $m \times (m \times I_s)$. Therefore, equaling the orthogonal spin current to the spin-transfer torque gives:

$$\tau_{STT} \propto m \times (m \times I_s) \ , \tag{2.12}$$

also called the Slonczewski torque. It takes the same form as the damping parameter when expressed in the LL equation. Thus, depending on the current polarity, it adds up or substracts to the damping term, enhancing or reducing the relaxation of the magnetization. More interestingly though is when these two terms have opposite signs and the STT overcomes the damping. In such conditions magnetic reversal is possible as well as exciting steady-state magnetic oscillations, both sought-after phenomena for applications [11, 12, 13, 14]. Specially in magnetic memory applications, the STT opens the possibility to a higher density and low-power memory device, overcoming the disadvantages of field writing. In particular due to being better scalable as the STT is proportional to the current density instead of the total current. It has been shown as a very promising technology being employed already in commercial RAM memories, STT-RAM [15, 16]. Secondly, it brings a new functionality to spintronic devices as current-induced nano oscillators. Auto-oscillations may be induced where the magnetization precesses around the effective field H_{eff} and the damping is counter-balanced by the STT. The frequency of these auto-oscillations is usually around the GHz range [17, 18, 19].

While studying the STT in spin-valve devices, an extra torque was observed. Unlike the STT which is even the magnetization, the observed extra term was odd in magnetization, being proportional to $m \times I_s$. It has the same symmetry as the precessional term in the LLG equation, hence it is known as the field-like torque. While the STT term can be understood from the conservation of angular momentum, the origin of the field-like term is not so clear with multiple mechanisms already proposed for its origin.

The LLG equation can now be expanded to include these two current-induced torques present in spin-valve like devices. Hence, the equation now reads:

$$\frac{\mathrm{d}M}{\mathrm{d}t} = \gamma\mu_0 M \times H_{eff} - \alpha m \times \frac{\mathrm{d}M}{\mathrm{d}t} + \tau_{STT} m \times (m \times I_s) + \tau_{FL} (m \times I_s) \ , \tag{2.13}$$

where τ_{STT} and τ_{FL} are the amplitude of the STT and field-like torques, respectively. We note that the field-like term adds up to the precessional term and so it can change the frequency of the precessional motion. Secondly, the threshold for current-induced excitation is only determined by the balance between the damping term and the Slonczewski torque.

In order to exploit the spin-transfer effect, we need to first generate a spin current. A couple of possibilities to achieve it is via optical pumping, ferromagnetic resonance, or current polarization by a ferromagnetic layer [20, 21]. Fig. 2.1 illustrates this process for a positive and negative current across the structure. In Fig. 2.1 (a), the fixed layer FM1 injects a spin-polarized current into

the non-magnetic layer along the its magnetization direction. If the current and thus the torque is strong enough to overcome the damping, the free layer FM2 will be oriented parallel to FM1. When the current direction is reversed, the electrons are injected from FM2 into FM1 (Fig. 2.1 (b)). However, in a ballistic model, only the electrons with spins parallel to FM1 are transmitted. The electrons with antiparallel spin are reflected back into FM2 and interact with its magnetization, resulting in a rotation of FM2 to be antiparallel to FM1. Thus, with a single reference layer two states can be written in the free layer FM2, depending on the current polarity. The reference layer is thicker than the free layer, or it is "pinned" via an exchange coupling to another magnetic layer. So that, its threshold to current-induced effect is much higher than in the free layer.

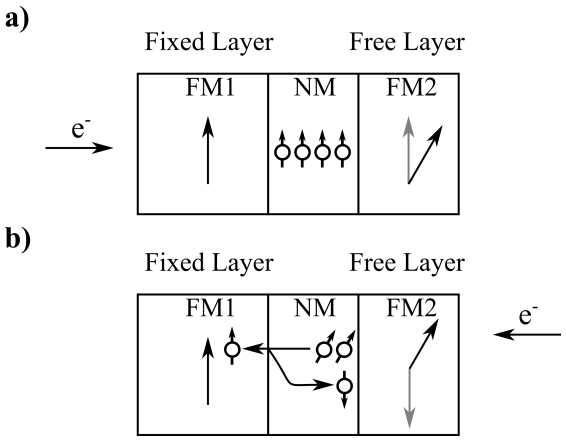

Figure 2.1: Schematic illustration of the spin-transfer torque. **a)** The reference layer FM1 acts as a spin-polarizer, injecting a spin current into the free layer FM2. Due to the STT, the FM2 layer (dark arrow) will be aligned along the FM1 (grey arrow). **b)** Same as in **a)**, but for opposite current polarity. Here, a current flows from FM2 into FM1. The electrons with spin along FM1 are transmitted while the electrons with opposite spin are reflected. The reflected electrons are injected into FM2, promoting a reorientation antiparallel to FM1.

2.4 Spin-Orbit Torque

Another option to generate a spin current is via the spin-orbit interaction (SOI) [22, 23, 24]. Spin-orbit interaction is implicitly included in the relativistic Dirac equation, when expanding it to terms on the order of $1/c^2$ and it is proportional to:

$$E_{SO} \propto \sigma \cdot (\nabla V \times p) \ . \tag{2.14}$$

The SOI can be regarded as the coupling of the spin angular momentum with the effective magnetic field in the lab frame of reference due to the motion of the electron in an electric field. In the lab frame of reference, the magnetic field is given by $(1/c^2)\, E \times v$, and equation 2.14 may be seen as a Zeeman term between the spin along σ and the momentum dependent effective field. In an atom, where the Coulomb field from the nucleus has a radial distribution, the SOI can be expressed as a dot product of spin and angular momenta, $(s \cdot l)$, and thereby the

name of the effect. Additionally, in solids where the Coulomb potential is periodic, the effective field will then be dependent on the k vector of the electrons.

There are a couple of possible origins for an internal electric field besides the Coulomb created by the nuclei. One way is the inclusion of impurities into the system, and secondly by crystal fields appearing at the interfaces or in the crystal structures which breaks the inversion symmetry of the system. The inversion symmetry may be broken by a noncentrosymmetric crystal lattice as in the zincblende structure, which originates the so called Dresselhaus SOI [25]. The SOI due to interfacial symmetry breaking is known as Rashba effect [26, 27].

The interfacial symmetry breaking is convenient as it allows the usage of magnetic materials without any structural asymmetry. Therefore, a common approach is to grow a nonmagnetic material with high SOC in contact with a thin FM layer. The electrical switching of the magnetization has been observed in such multilayer systems [28, 29]. However, two mechanisms can play a role at inducing the spin-orbit torque.

One mechanism is the injection of a spin current into the FM layer due to the spin Hall effect (SHE) in the heavy metal layer. The SHE generates a pure spin current perpendicular to the electrical current direction, with a polarization orthogonal to both currents. The SHE will be further described later in section 3.1.3. The spin current enters the FM and applies a torque on the magnetization. A similar picture to the STT, where the spin current is an electrical current-induced effect and does not require a second FM layer as a polarizer. Fig. 2.2 (a) illustrates this mechanism. An electrical current in the non magnetic layer generates a spin current resulting in a spin accumulation at the interface. As the current flows along the x-axis and the spin current along the z-axis, the spin accumulation is oriented along the y-axis.

The second mechanism is the inverse spin-galvanic effect (iSGE), where an electrical current induces a spin accumulation at the interface [30, 31]. Assuming the symmetry is broken in the z-axis by an interface, the Rashba spin-orbit coupling takes the following form:

$$E_R \propto (z \times k) \cdot \sigma \ , \tag{2.15}$$

where k is the electron's momentum vector and σ its spin. As a consequence the energy bands are spin split in momentum space (Fig. 2.2 (d)). Such spin textures lock the electron's spin to its momentum. Because of it, if an electrical current flows in these spin-polarized states, the electrons will acquire the respective spin direction. In Fig. 2.2 (b) a spin accumulation appears at the interface due to the structure inversion asymmetry and the Rashba spin-orbit interaction. The Rashba spin-orbit interaction leads to a spin texture where the electron's spin is perpendicular to its momentum, as depicted in Fig. 2.2 (c).

Once the spin accumulation is generated at the interface, it can act on the magnetization. The spin accumulation gives rise to two effectives fields. One which is parallel to the spin along $H_{FL} \parallel y$ and a second one along the cross product $H_{AD} \parallel m \times y$. When considering the torques originating from these current-induced effective fields, the first has the same symmetry as the field-like torque in equation 2.13, and the second as the Slonczewski torque. Thus, the LLG equation written for the STT is also useful to describe the SOT. However, more generally the Slonczewski term is referred to as damping-like or antidamping

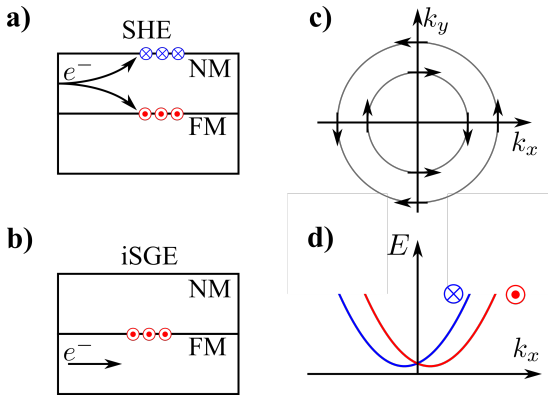

Figure 2.2: Schematic illustration of the spin-orbit torque. **a)** SOT via SHE and **b)** SOT via iSGE. **c)** Rashba spin texture at the Fermi level. The arrows show the direction of the Rashba effective field, which locks the electron's spin perpendicular to its momentum. **d)** Dispersion relation and spin splitting induced by the Rashba spin-orbit interaction.

torque. Here, in this work the we will be using the later.

The LLG equation is then rewritten as:

$$\frac{\mathrm{d}M}{\mathrm{d}t} = \gamma\mu_0 M \times H_{eff} - \alpha m \times \frac{\mathrm{d}M}{\mathrm{d}t} + \tau_{AD} m \times (m \times \sigma) + \tau_{FL} (m \times \sigma) \ , \quad (2.16)$$

where τ_{AD} and τ_{FL} are the magnitude of the current-induced torques, and σ the direction of the spin accumulation. Noteworthy is that while H_{FL} is independent of the magnetization, H_{AD} depends on the magnetization direction.

3. Magnetotransport

3.1 Magnetoresistances

Magnetoresistance is the phenomenon in which the electrical resistance of a material changes in the presence of a magnetic field or depends on the magnetic order. It comprises a large family of effects which can be observed in systems ranging from bulk non-magnetic materials, magnetically ordered materials and multilayered systems. Magnetoresistance effects has been widely studied due to its potential applications in a variety of fields, including the development of magnetic sensors and magnetic memory devices. This chapter focus on summarizing the main effects present when evaluating the resistance dependence on magnetic fields.

3.1.1 Anisotropic Magnetoresistance

Anisotropic magnetoresistance (AMR) was discovered in the 19^{th} century by Lord Kelvin. It was described as the relative change in resistance when the magnetization lies along and perpendicular to the electrical current. The AMR arises from the spin-orbit coupling and it is a bulk effect being observed in single-layered systems. This effect can split into two contributions, a crystalline and non-crystalline AMR [32]. The first one reflects the crystal symmetries and hence it is a function of the angle between the magnetization and the crystal lattice. Mainly observed in single crystal samples, as in polycrystalline systems this contribution averages out. The second and most common contribution, the non-crystalline, describes the effect observed by Lord Kelvin that is the variation of resistance dependent on the angle between magnetization and current. It is expressed as:

$$AMR = \frac{R_{\parallel} - R_{\perp}}{R_{av}} \tag{3.1}$$

with $R_{\parallel}$ and $R_{\perp}$ the resistances while the magnetization is parallel and perpendicular to the current, and R_{av} their average value [33, 34]. The AMR manifests itself not only as a longitudinal resistance but also as a transverse resistance similar to Hall effects. Thus, this transverse phenomenon is traditionally known as planar Hall effect. However, in this thesis it will be called transverse AMR as it follows different symmetries from the Hall effects.

The non-crystalline AMR is usually studied in Hall bar devices by performing field rotations. Both longitudinal and transverse resistances exhibit the following angular dependences:

$$R_{xx} \propto \cos 2\phi \tag{3.2}$$

$$R_{xy} \propto \sin 2\phi \tag{3.3}$$

where ϕ is the angle between magnetization and electrical current.

The AMR is even in magnetization, and consequently it is not the magnetization's direction but its axis that plays a role. In a collinear antiferromagnet, both magnetic sub-lattices lie along the some axis and therefore it would be expected that this effect is not cancelled out even in a zero net moment system. And

indeed, AMR has been observed in collinear antiferromagnets [35, 36, 37]. The previous expressions for the angular dependence still hold for the antiferromagnets, when the defining the angle ϕ as the angle between the order parameter, the Néel vector, and the current.

Equations 3.3 express the simplest form the non-crystalline AMR can take, and higher-order terms might be present. Concerning the crystalline AMR, it takes after the lattice symmetry. For instance in [37], using a corbino geometry a strong six-fold component is observed due to the hexagonal crystalline structure of the MnTe.

3.1.2 Giant and Tunneling Magnetoresistances

After the almost simultaneous observation by groups of Albert Fert and Peter Grunberg in the late 80's, the 2007's Nobel Prize was awarded to both for the discovery of the giant magnetoresistance (GMR) [38, 39]. The GMR is a phenomenon observed in multilayer systems comprising ferromagnetic layers separated by a non-magnetic conductive layer. The 'giant' name came due to the large 50% magnetoresistance observed at the time.

The GMR describes the change in resistance due to the relative orientation of two ferromagnetic layers. It originates from the spin-dependent scattering at the ferromagnetic interfaces, and it is present in the two possible geometries, current in plane (CIP) and current perpendicular to plane (CPP). The second case is more intuitive to visualize. In it, the current first flows through one FM becoming spin-polarized. The spacer layer is usually a non-magnetic conductive material with small spin-orbit coupling (longer spin-diffusion length), in order for the polarized current to flow with minimum scattering and to not dissipate its spin-angular momentum. Lastly, at the interface from the non-magnetic into the second FM, the spin-polarized electrons have a larger scattering rate if their spin is not parallel with the FM's magnetization. Thus, for antiparallel ferromagnetic layers a large resistance is measured, while for parallel a minimum resistance value.

In a CIP geometry, the conduction electrons need to scatter and diffuse through the three-layered stack to "feel" the parallel or antiparallel magnetic configuration. It was initially modeled based on the Boltzmann transport equation, where mainly the interfacial spin-dependent scattering is taken into account [40].

Similar to GMR, tunneling magnetoresistance (TMR) is observed when the non-magnetic conductive spacer layer is replaced by a thin insulating layer, which the current tunnels through in a CPP geometry. The quantum tunneling is determined by the density of states of both FM layers, and so it depends on their relative orientation similar to GMR. Regarding the observed magnitude of these magnetoresistances, in a GMR-based device a relative change of 70% was observed and a 600% change in a TMR device [41, 42].

Both of these effects can show a large relative change in resistance, which is highly sought after for applications. The most common device taking advantage of these phenomena is a spin-valve, and it is used as a field sensor or for reading the state of a magnetic memory cell. It consists of two FM layers, usually called reference and free layers, and they differ on their robustness. Such is achieved via

different coercivity fields, either by choosing different FM materials or exchange pinning the reference layer.

3.1.3 Hall family

In 1879, Edwin Hall made the discovery that an electrical current is deflected when in the presence of a magnetic field [43]. The electrons are subjected to the Lorentz force, i.e., they feel a force perpendicular to the current and magnetic field directions. This results in an accumulation of charges on one side of the conductor, leading to a voltage developed orthogonally to the current - the transverse voltage. The described effect is the well known Hall effect (or ordinary Hall effect - OHE), present in any conducting material.

Soon after, Hall realized that the same phenomenon in ferromagnetic materials yielded a much larger response. The stronger Hall effect response in ferromagnets became known as the anomalous Hall effect (AHE) [44, 45]. Empirically, the total Hall resistivity is expressed as

$$\rho_{xy} = R_0 H_z + R_s M_z \ . \tag{3.4}$$

The first term is the OHE contribution proportional to the out-of-plane magnetic field, where the R_0 is the ordinary Hall coefficient mainly dependent on the carrier concentration. The second term attempts to describe the AHE contribution into the transverse resistivity. It expects the AHE signal to scale with the out-of-plane component of the magnetization. Even though the previous expression applies to a wide range of materials, it fails to describe the presence and strength of the AHE in magnetically ordered materials with a vanishing net magnetization.

Indeed, the assumption that the AHE is proportional to the magnetization was firstly challenged on certain non-collinear antiferromagnets [46, 47, 48]. And more recently, a theoretical study predicts the presence of a spontaneous Hall effect on the collinear ordered antiferromagnetic RuO_2 [49, 50].

Karplus and Luttinger, in 1954, proposed the connection between AHE and spin-orbit interaction [51]. Starting from the relativistic corrections to the Hamiltonian of an electron inside a periodic lattice potential and perturbed by an applied electrical field, they concluded that an additional term should be added to the usual electron's velocity - the anomalous velocity. Later, the concept of anomalous velocity was discovered to be related with the Berry curvature in the momentum space [52, 53]. The Berry curvature can then be regarded as a fictitious magnetic field in the momentum space. Note that, in contrast to a real-space magnetic field which is divergence free, $\nabla \cdot B = 0$, the divergence of the Berry curvature can be non-zero. It can show very sharp features specially at or near degeneracy bands and band crossings [53, 54]. This opens an interesting way manipulate the Hall response by tuning the Fermi level close to these features in the band structure.

It is relevant to note the constraints imposed by time and inversion symmetries. The momentum dependent Berry curvature $\Omega(k)$ transforms under the time-reversal symmetry as $\mathcal{T}\Omega(k) = -\Omega(-k)$, and under inversion symmetry $\mathcal{P}\Omega(k) = \Omega(-k)$. Therefore, in a system with the combined inversion and time $\mathcal{PT}$ symmetry, it follows that the Berry curvature must be zero [55]. This is

of special importance for systems like the $\mathcal{PT}$ symmetric and antiferromagnetic CuMnAs, where no AHE is expected.

The previously described anomalous Hall effect is the intrinsic contribution. There are two other mechanisms, skew scattering and side jump, which rely on the presence of impurities in the system.

The family of Hall effects goes beyond the OHE and AHE. Here, however, we will only briefly mention two other phenomena, the spin Hall effect (SHE) and topological Hall effect(THE).

An additional contribution to the Hall conductivity has been proposed stemming from a nontrivial spin arrangement - the topological Hall effect. The origin of this effect is the Berry phase picked by the conduction electron when adiabatically moving through a topologically stable spin structure. In contrast to the previously described intrinsic AHE, theoretical works predict this phenomenon even while omitting the spin-orbit interaction [56, 57]. The effect was first reported in MnSi and linked to its magnetic phase where a skyrmion lattice is expected [58]. The THE is not only expected in the presence of skyrmions but it is also theorized to be present in more complex spin structures within the unit cell. THE has been reported and studied in non-collinear antiferromagnets such as Mn_5Si_3 and Mn_3Ge [59, 47]. The THE is induced by the so-called spin chirality. This quantity is defined as $k = \vec{n}_i \cdot (\vec{n}_j \times \vec{n}_k)$, where $\vec{n}$ is the unit vector giving the direction of the moment at the particular site (i,j,k) within one triangular sublattice [56]. A coplanar spin arrangement yields a $k = 0$, hence the topological Hall effect is associated with a noncoplanar spin order.

The spin Hall effect was initially predicted in 1971 by Dyakonov and Perel [60], and only 30 years later it was experimentally observed [61, 62]. It is an analogue to the anomalous Hall effect but observed in nonmagnetic systems without applying magnetic fields, as it also originates from the spin-orbit coupling. It is characterized by a pure spin current transverse to the electrical current, leading to the accumulation of opposite spin angular momenta on opposing edges of the conductor. Due to a majority and minority spin populations, in a ferromagnet with a net spin polarization the AHE leads to a net charge imbalance between opposite sides of the sample. In contrast, the SHE in a nonmagnetic material does not result in an imbalance of charge accumulation as, the equal number of spin up and down electrons are "pushed" against opposite edges of the sample.

This effect is usually described by a material's specific quantity, its spin Hall angle θ_H. The spin Hall angle is defined as the ratio between the spin momentum and electrical charge currents. Similarly to AHE, the SHE exhibits two contributions, extrinsic and intrinsic. The extrinsic SHE results from spin dependent scattering at impurities, whereas the microscopic origin of the intrinsic is the momentum dependent spin orbit field [63, 64]. Because the spin orbit coupling is influenced by the nuclei, it is expected that heavy elements exhibit a larger SHE, as it is the case for Pt.

From an application point-of-view, this effect is quite versatile. On one hand it can be used as a source of spin current, and thereby excite adjacent magnetic layers. Or taking advantage of the inverse SHE (iSHE) a pure spin current can be detected when converted into an electrical current in a heavy metal layer [65, 66, 67].

3.2 Thermoelectric Effects

Whereas the phenomena described above are driven by an electric field, or a gradient in electrical potential, similar phenomena is also observed when the electrons are driven by a temperature gradient. The thermal-induced effects exhibit a symmetry which closely resembles the same as the electrical driven ones. Hence, they are often described as their thermal counterpart. A heat current couples not only to the charge current, but also to the spin current. The interplay between these quantities is the scope of study of spin caloritronics. Spin caloritronics is then concerned with effects such as, the spin dependence on the Seebeck and Peltier effects, and the counterpart to the Hall family - the Nernst effects [68].

Despite often regarded as possible sources of artefacts on magneto transport measurements, thermal effects can also be exploited in order to study and detect magnetic order. Thus, here we are going through a brief overview of some thermoelectric effects.

Firstly, we start with the Seebeck effect, or thermopower. It describes the voltage build up when a temperature gradient is generated in the material. The Seebeck coefficient of a material is thus defined as the ratio between voltage and thermal gradient:

$$S = -\frac{\Delta V}{\Delta T} \ . \tag{3.5}$$

The thermal generated charged current can interact with an external field and with the magnetic order present in the system, giving rise to the Nernst effects. In a similar fashion, we have ordinary and anomalous Nernst effects (ONE and ANE), respectively stemming from the interaction with an external magnetic field and with the magnetic order. They correspond to the thermal counterparts of OHE and AHE. Analogous to the AHE, ANE is observed in ferromagnetic materials as well as in antiferromagnets where the fictitious magnetic field, Berry curvature, plays the main role [69, 70, 71, 54]. To our knowledge, no observation of the thermal counterpart of the altermagnetic Hall effect has been reported.

A thermoelectric equivalent to the AMR is also observed in magnetic materials, where the thermally driven charge current is affected by the orientation of the magnetic order with respect to the current direction. It shows the same symmetry as the conventional AMR, being measurable in both longitudinal and transverse configurations.

Magneto thermoelectric effects are also observed in non-magnetic materials, such as the spin Nernst effect (SNE) [72, 73]. Spin Nernst effect is the generation of a transverse spin current flowing perpendicular to the thermal gradient, ie, the thermal equivalent of the SHE.

The last effect we mention here is the spin Seebeck effect (SSE). It is observed in ferromagnetic and nonmagnetic multilayers, and it refers to an induced electrical current by a thermal gradient across the ferromagnet-nonmagnetic interface [74, 75, 76, 77]. The spin Seebeck effect can be split into two phenomena. First, the generation of a spin current in the ferromagnet and secondly, the conversion of spin into charge current in the nonmagnetic layer via iSHE. The spin carried by conduction electrons alone cannot explain this effect, as it has been observed in ferromagnetic insulators such as YIG. Instead, it is attributed to be mediated

by magnons.

The Fig. 3.1 illustrates the Hall and Nernst effects mentioned above, as well as it highlights the how these can be regarded as electrical-thermal counterparts. The thermoelectric Seebeck and spin Seebeck effects are schematically shown in Fig. 3.2 . Fig. 3.2 illustrates the longitudinal configuration of the SSE. Here, both the spin current and the temperature gradient are parallel. It is also possible to observe the SSE in a transverse geometry, where the spin current flows perpendicular to the temperature gradient. In case of a conductive ferromagnet, the transverse geometry allows a thermal voltage measurement clean of other thermoelectric effect like ANE.

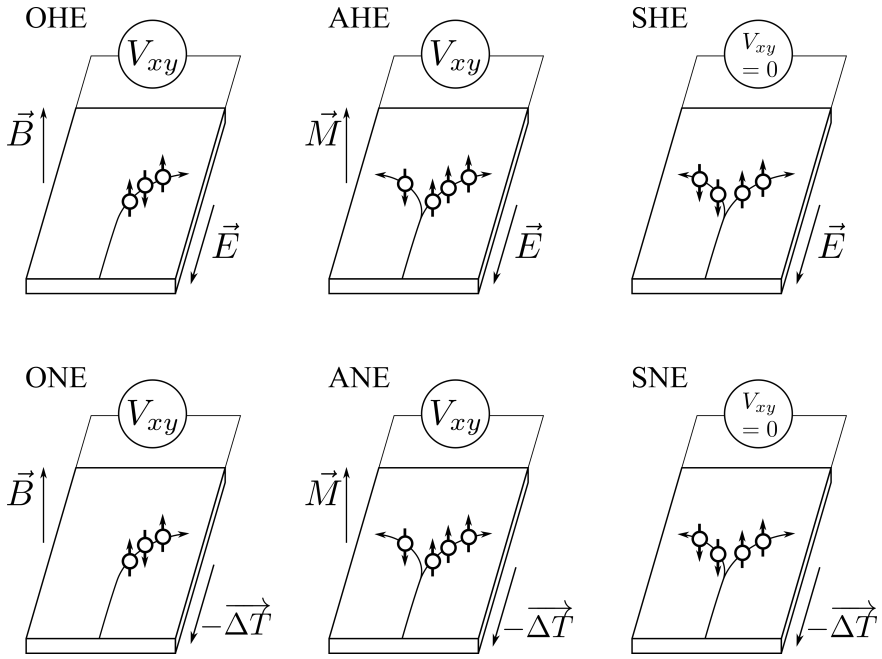

Figure 3.1: Schematics of the Hall and Nernst effects.

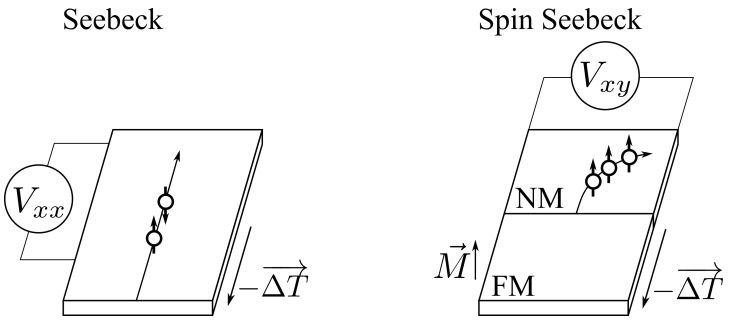

Figure 3.2: Schematics of the Seebeck effect and spin Seebeck effect. SSE depicted here is the longitudinal configuration, where the spin current and thermal gradient are collinear. There is also a transverse geometry not shown here.

4. Antiferromagnetic Systems

In this chapter, we will focus on the different antiferromagnetic systems utilized throughout this work. As mentioned in the first chapter, the main focus of this work lies on AFM systems that preserve the combined inversion and time symmetry $\mathcal{PT}$, with special attention on how to detect its magnetic order.

In order to electrically detect the reversal of the order parameter, we need an odd effect in magnetization. When looking at the linear-response magnetoresistance described by $E_i = \rho_{ij} j_j$, it means that $\rho_{ij}^{\text{odd}}(\mathcal{O}) = -\rho_{ij}^{\text{odd}}(-\mathcal{O})$. E is the electric field, j the electrical current, $\mathcal{O}$ the magnetic order parameter and ρ_{ij}^{odd} the resistivity tensor which is odd under time reversal. This way, when the order parameter is reversed the measured signal E_i changes sign. ρ_{ij}^{odd} can include the AHE contribution for instance, and additional effects equally odd in magnetization.

Applying the $\mathcal{PT}$ operation to the resistivity tensor yields, $\mathcal{PT}\rho_{ij}^{\text{odd}}(\mathcal{O}) = -\rho_{ij}^{\text{odd}}(\mathcal{O})$. The Neumann's principle links the symmetries of the crystal to its physical properties. Therefore, it imposes that in a $\mathcal{PT}$ symmetric system $\rho_{ij}^{\text{odd}} = \mathcal{PT}\rho_{ij}^{\text{odd}}$, or $\rho_{ij}^{\text{odd}} = -\rho_{ij}^{\text{odd}}$. By symmetry, we have then that $\rho_{ij}^{\text{odd}} = 0$.

In section 3.1.3, we showed that the Berry curvature, behind the AHE, vanishes under $\mathcal{PT}$ symmetry. Here, by symmetry arguments we see how the same symmetry does not allow any linear-response stemming from an odd magnetoresistance. On the other hand, even effects are still allowed, such as the AMR. Note that while $\mathcal{T}\rho_{ij}^{\text{odd}} = -\rho_{ij}^{\text{odd}}$, for the even tensor we have $\mathcal{T}\rho_{ij}^{\text{even}} = \rho_{ij}^{\text{even}}$.

We will introduce two AFM systems with $\mathcal{PT}$ symmetry. First, we start with the most simple AFM system where two ferromagnetic layers are antiferromagnetically coupled, that is, a synthetic antiferromagnet. Then an example of a natural AFM with $\mathcal{PT}$ symmetry, the CuMnAs. Since these systems are restricted to $\rho_{ij}^{\text{odd}} = 0$, the electrical detection of the magnetic order has relied on even effects, mainly the AMR. Regarding the synthetic antiferromagnets, a second option is an intentional non compensation between the FM layers, resulting in a net magnetic moment and a broken $\mathcal{PT}$ symmetry.

Lastly, we introduce Mn_3Sn, a noncollinear AFM and which allows the presence of AHE.

4.1 Synthetic Antiferromagnets

With properties in-between ferromagnets and antiferromagnets, synthetic antiferromagnets (SAFs) have recently drawn some attention as they show some of the benefits of AFMs while being easier to control, thus being regarded as a model system to AFMs. Synthetic antiferromagnets comprise multilayer systems where ferromagnets are antiferromagnetically RKKY-coupled, from the simplest trilayer structure to superlattices (Fig. 4.1). There are two main differences between synthetic and bulk antiferromagnets: the strength of the exchange interaction and the tunability of the SAFs. The former makes it much easier to manipulate the magnetic ordering in SAFs, in contrast to AFMs that show exchange fields of several Tesla. The latter, the tunability, comes from the high degree of freedom when choosing the layers' composition and thickness. Moreover, the traditional

tools to study the ferromagnetic order, as the AHE or the magneto-optical Kerr effect, may be used when choosing slightly different ferromagnetic layers in the SAF system [78].

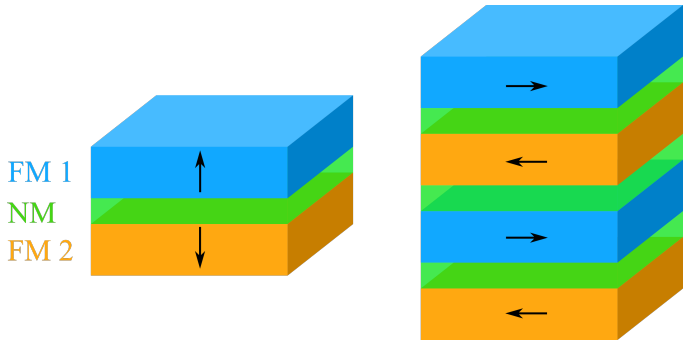

Figure 4.1: Synthetic antiferromagnetic systems. **a)** Trilayer system comprising two out-of-plane ferromagnetic layers (FM1 and FM2), and a nonmagnetic metal (NM) in between them. **b)** Multilayer system of multiple in-plane magnetized ferromagnetic layers. The arrows correspond to the respective layer's magnetization.

In order to manipulate the magnetic order in SAFs, the spin-Hall effect is commonly used by growing a heavy metal layer adjacent to the ferromagnet. Electrical switching between two in-plane orthogonal directions has been observed [79]. Different mechanisms and geometries of SOT switching in SAFs have also been reported [80, 81, 82, 83]. Also similar to AFMs, fast domain-wall motion and absence of Walker breakdown has been observed and predicted [84, 85]. Other interesting properties of SAFs include systems where the interlayer exchange can be electrically controlled [86], and it has been suggested that the Magnus force acting on skyrmions would be canceled out [87].

We consider a SAF with perpendicular magnetic anisotropy, with the following structure: Si/SiO2(sub.)/Ta(1.5)/Pt(5)/FM2/ Ir(0.6)/FM1/ Pt(4)/Ru(3), the number in parenthesis corresponds to the layer thickness in nm. Nominally, both ferromagnetic layers FM1 and FM2 are identical and they are composed by the following multilayers: [Co(0.2)/Ni(0.7)]x3 /Co(0.2). It comprises two ferromagnetic layers coupled via RKKY through an Ir layer, which are in-between two Pt layers, Fig. 4.2 .

The Pt layers play a key role in this heterostructure, they allow for the control of the adjacent FM layer. Two effects can take place simultaneously. A spin current can be injected into the FM layer due to the SHE in the Pt. And as the interface is swapped between the two pairs of Pt/FM, it results in an opposite polarized spin current flowing into the ferromagnets. This is illustrated in Fig. 4.2 by the spin polarized electron at the interfaces with polarizations σ_1 and σ_2. The second phenomenon is the Rashba-Edelstein effect, that is, the spin-momentum locked at the interfaces due to the local broken inversion symmetry. Similarly, as for the SHE case, this effect is also opposite at both the interfaces.

With the spin injection from SHE and/or spin accumulation from the Rashba-Edelstein effect, our system exhibits a staggered spin polarization acting on the antiferromagnetically coupled moments. Reminiscent of the cAFM CuMnAs and Mn_2Au, as discussed next. Hence, such a multilayer sample might be seen as a

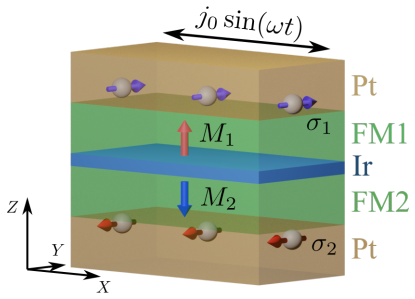

Figure 4.2: Studied out-of-plane SAF system, which is in-between two Pt layers. Due to the SHE in both Pt layers, we have a staggered spin polarization acting on each magnetic moment. Reminiscent of the Néel spin-orbit torque present in CuMnAs.

model system of the cAFM where the Néel spin-orbit torque is present. With the advantages that it is easier to externally manipulate (weaker exchange interaction) and we are not restricted by the system's symmetries required to observe the Néel spin-orbit torque.

Note that an important difference between the SAF system and the CuMnAs films is their anisotropies. While the SAF has an out-of-plane easy axis, the moments in the CuMnAs lie on the basal plane following and uniaxial or biaxial anisotropy. How this affects the electrical manipulation and detection of the magnetic order will be shown and discussed later on chapter 5.

4.2 CuMnAs - Collinear Antiferromagnet

In a ferromagnet, the positive intralayer exchange favors the alignment of neighboring spins. It leads to a long-range magnetic order, where within a single magnetic domain all spins lie along the same direction. Hence, they can show a spontaneous magnetization at zero field.

A negative exchange interaction, on the other hand, leads to the antiparallel arrangement of neighboring spins. A simple antiferromagnetic system we can picture is a 1D chain of alternating spins ($\uparrow\downarrow\uparrow\downarrow\ldots$). Expanding the idea to the 3D case and we have the collinear AFM (cAFM). They are then characterized by two antiparallel magnetic sublattices, which compensate each other, resulting in a zero net moment within the unit cell. Instead of the vanishing net magnetization, the order parameter in cAFM is the Néel vector $\vec{L}$. It is defined as $\vec{L} = \vec{M}_A - \vec{M}_B$, with $\vec{M}_A$ and $\vec{M}_B$ the magnetization of each sublattice.

Part of this work focused on the epitaxially grown CuMnAs, which drawn special attention after the demonstration of electrical manipulation of the Néel order [2]. When grown by molecular beam epitaxy, thin film layers of CuMnAs can be stabilized in a tetragonal phase (Fig. 4.3) and show a Néel temperature of 480 K [88].

The first technological application of AFM was in spin-valve type of devices. The AFM was pinning layer for the reference FM layer via the exchange bias effect. In order for the AFM to become from a passive element in multilayer systems as a pinning layer into an active element in a spintronic device, a main

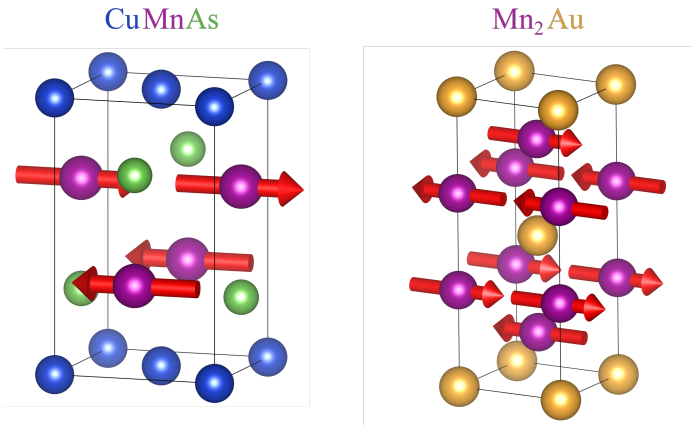

Figure 4.3: Crystal structure of collinear antiferromagnetic CuMnAs and Mn_2Au.

challenge would have to be overcome - How to control the antiferromagnetic order? Due to its compensated moments, it becomes quite insensitive to external fields. However, an AFM still responds when subjected to strong magnetic fields. When the magnetic field is applied along the hard axis of the cAFM, the two moments cant towards the field direction until they are aligned to the field and parallel to each other, i.e., the so called spin-flip field. The second case is if the field is along the easy axis. Here, the system is unresponsive until the spin-flop field, the field at which both moments rotate to be perpendicular to the easy axis. To be more exact, if, as shown in Fig. 4.4 (d), the Zeeman energy due to the magnetic field-induced tilting of the magnetic moments becomes larger than the anisotropy energy, the AFM-coupled moments "flop" from the easy axis to the hard axis. This dependence on an external field is schematically shown in Fig. 4.4 . For the case of CuMnAs, the spin-flop field is observed to be close to 2 T [89].

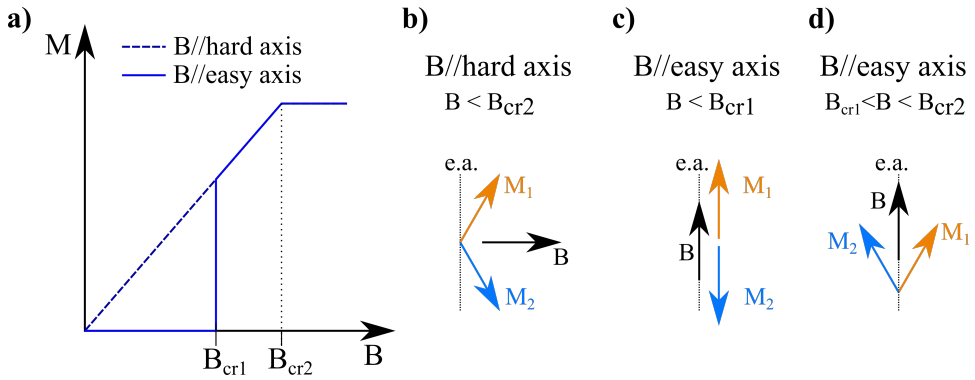

Figure 4.4: Collinear antiferromagnet under external field. **a)** Net magnetization as a function of the applied field. Two critical fields can be observed. B_{cr1} and B_{cr2} are the spin-flop and spin-flip fields, respectively. **b)** If the applied field is along the hard axis, then the moments cant towards it. **c)**When aligned with the easy axis, before the spin-flop the moments remain unchanged. **d)** And after it follows a similar behavior to a hard axis field sweep.

Despite an external field can influence the magnetic order of a cAFM, it is not a reliable and useful way to control it. Firstly, as the critical fields, spin-flop and

spin-flip fields, can be as strong as several Tesla. Since both of them depend on the strength of the large exchange field. But more importantly, because the external field cannot differentiate between reversed Néel vector states. Nor deterministic switching between reversed AFM states can be triggered by an externally applied magnetic field. That is, in Fig. 4.4 one can swap both magnetizations, M_1 and M_2, as both configurations are energetically equal. Even though the Néel vector L has reversed.

In 2014, Železný et al. predicted the existence of a current-induced effective spin-orbit field that acts in opposite directions for each sublattice, i.e., a staggered effective field on the atomistic scale following the antiferromagnetic order of the AFM. A field whose sign alternates between magnetic sublattice allows for a deterministic way to control the direction of the Néel vector. In order to be present the material should exhibit certain symmetries conditions, local broken inversion symmetry at the magnetic sites and the magnetic sublattices should form inversion partners [1, 90]. It was initially predicted in Mn_2Au [1], and experimentally demonstrated first in CuMnAs [2] and later in Mn_2Au [91, 3]. Both systems meet the symmetry requirements and their respective crystal structure is shown in Fig. 4.3 .

In a simple model, the current-induced effective field follows the same symmetry as Rashba spin-orbit field. Its staggered nature means that the sign of the spin-orbit interaction changes, since the crystal field at the magnetic atoms of the two magnetic sublattices is reversed. Similar to the SOT in FM systems, the current induced effective spin-orbit fields exert a torque on the magnetization. From the two possible spin-orbit torques, deterministic switching of CuMnAs is only due to a field-like type of torque. The current-induced antidamping torque remains inefficient for acting on the AFM order because, similar to an externally applied field, the corresponding spin-orbit field is not of staggered order. In Fig. 4.5 (a) the Rashba spin texture is shown in equilibrium and, in (b) when at nonequilibrium. While at nonequilibrium, the redistribution of charges leads to a net spin polarization perpendicular to the current direction. Here, it is only the spin texture for one magnetic sublattice, as the second one has the opposite sign. From the field-like torque and the staggered Rashba texture, we can set the Néel vector orthogonal to the electrical current (Fig. 4.5 (c) and (d)).

The detection of changing the magnetic order by 90° was achieved via AMR reading. The AMR is even in magnetic order, thus it cannot detect a Néel vector rotation by 180°. However, it yields maximum signal when comparing perpendicular Néel vectors. Depending on the geometry between writing pulses and probing current in Hall cross structures, the AMR signal is observed in either longitudinal or transverse resistance (see equations 3.3). In Fig. 4.5 (e) is illustrated a geometry where the AMR is seen in R_{xy}, i.e., the writing pulses are both at ±45°. The measured change in resistances are shown in (f).

The direct observation of the magnetic reorientation via optical means allowed to confirm the previous interpretation based on the indirect electrical measurements (Fig. 4.5 (g)). The magnetic domains were mapped using X-ray photoemission electron microscopy (XPEEM) where the magnetic contrast is obtained due to X-ray magnetic linear dichroism (XMLD) [93, 92]. Similar to AMR, XMLD is even in magnetization, hence it can would give us information regarding the axis of the Néel vector and not its direction. It yields maximum contrast when

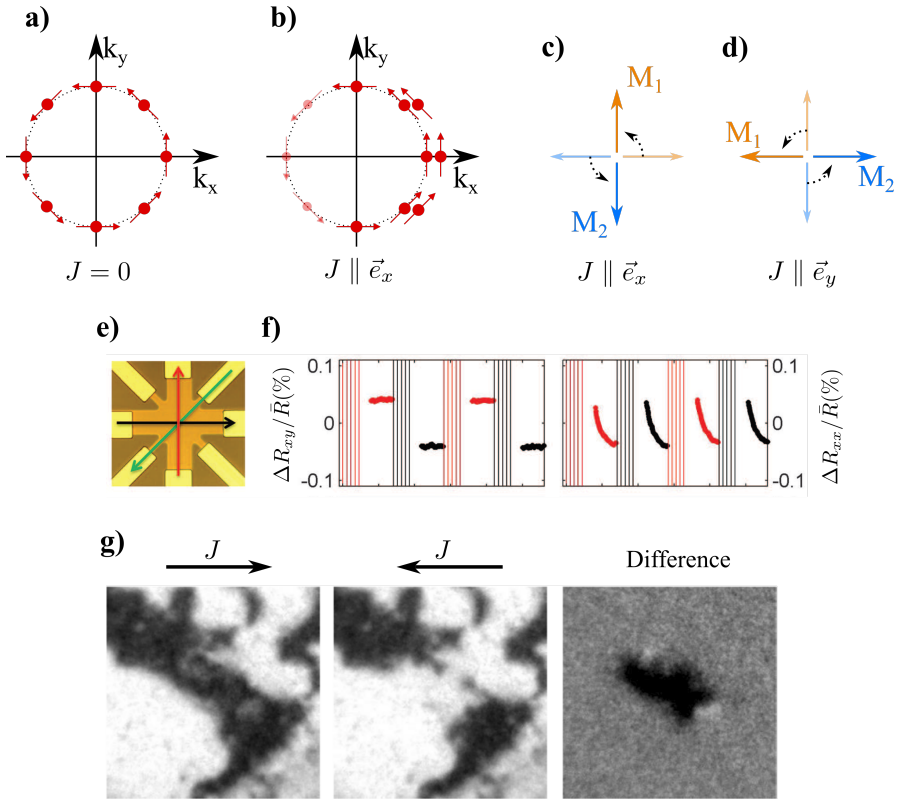

Figure 4.5: Staggered effective field and electrical switching in CuMnAs. **a)** and **b)** Schematic of Rashba spin texture (red arrows) for one magnetic sublattice in equilibrium and nonequilibrium, respectively. **c)** and **d)** The Néel spin-orbit torque allows the manipulation of the magnetic order electrically, setting the Néel vector perpendicular to the current direction. **e)** Measurement geometry, with the red and black arrows corresponding to the electrical pulses directions and the green arrow to the probing current. **f)** Change in transverse R_{xy} and longitudinal R_{xx} resistances, after a sequence of red and black writing pulses. $\bar{R}$ stands for the average longitudinal resistance. **g)** Detection of current polarity-dependent switching using XMLD-PEEM (view of $4\mu m \times 4\mu m$). The white and dark regions correspond to magnetic domains aligned orthogonally. Adapted from [2, 92].

the moments lie along and perpendicular to the X-ray polarization.

Without the long-range interaction, the magnetic order in cAFM becomes more susceptible to the local environment, such as crystal defects. Reimers et al. recently shown the correlation between the location of domain walls and structural twin defects [94]. The nonuniformity of the magnetic environment results in a complex electrical switching behavior. Upon crossing the switching onset, one single pulse does not reorient the whole sample. Instead, only a certain volume is affected. The switched volume is observed to be a function of the pulse height as well as of the number of equal pulses. This adds extra functionality as a multi-level memory cell to the CuMnAs devices [95].

An important advantage of AFM-based devices over conventional ferromagnets is their expected speed of operation. The strong exchange interaction in AFM leads to a higher precessional frequency (eq. 2.11), expected to be in the THz range. So far the switching of CuMnAs has been observed when driven by

short pulse lengths in the sub-nanosecond range and by picosecond THz radiation [96, 97].

Although the switching was initiated by picosecond excitations (pulses or sequences of pulses), it is not known whether the switching time is also of similar ultrafast speed, e.g. due to coherent precessional rotation or fast domain wall motion, or whether it requires a much longer time, e.g. when driven by thermally assisted reversal processes.

When electrical switching was mentioned above, it was synonymous with current-direction dependent reorientation of the magnetic order due to spin-orbit torque switching. However, a second type of switching was observed in CuMnAs - quench switching [98]. Here, the magnetic texture is drastically changed when a strong excitation is applied using electrical or optical pulses of sufficiently large magnitude to heat the magnetic system close to or above Neel's temperature. This causes the magnetic domains to fracture, a process known as 'domain shattering' due to "quench switching" (Fig. 4.6). The quench switching is usually accompanied by a large resistance variation (larger than expected from AMR) and subsequently a relaxation of the signal over time. The high density of domain walls could be responsible for the significant increase in electron scattering, in this shattered state where the domain size becomes comparable to the domain wall width. Moreover, the recent observation of atomically sharp domain walls in CuMnAs could additionally provide another source of electron scattering. This could explain the large resistance change in quench switching. These ultra-narrow features were observed using differential phase-contrast scanning transmission electron microscopy (DPC-STEM)[99].

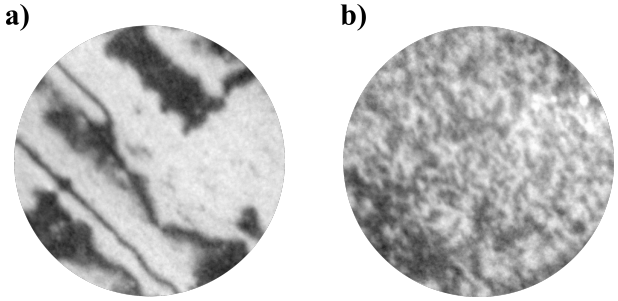

Figure 4.6: XMLD-PEEM images of domain fragmentation in CuMnAs (view of $8\mu m$). **a)** and **b)** Before and after the application of a strong electrical pulse, respectively. Adapted from [98]

4.3 Mn_3Sn - Noncollinear Antiferromagnet

Besides the collinear magnetic phase, AFM can also exhibit a noncollinear phase (ncAFM). Instead of the antiparallel configuration, more complex magnetic orders appear, in order to minimize the net magnetization. One example is the triangular antiferromagnetic order present in the Mn_3X family with X = (Sn, Ge, Ga).

The frustration in the magnetic system to accommodate the multiple spins and the interplay of different interactions, such as anisotropy, exchange and the DMI, may lead to a not perfect compensation of the net magnetic moment. Often, ncAFM systems exhibit a small net moment, a phenomenon usually referred

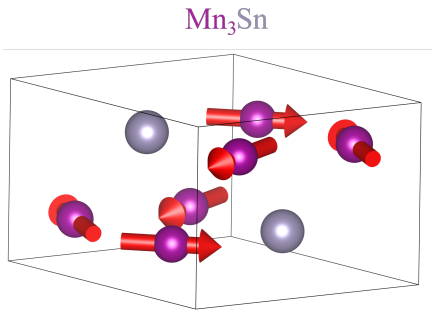

Figure 4.7: Crystal structure of the noncollinear antiferromagnet Mn_3Sn.

to as weak ferromagnetism. Despite the observed small moment, their Hall conductivity can be comparable to ferromagnets. This was demonstrated by Chen et al. on their theoretical work on cubic Mn_3Ir, the first prediction of AHE on ncAFM [46]. In the same year, Kübler et al. predicted the presence of AHE in the hexagonal systems Mn_3Sn and Mn_3Ge [47]. Moreover, they also showed the enhancement of the Berry curvature close to band crossings near the Fermi energy. Soon after, the experimental observation of AHE in Mn_3Sn was achieved by Nakatsuji et al. [48].

The Hall conductivity was believed to be proportional to the magnetization of the magnetic material. Therefore, due to their compensation, no Hall response would be expected in antiferromagnets. For instance, the two systems highlighted in the previous section, CuMnAs and Mn_2Au, follow this empirical rule. For many systems, this would lead to the overlooking of certain symmetries that do not allow a nonzero AHE response. In both of these cAFM, the crucial symmetry is the combination of $\mathcal{PT}$. However, a different set of symmetry restrictions might still allow nonzero Hall conductivity, without the requirement of a nonzero net moment.

The ncAFM Mn_3Sn shown in Fig. 4.7 preserves the $\mathcal{P}$ symmetry. Given that any magnetic system breaks $\mathcal{T}$, we have that the $\mathcal{PT}$ symmetry combined is broken. Therefore, the anomalous Hall conductivity might be nonzero unless other symmetries present in the system force it to be otherwise.

A key symmetry operation used to study the anomalous Hall conductivity in the triangular ncAFM is the mirror operation. And the focus lies on how it transforms the Berry curvature integrated over the entire Brillouin zone, as it is the source of the intrinsic AHE. The Berry curvature acts as a magnetic field, hence it is treated as an axial vector. Under a mirror operation $\mathcal{M}$, the component of the axial vector normal to the mirror plane is not affected, while the in-plane components flip their sign. We conclude that if a system contains a mirror symmetry, the Berry curvature parallel to the mirror plane is odd, $\mathcal{M}\Omega_{\parallel}(k_x, k_y, k_z) = -\Omega_{\parallel}(k_x, -k_y, k_z)$, while the normal projection is even, $\mathcal{M}\Omega_{\perp}(k_x, k_y, k_z) = \Omega_{\perp}(k_x, -k_y, k_z)$ (Fig. 4.8 (a)).

The Hall conductivity is obtained after integrating the Berry curvature over the Brillouin zone [44]:

$$\sigma_{\alpha\beta} = -\frac{e^2}{\hbar}\int_{\mathrm{BZ}} \frac{\mathrm{d}^3k}{(2\pi)^3}\Omega_{\alpha\beta}(k) \ . \tag{4.1}$$

Therefore, for a non-vanishing transverse conductivity the Berry curvature $\Omega_{\alpha\beta}(k)$

should not be odd in k. Let us consider a system with the following symmetries, $\mathcal{P}$ and $\mathcal{M}_{[100]}$ (mirror plane normal to the x-axis). Starting with the Berry curvature normal to the [100] plane. The $\mathcal{M}_{[100]}$ symmetry implies that $\Omega_{yz}(k_x, k_y) = \Omega_{yz}(-k_x, k_y)$ and the $\mathcal{P}$ symmetry implies that $\Omega(k_x, k_y) = \Omega(-k_x, -k_y)$. As schematically shown in Fig. 4.8 (b), the function $\Omega_{yz}(k)$ does not necessarily integrate to zero and thus a conductivity in the direction σ_{yz} might be expected. On the other hand, since $\mathcal{M}_{[100]}\Omega_{xy}(k_x, k_y) = -\Omega_{xy}(-k_x, k_y)$ it forces a Berry curvature distribution over the k-space that integrates to zero (see Fig. 4.8 (c)). The same is true for Ω_{zx}. As a result our system only allows σ_{yz} while constraining σ_{xy} and σ_{zx} to be zero.

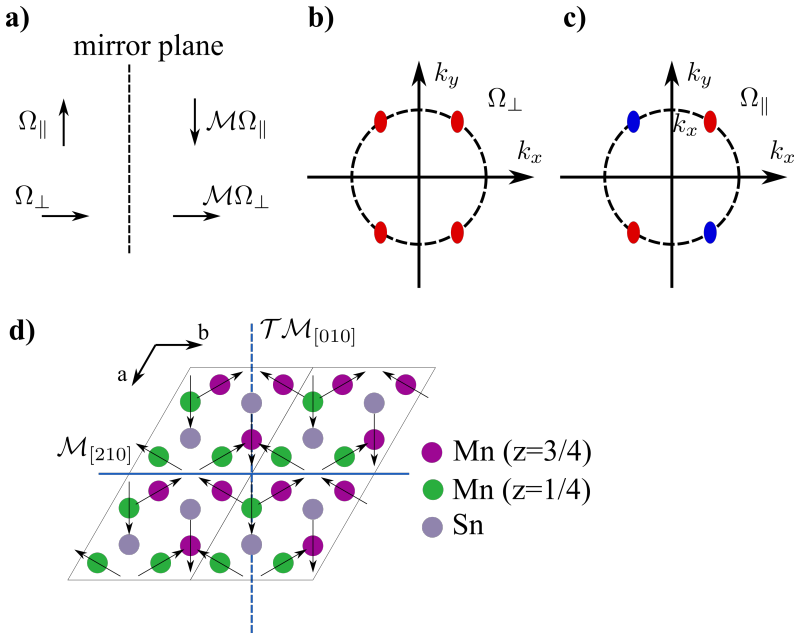

Figure 4.8: **a)** Berry curvature under a mirror operation. **b)** and **c)** Schematic of the Berry curvature over the k-space when both symmetries $\mathcal{P}$ and $\mathcal{M}_{[100]}$ are present. The red and blue marks represent opposite signs of Ω, and the dashed circle is just a guideline. While **b)** depicts the behavior of $\Omega_\perp$ (or Ω_{yz}), **c)** shows $\Omega_\parallel$ (or Ω_{xy} and Ω_{zx}). **d)** Crystal structure of Mn_3Sn projected onto the basal plane. Two mirror planes are highlighted, $\mathcal{M}_{[210]}$ and $\mathcal{T}\mathcal{M}_{[010]}$.

Part of this thesis focused on the ncAFM Mn_3Sn. It crystallizes in a hexagonal structure with space group $P6_3/mmc$ (Fig. 4.7). Its Mn atoms form a kagome lattice in the c-plane, and below the Néel temperature of $T_N = 420$ K, an inverse triangular spin configuration is stabilized with a small magnetization on the order of a few $10^{-3}\mu_B$/Mn [100, 101]. In Fig. 4.8 (d), the crystal structure and spin configuration together with two of its mirror symmetries are shown. These two mirror symmetries impose restrictions on the Berry curvature as discussed above. The mirror symmetry $\mathcal{M}_{[210]}$ imposes on the in-plane components of the Berry curvature to be odd with respect to the plane. As a consequence, the tensor component σ_{xy} of the Hall conductivity, linked to the out-of-plane Berry curvature, is zero. This is in agreement with the experimental observation for temperatures above 50K [48]. Below it, a large anomalous conductivity is measured. It is speculated to stem from an out-of-plane canting of the moments, resulting in a nonzero chirality and consequently a contribution from the topological Hall effect.

Even if the crystal structure remains the same, the mirror symmetries may be preserved or broken by altering the magnetic order. This means that when undergoing a magnetic phase change, the symmetries present and hence the Hall conductivity tensor might change as well. One example is the family of magnetic antiperovskites $ANMn_3$ (A = Ga, Sn, Ni). Based on symmetry analyses and theoretical calculations, Gurung et al. demonstrated that for two different non-collinear magnetic orderings, the anomalous Hall conductivity is zero and finite [102]. They consider the system $GaNMn_3$ and its two noncollinear phases denoted Γ_{5g} and Γ_{4g}. Both phases exhibit a coplanar geometry, with the magnetic moments on the (111) plane. The Γ_{5g} phase, belonging to the magnetic space group $R\bar{3}m$, has three mirror planes perpendicular to the (111) plane - $\mathcal{M}_{[10\bar{1}]}$, $\mathcal{M}_{[0\bar{1}1]}$ and $\mathcal{M}_{[\bar{1}10]}$. The combination of these three mirror planes results in a zero Hall conductivity tensor in all directions. While this magnetic phase inhibits the presence of the AHE effects, the Γ_{4g} allows it. The same mirror operations are only preserved when combining time-reversal symmetry to them, forming the space group $R\bar{3}m'$.

Together with AHE, the Anomalous Nernst effect has also been investigated in Mn_3Sn, being theoretically predicted and observed in bulk systems [69, 70, 103]. Additionally, both effects seem to show a large influence on the distance of the Fermi level to Weyl nodes [104, 105]. Specifically, while the AHE reaches a maximum when the Fermi level is located the Weyl point, the ANE response becomes zero. However, the ANE shows a large enhancement when the Fermi level is slightly shifted from the node.

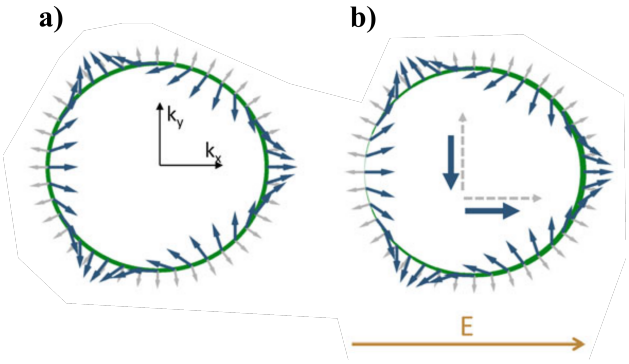

Figure 4.9: **a)** Illustration of the Fermi level of a ncAFM in equilibrium. Blue and gray arrows correspond to the spin orientation and velocity direction, respectively. **b)** An applied electrical field redistributes the electrons, resulting a longitudinal and transverse spin currents. Adapted from [106].

Apart from the anomalous conductivity characteristic of ferromagnetic systems, ncAFM also possesses a spin polarized current similar to that of ferromagnets. In 2017, Železný et al. reported the presence of spin-polarized currents in Mn_3Sn and Mn_3Ir [106]. As depicted in Fig. 4.9 (a), in contrast to a FM, the spins point along different directions at the Fermi level. Since the system is compensated, the integral of the spin of all electrons is zero. when an electrical field is applied to the system, the electrons are redistributed along the Fermi level. Now, together with a net electrical current parallel to the field, also a spin current emerges. Moreover, the spin current exhibits a longitudinal and transverse

components. A key difference to ferromagnetic systems, where in the absence of spin-orbit coupling, where the spin current would only be longitudinal.

Together with their prediction of spin polarized currents, Železný et al. also proposed an AFM magnetic tunnel junction. Given the presence of a longitudinal spin current, phenomena like STT and GMR (or TMR) are expected. The STT offers a mechanism to control the magnetic order, while a GMR behavior would enable the realization of an AFM-based memory device with potentially large readout signal. Recent reports show the first results on the observation of TMR on MTJ based on ncAFM [107, 108]. While one publication reports TMR of 2% on a Mn_3Sn MTJ, the second one shows a TMR ratio of 100% using Mn_3Pt.

5. Detection of magnetic order in antiferromagnets

This chapter is dedicated to the detection of the antiferromagnetic order, taking advantage of either electrical or thermoelectrical effects.

We start with the out-of-plane SAF system. We demonstrate its possible application as magnetic memories where an analog-like value is stored in AFM domains. Furthermore, a memristor functionality is shown with two important properties - multilevel states and long-time stability. Imaging the magnetic order with magnetic force microscopy (MFM) provided two main results. Firstly, it confirms our interpretation that the second-order magnetoresistance is proportional to the ratio between oppositely oriented domains. And secondly, we observe large AFM domains hinting at domain wall propagation being the most likely phenomenon behind the electrical switching, in contrast to domain nucleation.

Next, we move into a "real" AFM and focus on the detection of the magnetic order in CuMnAs. Previous works had demonstrated a memory device where the information is stored on domains with the perpendicular Néel order. We show that in the same antiferromagnetic films as used earlier, we can also electrical switch between reversed states. Moreover, the detected reversed states are stable and show no sign of decay over a span of 25 hours, in contrast to perpendicular switching which decays on the time scales of seconds to minutes.

The electrical detection of the magnetic order returns an average measurement over the probed area. The longitudinal resistance probes the area between the two longitudinal contacts, whereas the transverse resistance senses the square intersection at the cross-region. Therefore, electrical detection can only provide us with the relative population between domains, and not its spatial distribution. In order to image the magnetic domains in the cAFM CuMnAs, we proposed a thermoelectric detection method combining a local heat gradient with the magneto-Seebeck effect. Employing this technique, we observe polarity-dependent 90° switching in a biaxial film and 180° switching in a uniaxial sample. In addition, for high current pulses, the fragmentation of the magnetic order into multiple nanometer-sized domains is observed. This tabletop imaging technique provides a valuable alternative to the XMLD-PEEM, which requires access to a synchrotron beam line.

Finally, we show the versatility of the thermal scan imaging as different thermoelectric effects may be exploited. The last work highlighted in this thesis combines a laser-induced thermal gradient with the ANE to image the magnetic domains of the ncAFM Mn_3Sn. In it, magnetic domains are heat-assisted written and afterward imaged with a ANE reading.

5.1 Electrical detection of the Néel vector reversal

As briefly mention on the previous chapter, the detection of the Néel vector in the cAFM CuMnAs relied on the electrical reading of the AMR response and on the optical signal from XMLD. Both phenomena are even in magnetization, that is, they can sense the axis the Néel lies along. But, its direction along the axis remains undetermined. An odd effect would be necessary to distinguish opposite oriented states, like AHE. However, in CuMnAs due to its $\mathcal{PT}$ symmetry, the AHE response is zero. And in a fully compensated SAF, the AHE signal also vanishes.

The proposed solution is the measurement of second-order magnetotransport effects. The microscopic mechanism behind it is the combination of magnetoresistances with current-induced fields. In the presence of current-induced fields, the resistance becomes a function of the current as the moments are dragged away from their equilibrium positions. The first-order, or linear, response is described by $E_i = \rho_{ij} j_j$, where ρ_{ij} relates to the current-independent resistivity. Higher-order terms describe how the resistivity depends on the current, and although high-orders are possible to be present we look only up to the second-order term. In order for the second-order response to be present the inversion symmetry must be broken in the system. The second-order transport equation may be written as $E_i = \xi_{ijk} j_j j_k$, and both the electrical field E_i and the electrical current j_i are both odd under inversion symmetry $\mathcal{P}$. It implies that the $\mathcal{P}$ symmetry has to be broken in order to ξ_{ijk} to be nonzero.

The Fig. 5.1 illustrates the mechanism responsible for the second-order term. The direction in which the AFM moments are tilted away from equilibrium depends on the Néel vector direction. In other words, since the field-like Néel spin-orbit torque is odd in magnetization ($\vec{T}_{FL} \propto \vec{M} \times \vec{\sigma}$), the equilibrium position with current differs for both states with opposite Néel vector. Therefore, when combining the spin-orbit torque with the even in magnetization AMR, the resulting second-order AMR becomes odd.

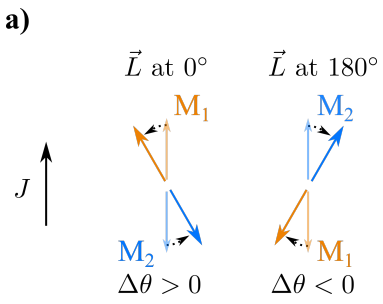

Figure 5.1: Second-order magnetotransport effect.

The displacements from the equilibrium position are usually very small, and the corresponding signal is as well. To improve the sensitivity of the measurement a homodyne detection method is used. In our detection experiments, a low frequency (143 Hz) probing current flows through the system. Using lock-in amplifiers 4 signals are measured simultaneously, that is, longitudinal and transverse AMR resistance, and the first and second harmonics of each. From Ohm's law,

it follows:

$$V = R(\theta)I \tag{5.1}$$

$$V \approx \left(R(\theta_0) + \left.\frac{\partial R}{\partial \theta}\right|_{\theta_0} \Delta\theta\right) I\,, \tag{5.2}$$

where θ is the angle of the Néel vector and θ_0 its equilibrium position, i.e., position at zero current. Assuming now the alternating AC current, $I = I_{AC}\sin(\omega t)$ and that $\Delta\theta = \delta\theta I$, where $\delta\theta$ is a proportionality factor, we get:

$$V = R(\theta_0)\, I_{AC}\sin(\omega t) + \left.\frac{\partial R}{\partial \theta}\right|_{\theta_0} \delta\theta I_{AC}^2 \sin^2(\omega t)\,. \tag{5.3}$$

From here we can identify three terms, one DC component V^{dc}, a 1st harmonic $V^{1\omega}$ and a 2nd harmonic $V^{2\omega}$:

$$V^{DC} = \frac{1}{2}\left.\frac{\partial R}{\partial \theta}\right|_{\theta_0} \delta\theta I_{AC}^2 \tag{5.4}$$

$$V^{1\omega} = R(\theta_0) I_{AC}\sin(\omega t) \tag{5.5}$$

$$V^{2\omega} = \frac{1}{2} I_{AC}^2 \left.\frac{\partial R}{\partial \theta}\right|_{\theta_0} \delta\theta \sin\left(2\omega t - \frac{\pi}{2}\right)\,. \tag{5.6}$$

The signal oscillating at the same frequency as the AC current, that is the 1st harmonic signal $V^{1\omega}$ corresponds to the linear response, while the 2nd harmonic signal $V^{2\omega}$ oscillating at double the frequency corresponds to the second-order response. The measurement of high-order magnetotransport has been used before to detect the presence of current-induced torques in ferromagnets and heterostructures [109, 110, 111]. Note that, even though the DC component contains similar information to the 2nd harmonic signal, it is difficult to disentangle the desired signal from the multiple artefacts present in DC.

An important remark on the 2nd harmonic signal is that it does not only contain contributions from the current-induced fields. Thermoelectric effects induced by Joule heating are quadratic in current, and therefore are observed on the 2nd harmonic signal. Such effects could be for instance ANE and SSE. Whether they are treated as measurement artefacts or a detection tool depends on the final intent behind the measurement.

Lastly, often instead of the voltage signals, the resistance signals are used. They are defined as $R^{1\omega} = V^{1\omega}/I_{AC}$ and $R^{2\omega} = V^{2\omega}/I_{AC}$. Thus, the 1st harmonic of the resistance is independent of the probing current whereas, the 2nd is linear to it. The linear dependence on current of the 2nd harmonic resistance signal can be used to identify and disentangle the desired signal from artefacts present on the overall measured signal. One common such artefact comes from the AC source, as it does not provide a "perfect" sinusoidal curve hence containing undesired signals at multiple frequencies. As the linear response resistance does not depend on the current, it can be more easily compared between measurements at different probing currents (Joule heating effects might slightly change the resistance value). When comparing 2nd harmonic measurements, however, these values should be normalized by the probing current.

5.2 Synthetic antiferromagnet

Let us first consider the SAF system illustrated in Fig. 4.2 . The experimental results were obtained on a $50 \times 5\ \mu m$ Hall bar (Fig. 5.2 (a)), through which an AC current flows. The longitudinal and transversal resistances' first and second harmonic signals are simultaneously measured.

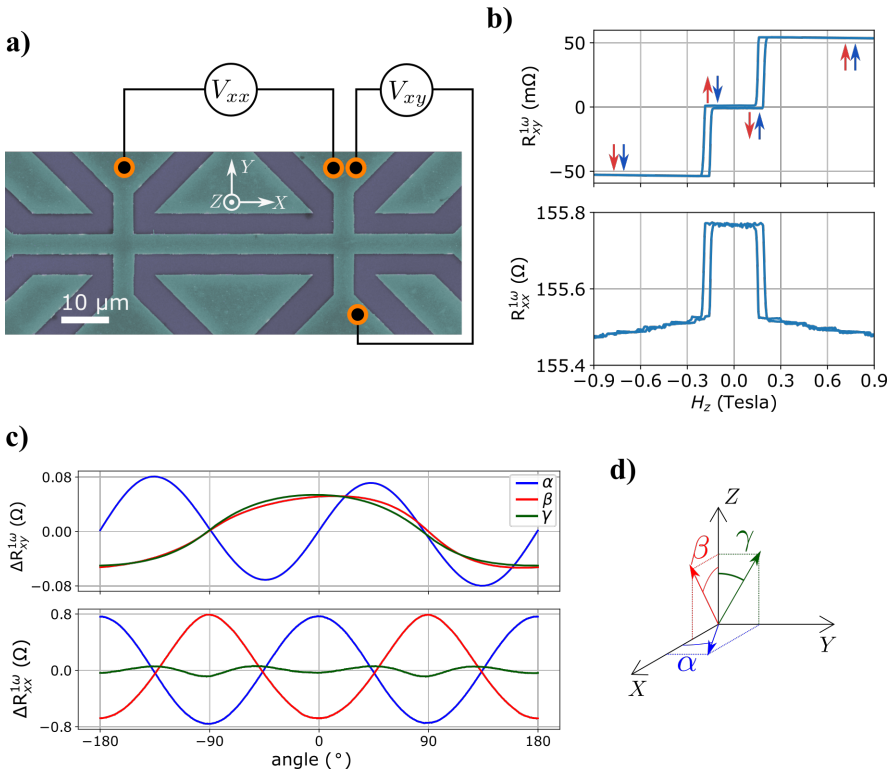

Figure 5.2: Experimental setup for electrical detection in out-of-plane SAF. **a)** Scanning electron micrograph of the Hall bar device, with schematics corresponding to the measurement setup. **b)** Linear-response of both transversal and longitudinal resistances measured during an out-of-plane field sweep. No distinction between the two antiparallel states is observed, besides a small signal in $R_{xy}^{1\omega}$ due to an unintentional asymmetry between the ferromagnetic layers yielding a small net magnetic moment. **c)** Linear responses $R_{xy}^{1\omega}$ and $R_{xx}^{1\omega}$ as a function of three primary angle rotations, depicted in **d)**.

In Fig. 5.2 (b), it is shown an out-of-plane field sweep, while measuring both resistances' linear response, $R_{xy}^{1\omega}$ and $R_{xx}^{1\omega}$. The longitudinal resistance ($R_{xx}^{1\omega}$) shows a GMR-like behavior, a step-like function with a low resistance level when both moments are aligned after the spin-flip, and a high-resistance level otherwise.

In $R_{xy}^{1\omega}$, mainly the anomalous Hall effect is present, where the four possible magnetic states are observed. Despite the sample being nominally compensated, in practice, its ferromagnetic layers are not completely identical, resulting in a nearly compensated SAF. Most likely due to the different layers each FM layer is grown on top of. Hence, slight variation of magnetic moment or magnetic anisotropy can be expected. Consequently, when removing the out-of-plane field, once the spin-flip field (≈ 0.15 T) is crossed, the magnetic order changes into a deterministic uniform antiparallel state. Such unintentional property helps us

prepare the magnetic state via external means, enabling the study of the sample's response when in a single magnetic domain. Therefore, two antiparallel states can be defined as the states obtained after saturating the sample in negative and positive out-of-plane fields.

In order to identify and quantify the magnetoresistances in the system, the 1st harmonic (linear response) signals were analyzed during field sweeps and field rotations. From the out-of-plane field sweep, the anomalous Hall effect and giant magnetoresistance are estimated. The other effects are identified when studying the angle dependence of the signals as function of the three main rotation angles. These field rotation were performed at 2 T, above the spin-flip field of the sample. This way we can approximate our system to a single net magnetization, similar to a single ferromagnet system. The data was analyzed through a Fourier series decomposition,

$$f(x) = \sum_{n=0}^{N} a_n \sin(nx) + b_n \cos(nx) \tag{5.7}$$

The observed magnetoresistances are summarized into the table 5.1, where it is specified from which angle rotation and signal ($R^{1\omega}_{xx}$ or $R^{1\omega}_{xy}$) the respective amplitude per sheet was estimated. The field rotation data is shown in Fig. 5.2 (c), and the angles are defined in Fig. 5.2 (d).

Operation	Signal	MR	Amplitude per sheet
β-rotation	$R^{1\omega}_{XX}$	AMR	72 $m\Omega$
γ-rotation	$R^{1\omega}_{XX}$	cAMR	5.6 $m\Omega$
γ-rotation	$R^{1\omega}_{XX}$	SMR	1.1 $m\Omega$
B_Z sweep	$R^{1\omega}_{XY}$	AHE	54 $m\Omega$
B_Z sweep	$R^{1\omega}_{XX}$	GMR	25 $m\Omega$ (0.16 %)

Table 5.1: Magnetoresistances present in the SAF system and their amplitudes.

We aim at detecting the two AP states using the higher-order terms of resistivity, which do not depend on a net magnetic moment. We apply an AC current of 5 mA (RMS) with a frequency of 163 Hz through the Hall bar device and focus on the longitudinal signal appearing at double the frequency. In Fig. 5.3 (a), it is shown a clear distinction between the two AP states in the $R^{2\omega}_{xx}$ signal during a field sweep along the current direction H_x. In order to be sure of the sample's magnetic state, data was only collected while sweeping the field from 0 to ± 2 T. Measuring only for increasing magnitude of the field, we avoid the uncertainty in the magnetic order when crossing the in-plane spin-flip (≈ 1 T) from high fields, since both AP states are energetically equal. Prior to each of these four sweeps, an out-of-plane field of ± 0.3 T was applied and removed to set one of the two AP states.

From the 2nd harmonic signal expression (eq. 5.6), we conclude there are two main conditions for it to be nonzero. First, the current-induced field should lead to the displacement from the equilibrium position, or $\delta\theta \neq 0$. In other words, the current-induced field should not be parallel to the moment. Secondly, the resistance for positive and negative currents should be different, or $\frac{\partial R}{\partial \theta}\Big|_{\theta_0} \neq 0$. For this reason, in an out-of-plane system with current flowing in the sample's plane, there is no 2nd harmonic signal expected at zero field. It is a symmetric

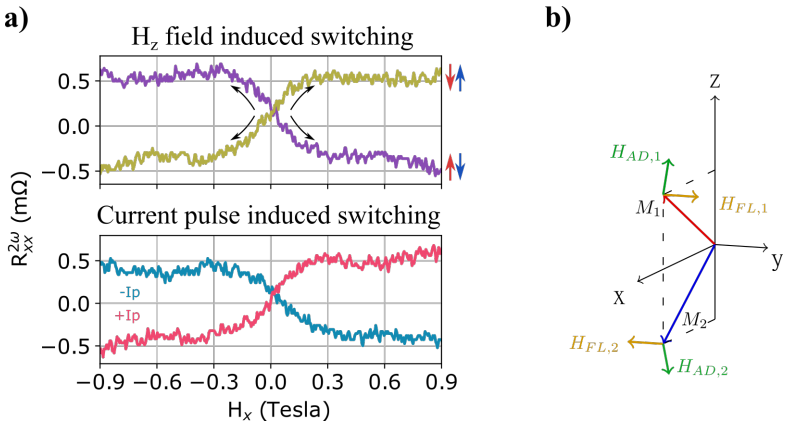

Figure 5.3: Second-order magnetoresistance in the out-of-plane SAF. **a)** Second harmonic signal of the longitudinal contacts measured for an in-plane field sweep. In order to unambiguously know the magnetic state of the SAF, these sweeps were measured always starting from zero field after the application of out-of-plane ±0.3 T to fully magnetize the whole sample with a particular antiparallel state. Instead of applying the out-of-plane field, similar signal is obtained when an electrical pulse is sent through the sample at $H_x = -0.9$ T. The antiparallel states are fully determined by the pulse polarity. **b)** Sketch of the current-induced fields. Here, we highlight the staggered nature of the antidamping field as well as its out-of-plane projection which energetically favors one antiferromagnetic state.

point (a maximum or minimum) of the main magnetoresistances present in the system - AHE, GMR and AMR. In Fig. 5.3 (a) it can already be observed that, only at zero field, the states can not be detected or distinguished.

There are two possible current-induced effective fields, a perpendicular field H_{FL}, that points along with the spin polarization $\vec{\sigma}$ and is responsible for the field-like torque. The second field is the antidamping H_{AD}, which is proportional to $\vec{M} \times \vec{\sigma}$. The probing current flowing through the device oscillates at a relatively low frequency compared to the intrinsic frequencies of the system. Thus, we can assume the moments are following their respective effective field at every instant. In Fig. 5.3 (b), it is shown an illustration of the current-induced fields when an external field is along x. It can be readily seen that H_{FL} is always staggered, and tilts the moments along the in-plane angle. Which for an external field along x yields no 2$^{\text{nd}}$ harmonic signal. Thus in such a configuration, the H_{FL} would not contribute to the signal. The H_{AD}, on the other hand, at zero field is non-staggered, pointing along $\pm x$. However, once the moments start to cant towards x, H_{AD} now has a z projection which is staggered. Moreover, this projection of the effective field leads to a change of resistance (both AMR and GMR) which is different for both current polarities. Therefore, the $R_{xx}^{2\omega}$ signal observed stems from a current-induced antidamping field. The detection of the two AP states is then possible because the H_{AD} changes sign for the two antiferromagnetic states, tilting the moments in opposite directions for the same current direction. When reversing the magnetic order, it results in signals with the same amplitude and in opposition of phase. As confirmed by the symmetric signal while changing the sign of the external field or changing between AP states.

Besides the detection of the two AP states, the staggered out-of-plane com-

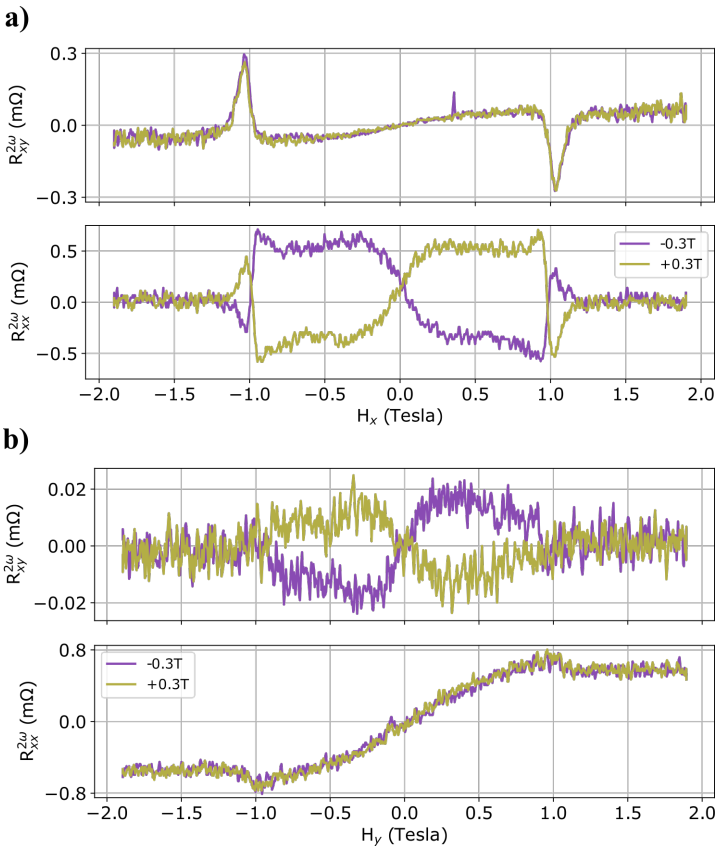

Figure 5.4: Nonlinear responses in SAF as a function of H_x and H_y. $R^{2\omega}_{xy}$ and $R^{2\omega}_{xx}$ measured during field sweeps along x and y, in **a)** and **b)** respectively. Prior to each sweep an uniform state was prepared applying an out-of-plane field.

ponent of H_{AD} can also be used to induce polarity-dependent electrical switching between the two states. In Fig. 5.3 (a), we compare the electrical switching with the out-of-plane field writing. Electrical current pulses of 1.83×10^7 A/cm^2 and 10 ms long were applied at -0.9 T. Firstly, independently of the state set previously by the external field, the pulse's polarity uniquely determines the sample's final state. Secondly, the signal's amplitude is comparable to that of the field writing, suggesting a full magnetic reorientation across the whole volume between the longitudinal contacts. The system can then be used as a magnetic memory, where both the readout and writing do not depend on an intentional unbalance of the FM layers. Also worth mentioning is the possibility of a two-terminal device, in contrast to a geometry where the Hall response is measured. Moreover, while the external field is along x, probing the $R^{2\omega}_{xx}$ has the advantage of being clean of thermal effects, such as ANE and SSE. They are present instead in $R^{2\omega}_{xy}$.

In Fig. 5.4 , we show the 2$^{\text{nd}}$ harmonic signals for both field sweep directions. As before, each sweep is measured after an out-of-plane field is applied in order to select one antiparallel state. We observe the thermal contributions in $R^{2\omega}_{xy}$ and $R^{2\omega}_{xx}$ when applying an external field along x and y, respectively. These background signals are associated with anomalous Nernst effect and / or spin-Seebeck effect. Both exhibit the same symmetry, making it difficult to distinguish the individual contributions. They originate from an out-of-plane thermal gradient which is induced by Joule heating. The total thermal contribution is around 0.055 mΩ

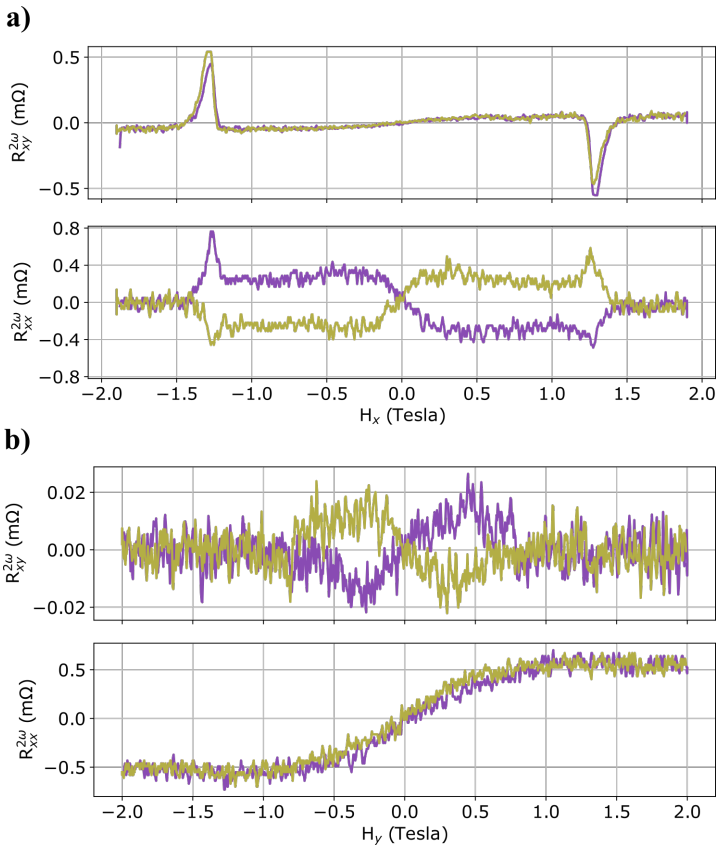

Figure 5.5: Nonlinear responses in an asymmetric SAF as a function of H_x and H_y. $R^{2\omega}_{xy}$ and $R^{2\omega}_{xx}$ measured during field sweeps along x and y, in **a)** and **b)** respectively. Prior to each sweep an uniform state was prepared applying an out-of-plane field. Note that, here the probing current was 4 mA, instead of the 5 mA used in the symmetric system. While comparing both signals, they should be scaled accordingly.

per sheet. Note that, there are 10 squares between the longitudinal contacts, therefore the signal is larger by tenfold.

It is noteworthy that the method of detecting the antiparallel state, which involves applying an external field along the x-axis and measuring $R^{2\omega}_{xx}$, is not the only available option. An alternative approach involves applying the field along the y-axis and measuring $R^{2\omega}_{xy}$, as illustrated in Fig. 5.4 and Fig. 5.5 . However, this option has its own drawbacks. Besides the smaller magnitude of the signal, it is sensitive to the cross area of the device where the current density and current lines are not uniform. Furthermore, the most relevant disadvantage is that even though with an external field along the y-axis the order parameter can be detected, the electrical switching is not achievable. The incapability to switch can be understood from a macrospin perspective as the absence of a staggered component along the easy axis of the current-induced effective field.

When applying a field along the x-axis, $R^{2\omega}_{xy}$ exhibits peak features at the vicinity of the spin-flip field. These can be intuitively explained by the flattening of the energy barrier. That is, with an increased in-plane field and lower barrier between equilibrium states, the current-induced field can promote a larger displacement from the equilibrium position or even a switching between min-

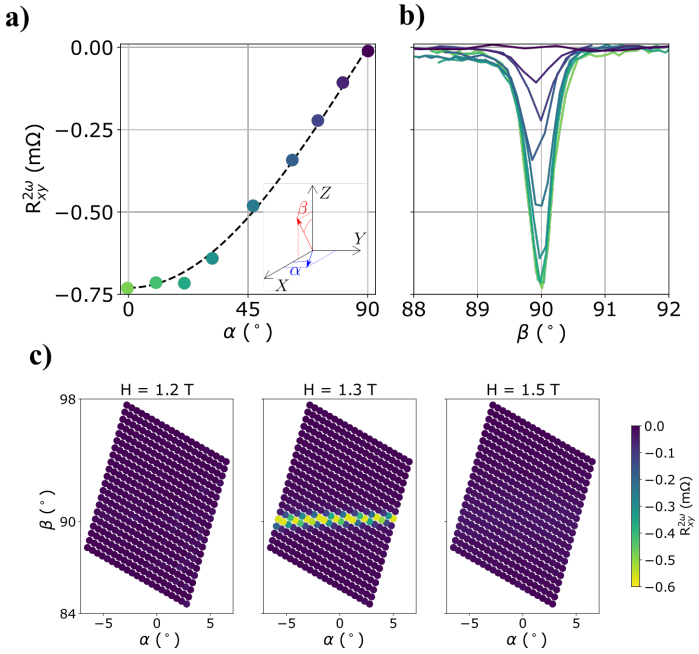

Figure 5.6: Second harmonic peak feature in $R_{xy}^{2\omega}$ measured on the asymmetric system. **a)** and **b)** show the dependence of the peak feature on the azimuthal and polar angle respectively, at a constant magnitude of the field of 1.3 T (or SF field). The dashed line on **a)** works as a guide-line to the eye in order to highlight the cosine dependence on the azimuthal angle, α. The angular precision needed for such measurements is presented in **b)** as the width of the peak as a function of the out-of-plane angle, β, is narrower than one degree. **c)** angular maps where the $R_{xy}^{2\omega}$ is scanned around its maximum, i.e., the x axis (or $\alpha = 0°$ and $\beta = 90°$) at different field magnitudes.

ima. Hence, yielding a larger nonlinear response. In the transverse contacts, $R_{xy}^{2\omega}$, the peak feature stems from the anomalous Hall effect from the small net moment. The same should be seen in the longitudinal contacts, $R_{xx}^{2\omega}$, where the signal would originate from the AMR. However, due to a small misalignment of the in-plane field, a switching event is observed at the same field range the peak is expected. The expected behavior is observed and shown here on a different sample, which is intentionally non-compensated. Its layer composition nominally only differs on the thickness of the top ferromagnetic layer, being four repetitions of [Co(0.2nm)/Ni(0.7nm)] instead of three. Here, no switching event occurred during the in-plane sweep and the peaks can be easily identified. Fig. 5.5 shows the 2$^{\text{nd}}$ harmonic signals measured in the asymmetric system. The results from the asymmetric SAF are always specified, and if not mentioned the compensated system is considered.

The influence of the net moment on the nonlinear response can be evaluated by comparing the characteristics of nominally compensated and non-compensated samples. A notable difference observed is the height of the peak features in $R_{xy}^{2\omega}$, with a value of 0.06 mΩ per mA in the symmetric system and nearly double at 0.13 mΩ per mA in the asymmetric one. This is consistent with the hypothesis that these features originate from the anomalous Hall effect and are therefore affected by the net moment within the sample. However, when the external field

is applied along the y-axis, the signal observed in $R_{xy}^{2\omega}$ is similar between the two samples, with a maximum signal between antiparallel states of roughly 4 $\mu\Omega$ per mA. When the antidamping effective field is the dominant one it drives the moment only along the azimuthal angle, as illustrated in Fig. 5.2 (d). Therefore, in this geometry, $R_{xy}^{2\omega}$ contains no contribution from the AHE, but from AMR. Thus, demonstrating that combining the AMR and nonlinear response can yield a detection method independent of the net moment of the system. Regarding the $R_{xx}^{2\omega}$ during the x-sweep, it is not so straightforward to compare as there are two main contributions into it, AMR and GMR. Nevertheless, the signals at 0.5 T for the symmetric and asymmetric samples are 0.18 and 0.15 mΩ per mA, respectively, which indicate that this is a reliable technique that can be applied to both fully-compensated and non-compensated systems.

A few extra words regarding the peak feature. In Fig. 5.6 (a) and (b) it is shown the dependence of the feature on the azimuthal and polar angles, respectively. The data shown was measured on the asymmetric SAF sample. A cosine dependence on the in-plane angle α is observed, supporting the picture that this feature is of SOT origin, showing its maximum when the angle between magnetization and spin polarization is maximum. At the different values of α, a scan on β was performed, Fig. 5.6 (b). Here, we would like to highlight how narrow the feature is with respect to the out-of-plane angle. In other words, the precision required to align the external field with the sample plane has to be smaller than 1°. Finally, another evidence supporting our interpretation is summarized in Fig. 5.6 (c). Angular scans around the x-axis (or $\alpha = 0°$ and $\beta = 90°$) were measured at different field magnitudes. The feature is not moving in parameter space as a function of H, and it is only observed at spin-flip field.

The change in magnetoresistance as a function of the electrical pulse height is shown in Fig. 5.7 . As discussed before in $R_{xx}^{1\omega}$ no change is observed, as the linear response can not distinguish between the two AFM states (Fig. 5.7 (b)). On the other hand, the non-linear response changes its reading depending on the current density of the pulse (Fig. 5.7 (c)). It does not show a step-like dependence expected from a complete reorientation of the magnetic order at one specific critical current. Instead, a smooth non-linear curve between the two fully saturated states is observed, with multiple levels in between. Such behavior results from the partial switching across the sample allowing both AP states to coexist with a given ratio. Thereby adding extra functionality to the system as a multilevel memory, where the signal-to-noise ratio of the measurement limits the number of different states.

All the data was acquired at 0.9 T and before each electrical pulse one strong pulse with negative polarity was applied to reset the state (Fig. 5.7 (a)). At each current density, the measurement was repeated ten times and its mean value of the average over 1 minute is plotted. The error bars correspond to the standard deviation of the average value. The electrical switching mechanism is reproducible as hinted by the narrow error bars (inset of Fig. 5.7 (c)).

The field-assisted switching mechanism was briefly described above when describing the peak features observed in the 2$^{\text{nd}}$ harmonic signals. As an in-plane external field H is applied, the moments cant towards the external field. Considering no current is flowing and no in-plane anisotropy, in equilibrium, the system can be described simply by considering the polar angles, θ_1 and θ_2, and setting

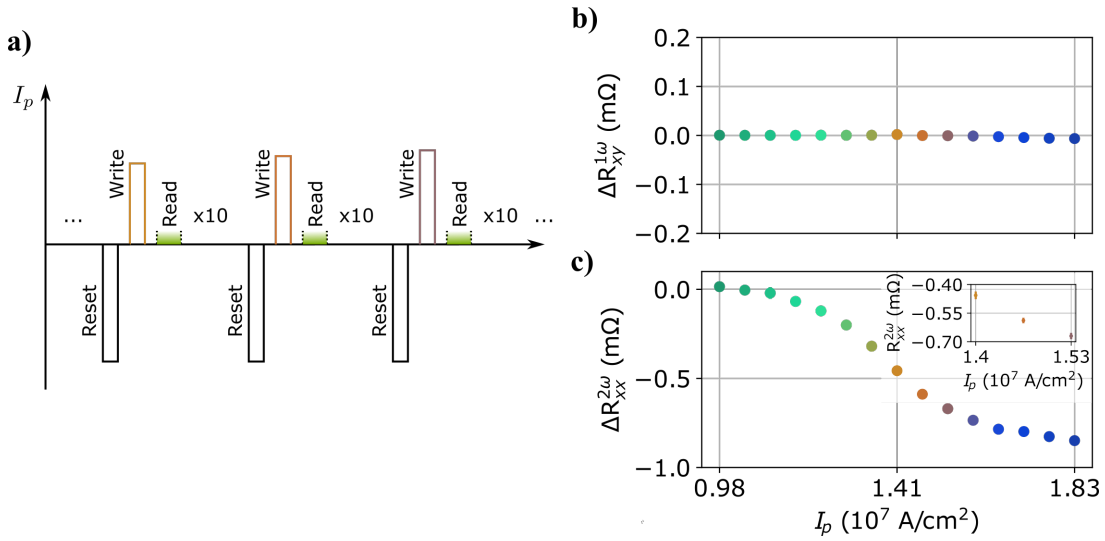

Figure 5.7: Multilevel electrical switching in SAF. **a)** Pulse sequence used to probe the dependence of the switching signal on the pulse height, as well as the reproducibility of the switching signal. The change in longitudinal resistance as a function of the pulse amplitude at 0.9 T, in both 1$^{\text{st}}$ and 2$^{\text{nd}}$ harmonics, **b)** and **c)** respectively. Each point is the average of a set of 10 pulses, and in-between writing pulses the magnetic state is reset by a -1.83×10^7 A/cm^2. The error bar is the standard deviation of the mean value and it can be better seen in the inset.

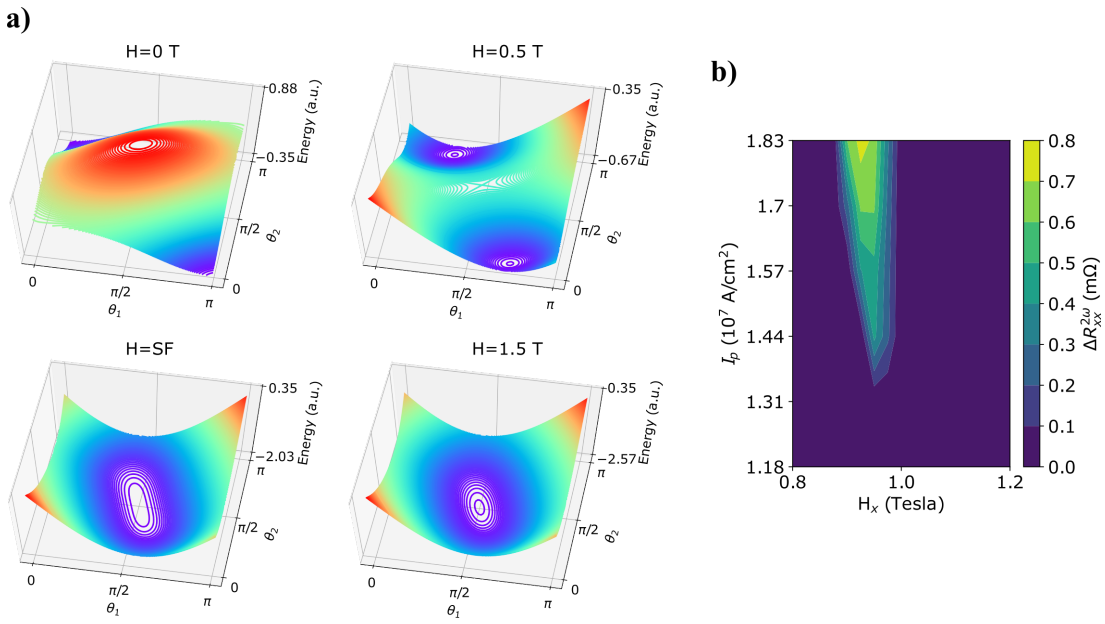

Figure 5.8: Field-assisted electrical switching in the out-of-plane SAF. **a)** The energy function plotted as a function of θ_1 and θ_2, at different field strengths. At the spin-flip, the system transitions from showing two equal minima to a single global minimum. (These are a result of simulating the asymmetric system. Nevertheless, the key idea still holds for the symmetric sample.) **b)** Two-dimensional map of the switching signal in $R^{2\omega}_{xx}$ as a function of the current pulse height, I_p, and external field, H_x.

the azimuthal angles φ_1 and φ_2 equal to φ_H, the in-plane angle at which the field is applied. In Fig. 5.8 (a), the energy landscape as a function of θ_1 and θ_2 is plotted for different magnitudes of H. Anisotropy, interlayer exchange and Zeeman energies were taken into account in the energy function. There are two equal minima for small fields that correspond to swapping the anti-parallel states ($\uparrow\downarrow$ to $\downarrow\uparrow$, or vice-versa). Both moments cant towards the sample plane as the field increases, thus the two minima come together at $(\theta_1, \theta_2) = (\pi/2, \pi/2)$. This point, when the moments align with the field is the spin-flip (SF) field. After it, there is only this one equilibrium point. Although the simulation was done for the asymmetric sample, the same applies to the symmetric system and it gives us an intuitive picture of the field-assisted switching.

Fig. 5.8 (b) presents a two-dimensional map of the switching signal as a function of the current pulse height, I_p, and external field, H_x. The signal is quantified as the difference in $R_{xx}^{2\omega}$ between two current pulses with opposite polarity but equal magnitude at a fixed external field H_x. As expected, no switching is observed above the spin-flip field, as the system has a single equilibrium position in this regime. Additionally, the onset of switching is shifted to higher current densities as the external field is weaker or the energy barrier is higher.

Besides the reproducibility, we also observe long retention of the written magnetic state. While electrically writing a new state, the need for an in-plane magnetic field is twofold. As already mentioned above, the field is required in order for the antidamping field H_{AD} to acquire a staggered out-of-plane component. Secondly, a higher in-plane field lowers the energy barrier separating the two AP states, consequently decreasing the electrical switching onset. The barrier also governs the long stability of the stored information in the memory. Hence, for a magnetic storage application, the external field may be removed to enhance the robustness of the memory. This idea is shown in Fig. 5.9 , where a multidomain state was prepared at 0.9 T and read after a one-hour gap at zero field. We start by electrically writing two saturated states, following a sequence of $(-I_p, I_p, -I_p)$ with $I_p = 1.83 \times 10^7$ A/cm^2. The fourth pulse is a weaker pulse at 1.6×10^7 A/cm^2 writing a multidomain state. The signal is measured again after one hour, demonstrating the stability of the magnetic order. The last sequence of $(-I_p, I_p)$ pulses is used as a reference of the full scale of the signal and makes sure there is no drift of the offset level.

An electrically written multidomain state was imaged with magnetic force microscopy (MFM). Fig. 5.10 (a) shows a section within the main channel of the Hall device, where two distinct regions colored blue and green are observed, corresponding to the two AP states. Large AFM domains spanning microns are present compared to domains in a crystal AFM as CuMnAs [93, 92]. Interestingly, a zoomed-in scan focusing on the domain walls shows that they have a larger contrast, comprising darker and lighter stripes together running along the domain wall (Fig. 5.10 (b)). The double stripe signal likely stems from a net dipole moment at the center of the domain wall, as a result of the dipole interaction between layers. Such an assumption is also consistent with the fact that the two stripes never alternate between them. For example, in the bubble domain seen in Fig. 5.10 (c), the lighter (darker) stripe is always adjacent to the brighter (darker) domain. The same is observed throughout the sample (Fig. 5.10 (b)).

In our interpretation of the nonlinear response signal ($R_{xx}^{2\omega}$), it is directly

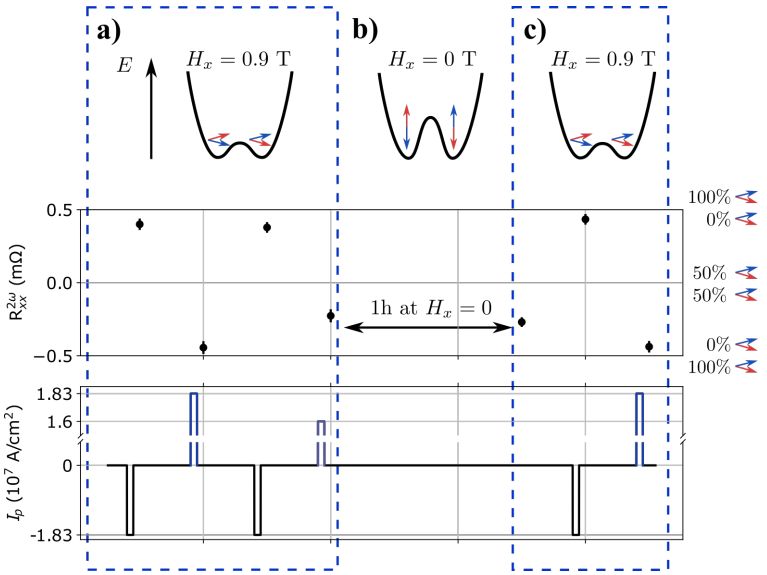

Figure 5.9: Robust SAF memory. After the preparation of a multidomain state at 0.9 T, the external field is removed for one hour. The magnetic state is probed again remaining at the same relative signal of the two saturated states. **a)** Sketch of the energy landscape as a function of the external field. **b)** $R^{2\omega}_{xy}$ signal, where each point is the average over 1 minute reading and the error bar the standard deviation. **c)** Electrical pulses applied before each reading.

sensitive to the relative population of both AP states. To further support our interpretation, we compare the 2$^{\text{nd}}$ harmonic signal with the ratio in area of both AFM domains imaged with MFM. The measured 2$^{\text{nd}}$ harmonic signal while preparing the multidomain imaged in MFM is shown in Fig. 5.10 (d). We start by writing the two saturated states and then the multidomain one. From it we should expect a close to 30/70 ratio in population, which is in good agreement with the 25/75 we obtain from the MFM scans.

To conclude, our work demonstrates the possible application of perpendicularly magnetized SAF as magnetic memories where a analog-like value is stored in AFM domains, in contrast to conventional binary computation. Furthermore, a memristor functionality is shown with two important properties - multilevel states and long-time stability. This memristive behavior is highly sought after in order to realize a neuromorphic computer. Spintronics devices are good candidates to achieve such behavior, as their resistance value may be tuned via magnetic textures such as domain walls [112]. For instance, in Lequeux et al. [113], a synaptic behavior is observed in a magnetic tunnel junction while exploiting the possibility to shift the position of a magnetic domain wall inside a single ferromagnetic layer. Their signal, similar to our work, corresponds to the relative area between two oppositely oriented domains. They use a free FM layer and a SAF structure as reference for the TMR effect. Alternatively, we propose a new spintronic memristive device where a compensated SAF is the active element of the device and the multiple states are encoded in the ratio of AFM domains, at the expense of a weaker signal's strength.

Comparing a nominally compensated with a non-compensated system, we can further support that the electrical switching and nonlinear response detection

do not rely on a non-zero net moment. However, both processes writing and reading, still require an external field which can hinder the use of these systems in future technological applications. Imaging the magnetic order with magnetic force microscopy provided two main results. It confirmed our interpretation of the nonlinear signal where we see a good agreement with the population distribution. And secondly, we observe large AFM domains hinting at domain wall propagation being the most likely phenomenon behind the electrical switching, in contrast to domain nucleation.

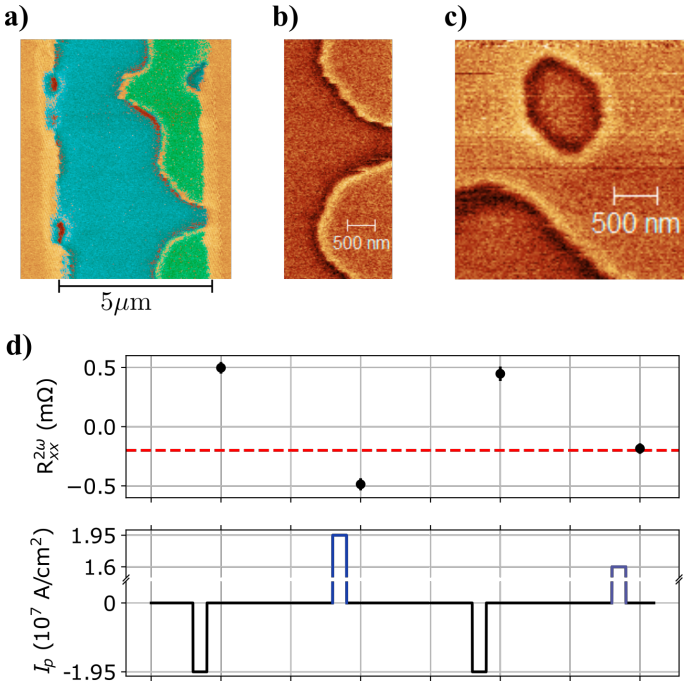

Figure 5.10: Antiferromagnetic domain walls in SAF - comparison between 2nd harmonic measurement and MFM. **a)** Section of the Hall bar scanned with MFM. Large domains are observed as blue and green regions (edited colors for clarity). **b)** Zoomed-in area inside **a)**. There is a small contrast difference between domains, and a larger contrast at the domain walls. **c)** Bubble-like domain observed inside the cross area of the Hall device. The domain walls are seen as a dark and light features side-by-side. Likely to arise from a net in-plane moment at the domain wall center - charged domain walls. **d)** Electrical preparation of the multidomain state prior to the MFM scan. From the electrical measurement a 30% / 70 % population is expected.

5.3 CuMnAs

5.3.1 Second harmonic detection

We focus our attention now on the bulk cAFM CuMnAs and how to detect its magnetic order. It shares some similarities with the previous SAF system. They share the $\mathcal{PT}$ symmetry, rendering a null AHE response. Likewise, we will take advantage of the nonlinear response of the AMR to detect the magnetic order. The key difference between the two systems is their anisotropy. Whereas the perpendicularly magnetized SAF requires an in-plane field to yield a nonzero nonlinear response and to achieve electrical switching, the in-plane magnetized CuMnAs does not have such restrictions.

In the out-of-plane SAF system, an external field is required for the anti-damping field to have a staggered out-of-plane component and hence favoring a deterministic switching. With an in-plane magnetization and the Néel spin-orbit torque present in CuMnAs which acts as a field-like torque no external field is required. The current-induced field is then always staggered and has a projection along the easy axis, resulting in a reorientation of the magnetic order. The electrical manipulation of the collinear moments may be succinctly described as an electrical current pulse favors a Néel vector perpendicular to it.

The following electrical measurements were carried out on devices fabricated from a 10 nm thick CuMnAs film grown by molecular beam epitaxy on a GaAs substrate and protected by a 3 nm Pt layer. The Fig. 5.11 (a) shows a 4 μm wide Hall cross device with added contacts to enable simultaneous detection of longitudinal and transverse signals. We will start by discussing two measurement configurations used to observe electrical switching in the CuMnAs. These are the two cases that yield the maximum AMR signal, either in linear or nonlinear response. Recalling the AMR expressions in equations 3.3, we conclude that their maximum linear response signal comes from rotating the Néel vector by 90°. Moreover, depending on which contacts, longitudinal or transverse, the measurement configuration should be chosen accordingly. For instance, to detect the reorientation of the magnetic order in the longitudinal contacts $R_{xx}^{1\omega}$, the probing current should flow parallel or perpendicular to the Néel vector. On the other hand, to observe the 90° rotation in the transverse contacts $R_{xy}^{1\omega}$, the current should be at ±45° with the axis of the magnetic order. These two cases are illustrated in Fig. 5.11 (b). In the first case, denoted as AC90, the electrical current pulses and the probing current are parallel or orthogonal. In the second one denoted AC45, the probing current is ±45° with the writing pulses. This symmetry of the AMR measurement was clearly shown by Wadley et al.[2].

Regarding the nonlinear response, the same two conditions discussed for the SAF apply here. The current-induced field should lead to a tilting of the moments, and such deflection should result in a resistance change which is different for both current polarities. Thus, to maximize the nonlinear response, the probing current should not be perpendicular to the Néel vector and we should be in a configuration where we maximize the first derivative of the AMR. The table in Fig. 5.11 (c) sums up in which measurement configuration both linear and nonlinear responses are expected.

The key result, the identification of Néel order reversal in a cAFM, is summarized in Fig. 5.12 . Starting with the measurement configuration AC90, we send

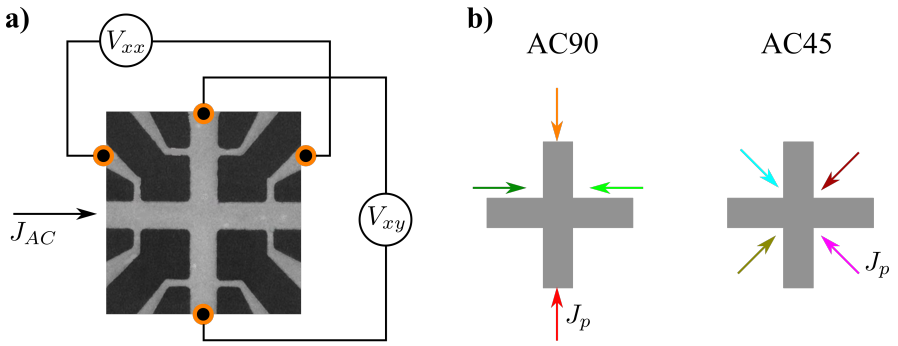

c)

		AC90	AC45
V_{xx}	1ω	✓ *	×
	2ω	×	✓ **
V_{xy}	1ω	×	✓ *
	2ω	✓ **	×

Figure 5.11: Experimental setup for electrical switching and detection of the magnetic order in CuMnAs. **a)** Scanning electron micrograph of the cross-bar device with contacts allowing to measure longitudinal and transverse resistances along x and y axes. **b)** Two measurement configurations, AC90 where the probing current is orthogonal or perpendicular to the writing pulses, and AC45 where the probing current is at ±45° with the writing pulses. **c)** Table summarizing where to expect a switching signal, for each measurement configuration. * shown in [2] and ** shown in [114].

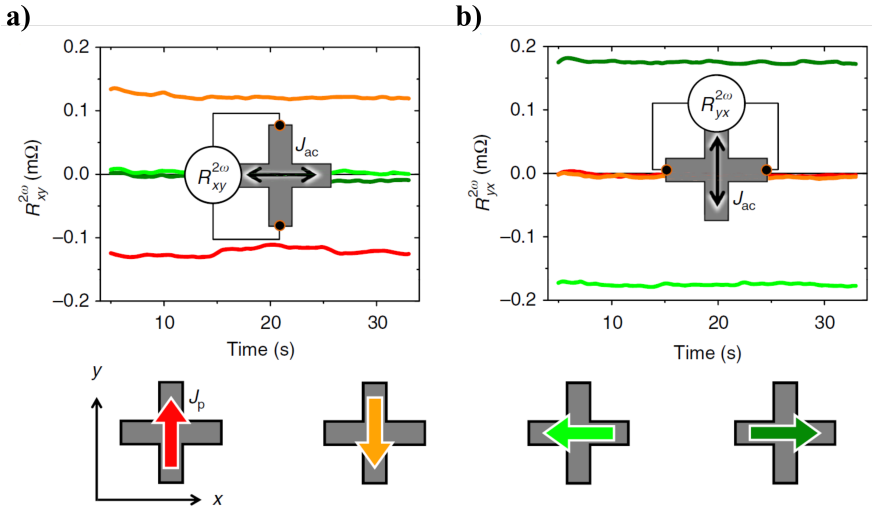

Figure 5.12: Symmetry of the 2nd harmonic signals in AC90. **a)** $R^{2\omega}_{xy}$ readout after a sequence of pulse along the ± x and ± y directions. **b)** Same as **a**, with $R^{2\omega}_{yx}$ readout, that is, the probing current is along the y axis. From [114].

20 ms long writing pulses J_p of amplitude 11 mA along the four directions defined by the cross. After each pulse, a probing current at 143Hz and 2 mA RMS flows along the x or y directions and the transverse nonlinear response is measured accordingly. In Fig. 5.12 (a), the probing current flows along the x axis and we observe a different signal for the pulses along the ± y directions and zero signal for the pulses along ± x directions. As discussed above, this sequence of pulses set the Néel vector parallel or perpendicular to the probing current direction, which corresponds to the maximum derivative of the transverse AMR. However, the green pulses set the moments aligned with the current-induced fields, resulting in no deflection of the moments and thus no 2$^{\text{nd}}$ harmonic signal. This interpretation of the 2$^{\text{nd}}$ harmonic signal is corroborated in Fig. 5.12 (b), as now the probing current is sent in the y direction, and the situation reverses. We can now distinguish the reversed magnetic order written by the green pulses, but not the pulses along the ± y directions.

From the table in Fig. 5.11 (c), we should also expect a signal in $R_{xx}^{1\omega}$. Fig. 5.13 (a) and (b) show both the $R_{xy}^{2\omega}$ and $R_{xx}^{1\omega}$ signals after a sequence of pulses along +y,+x,-y,-x directions. Indeed, as expected the linear response $R_{xx}^{1\omega}$ differentiates only between states whose axes are rotated by 90°. Each point corresponds to an averaged signal over 30 s and the error bars correspond to the standard deviation. The 1$^{\text{st}}$ harmonic of the longitudinal resistance includes the small AMR contribution (smaller than 1%) on top of the large isotropic resistance of the device. Additionally, the latter can show a significant thermal drift, for instance after each writing pulse. Still, we observe a clear switching signal in $R_{xx}^{1\omega}$.

Both signals, $R_{xy}^{2\omega}$ and $R_{xx}^{1\omega}$ share the same trend when plotted against the writing pulse amplitude, showing as well a common threshold (Fig. 5.13 (c)). This implies the common mechanism behind the two signals, magnetic reorientation. The monotonous increase after the current onset might be ascribed to the multiple magnetic domains which require different current amplitudes to switch. With an increasing writing current amplitude more and more domains might be controlled. In Fig. 5.12 (d), the dependence of both signals on the probing current is shown. We further confirm the source of the 2$^{\text{nd}}$ harmonic signal as the magnetoresistance's nonlinear term, since it exhibits a linear behavior on current amplitude. In turn, the linear response is independent of the probing current amplitude. Both dependencies follow the predicted behavior shown on equations 5.6.

Not only the 2$^{\text{nd}}$ harmonic signal allows us to detect a 180° rotation of the magnetic moments, but it brings another advantage, the long stability of the readout signal. Fig. 5.14 (a) shows a 25 hour measurement of $R_{xy}^{2\omega}$ after a pulse along +y and -y, which exhibits no sign of decay within this time scale.

In the SAF system, Pt layers were grown adjacent to the FM layers in order to have a spin accumulation at the interfaces, and thereby exert a torque on the magnetic moments. Likewise, the same could be happening here and it raises the question of whether the observed electrical switching is due to a Néel spin-orbit torque or a spin accumulation at the CuMnAs/Pt interface. To evaluate the effect of Pt on the electrical switching, we performed the same switching experiments on a reference sample. Both samples belong to the same 10 nm CuMnAs wafer, however during the Pt evaporation half of the wafer was masked. The reference sample was then obtained from the masked area, not containing the Pt layer

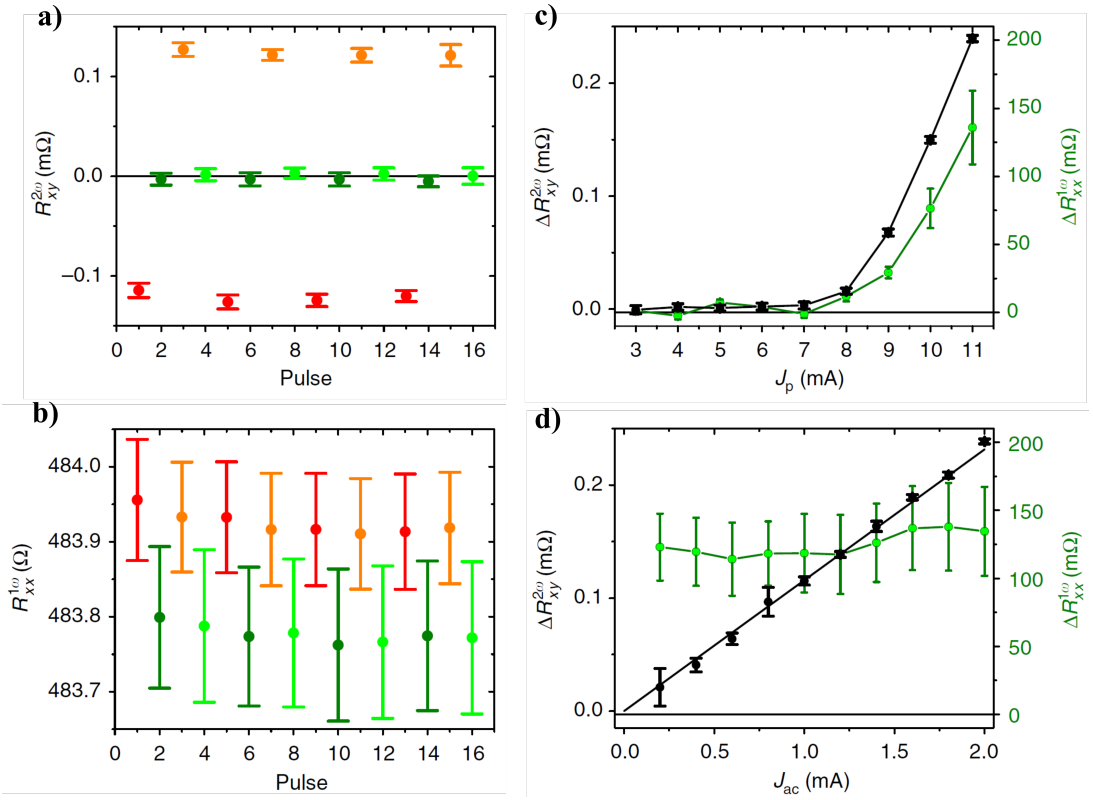

Figure 5.13: Comparison of 1st and 2nd harmonic signals. **a)** and **b)** $R^{2\omega}_{xy}$ and $R^{1\omega}_{xx}$ signals measured for four sequences of writing pulses along +y,+x,-y,-x directions. **c)** and **d)** First and second harmonic signals measured as a function of the amplitude of the writing and probing current, respectively. From [114].

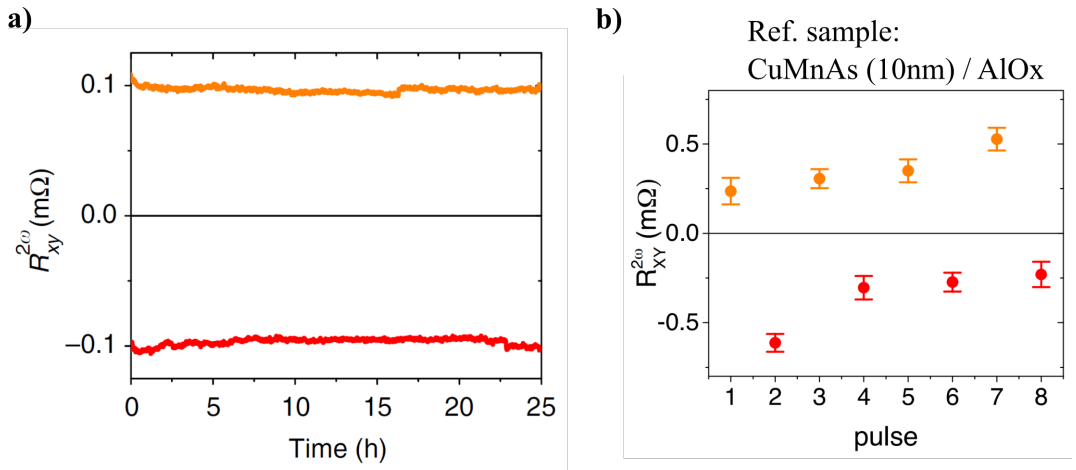

Figure 5.14: Long stability of the 2nd harmonic signal and reference sample without Pt layer. **a)** A 25 hour measurement of $R^{2\omega}_{xy}$ after a +y and a -y writing current pulse. **b)** $R^{2\omega}_{xy}$ measurement on a reference sample without the Pt layer. Adapted from [114].

but sharing the CuMnAs layer. The reference sample is a four-contact cross bar device with 10 μm wide bars, patterned into the CuMnAs/AlOx film.

We measured the transverse 2$^{\text{nd}}$ harmonic signal $R_{xy}^{2\omega}$ as a response to writing pulses along the $\pm$y directions. The probing current amplitude was 1 mA in RMS and the current pulses were 20 ms long and 9 mA in amplitude. The measured $R_{xy}^{2\omega}$ behaves just like the sample with the Pt layer, as it is shown in Fig. 5.14 (b). Even though the writing current is lower for the reference sample, 9 mA compared to the 11 mA before, we should take the shunting effect from the Pt into account and compare the current density inside the CuMnAs layer.

The sheet resistance of the CuMnAs/Pt/AlOx sample is around 100 Ω which is approximately four times lower than the sheet resistance in CuMnAs/AlOx. Therefore, in the Pt containing sample, only 1/4 of the total current flows through the CuMnAs while 3/4 goes in the Pt. we can now compare the current densities flowing in the CuMnAs layers. While in the sample with Pt, the 11 mA corresponds to 5.3×10^6 A/cm^2, the 9 mA in the sample without Pt corresponds to 9×10^6 A/cm^2. Note that in the reference sample, stronger writing pulses are required. We assign the difference to the Joule heating. The shunting through the highly conductive Pt results in a larger Joule heating effect as it scales quadratically in current. In fact, between these samples, the Joule heating is 4 times larger in the sample with Pt, for the same current in the CuMnAs.

Both, the SHE in Pt or from the Rashba-Edelstein effect at the interface result in a nonstaggered spin polarization $\vec{\sigma}$. In this case, only the current-induced antidamping field as a staggered component given by $\vec{\sigma} \times \vec{M}_1$ and $\vec{\sigma} \times \vec{M}_2$, with $\vec{M}_2 = -\vec{M}_1$. However, this remains inefficient at promoting a magnetic reorientation event. Due to the anisotropy in CuMnAs with a strong out-of-plane hard axis, the antidamping field which points along the out-of-plane direction is not suitable for switching.

Going back to our CuMnAs/Pt sample, we show that the studied sample shows an easy plane anisotropy allowing us to set the Néel vector along in direction in the plane. To illustrate this, we use now the measurement configuration AC45 described in Fig. 5.11 (b). Here, the current pulses are sent through two legs of the cross device simultaneously so that at the center of the device the current lines are mainly flowing diagonally. Keeping the probing current along the x direction, both 1$^{\text{st}}$ harmonic signal $R_{xy}^{1\omega}$ and 2$^{\text{nd}}$ harmonic signal $R_{xx}^{2\omega}$ are shown in Fig. 5.15 (a) and (b). This is the usual configuration where the electrical switching is detected in the $R_{xy}^{1\omega}$ signal. Here, we show that this signal is also accompanied by a signal in $R_{xx}^{2\omega}$.

While the signal observed in $R_{xy}^{1\omega}$ shows a significant decay in a range of minutes, the 2$^{\text{nd}}$ harmonic signal $R_{xx}^{2\omega}$ is remarkably stable (as observed for the AC90 case). Fig. 5.15 (c) highlights this discrepancy with 12 hour measurements after each pulse. As hinted by the pulse height dependence of the switching signal (Fig. 5.13 (c)), we have a system comprising multiple magnetic domains. A possible mechanism behind the multidomain nature of our samples is the magnetostriction effect. With the coupling between magnetic order and crystal lattice, after a writing pulse the magnetostriction drives the randomization of the Néel vector within a semicircle around the initial setting direction. Thus, since the linear response is sensitive to the relative population of domains lying along orthogonal axes, this effect can explain the vanishing 1$^{\text{st}}$ signal.

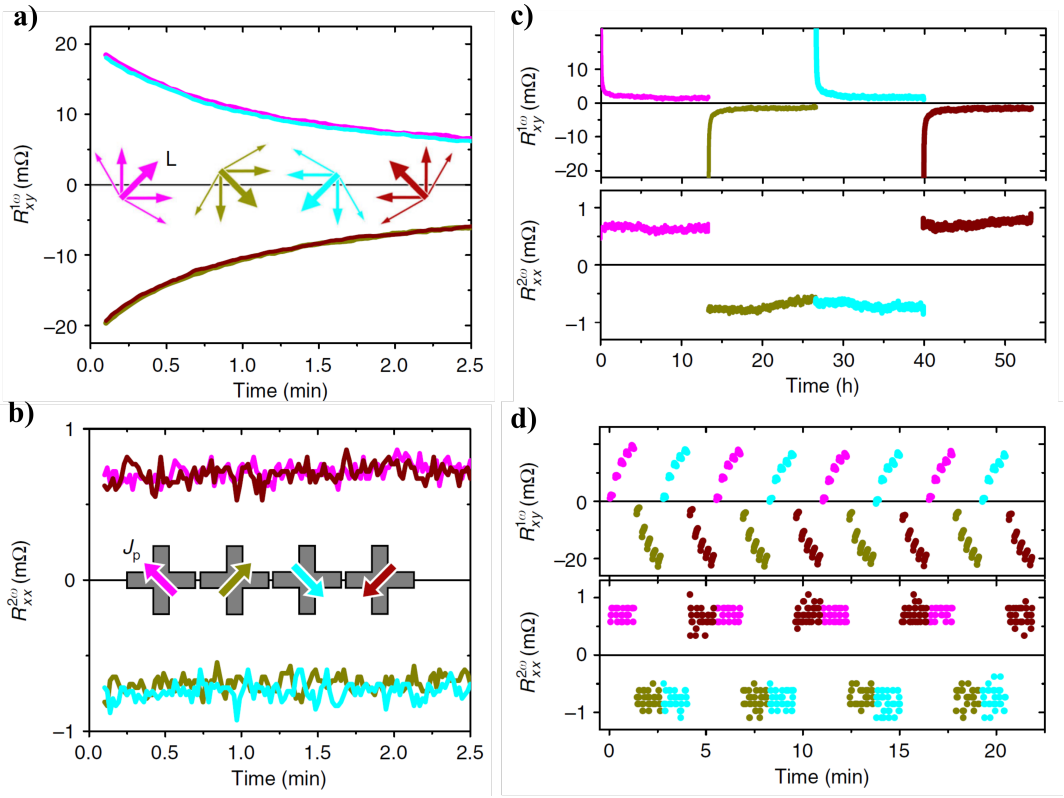

Figure 5.15: Electrical switching in CuMnAs in AC45 configuration. **a)** and **b)** Measurement of 1st harmonic signal $R_{xy}^{1\omega}$ and 2nd harmonic signal $R_{xx}^{2\omega}$ after a sequence of writing pulses along directions rotated by ±45° from the main cross axes. **c)** Same as **a)** and **b)** for 12 hours probing measurements after each pulse. **d)** Dependence of both signals on the number of consecutive pulses before changing the pulsing angle. From [114].

Yet, the magnetostriction mechanism being even in magnetization, it can not drive a sign flip of the Néel vector. Therefore, a finite difference between the initial setting direction and its opposite remains over time. Note that the nonlinear response senses the difference between oppositely oriented domains.

Another interesting distinct aspect between the 1st and 2nd harmonic signals is their respective behavior when a train of pulses is sent before changing the pulse direction (Fig. 5.11 (d)). In the 1st harmonic signal, we observe memristive multilevel characteristics on top of the strongly relaxing 90° reorientation signal. In turn, the same memristive effect is not visible in the 2nd harmonic signal, being stable and independent of history.

In summary, in both AFM systems, the compensated out-of-plane SAF and the cAFM CuMnAs, the nonlinear term of AMR gives us a tool to electrically detect reversed magnetic states in $\mathcal{PT}$ symmetric systems, where the AHE is excluded. The key ingredient for it to be present is the broken inversion symmetry. Regarding the manipulation of the moments, in the SAF structure it is achieved via the adjacent Pt layers whereas, in the CuMnAs the Néel spin-orbit torque arises from the special symmetry conditions of the crystal lattice. A second main difference between the two is the current-induced field which is efficient at promoting deterministic switching. Due to their respective anisotropies, in

the out-of-plane SAF we take advantage of the antidamping field while in the in-plane CuMnAs we exploit the field-like torque. From an application point-of-view towards an AFM memory device, both systems offer a robust and stable 2^{nd} signal. The weak strength of the signal, however, might hinder its technological adoption. More so in the case of SAF where an external field is required to write and read the magnetic order. Nevertheless, the memristive behavior observed might render these AFM systems useful in the pursuit of neuromorphic computing.

5.3.2 Magneto-Seebeck microscopy

Electrical measurements return us a global, averaged value of the probed area. In multidomain systems, it might be a drawback as we do not have access to the actual domain distribution or how the magnetic order changes after an electrical pulse. We will now focus on imaging the magnetic order of the cAFM CuMnAs.

Microscopy techniques for imaging AFM have relied mainly on large-scale synchrotron facilities. Namely, to image cAFM X-ray magnetic linear dichroism combined with photoemission electron microscopy (XMLD-PEEM) has been used [2, 92, 115, 116]. In an attempt to achieve a more accessible imaging method, NV-diamond magnetometry was recently reported in AFM [117]. Here, we will discuss an alternative technique based on a thermoelectric response, the magneto-Seebeck effect (MSE). The MSE can be applied to a large class of materials given they are conductive. However, it does not rely on uncompensated moments or magnetic stray fields, and it is not limited to AFM systems that allow the ANE such as the ncAFM.

The MSE can be described as a global voltage generated by a localized thermal gradient, and the measured thermal voltage will reflect the antiferromagnetic texture within the localized area affected by the thermal gradient. In order to induce an in-plane thermal gradient we start by using a focused laser on the sample. This first technique is based on the scanning far-field optical microscopy (SFOM) [118]. The second approach to induce a thermal gradient utilizes a scattering-type scanning near-field optical microscopy (SNOM) [119, 120]. Here, a metal-coated tip of an atomic force microscope (AFM) is placed in close proximity to the sample surface and acts as an antenna. An incident electric field onto the AFM tip is strongly confined at the tip's apex, providing a nanoscale near-field point source. Thus the SNOM technique allows us to focus light on a much narrower spot compared to the SFOM, down to the tens of nm compared to 1 μm resolution given by the far-field approach.

In Fig. 5.16 (a) we have the Seebeck effect illustrated, as a global thermal gradient across the sample is converted into a thermal voltage V_T. However, if the in-plane thermal gradient is generated in a localized area with radial symmetry, then the induced thermal currents flowing to the left and right contacts are the same and there is no thermal voltage (Fig. 5.16 (b)). However, if this same radial thermal gradient sits at the boundary where the Seebeck coefficient changes, then the two currents flowing to the left and right are not equal in magnitude and a net thermal voltage appears (Fig. 5.16 (c)). This is the basic principle of a thermocouple, where two materials with distinct Seebeck coefficients are used. Instead of different materials, the MSE exploits the magnetic contribution of the Seebeck effect. The coefficient is even in magnetization and depends on which axis it lies on.

Exploiting this effect, we investigated how the magnetic order in CuMnAs changes when electrically reorienting the Néel vector.

In the SFOM-MSE method, we use an 800 nm wavelength cw laser beam of 1 mW focused on the sample's surface, with a full width at half maximum of 1 μm. Consequently, the laser spot induces a lateral radially symmetric thermal gradient, which in turn will lead to a thermal voltage V_T which is monitored as a function of the laser position (Fig. 5.17 (a)). The laser beam is modulated at a frequency of 1.7 kHz by an optical chopper and the thermal voltage V_T is

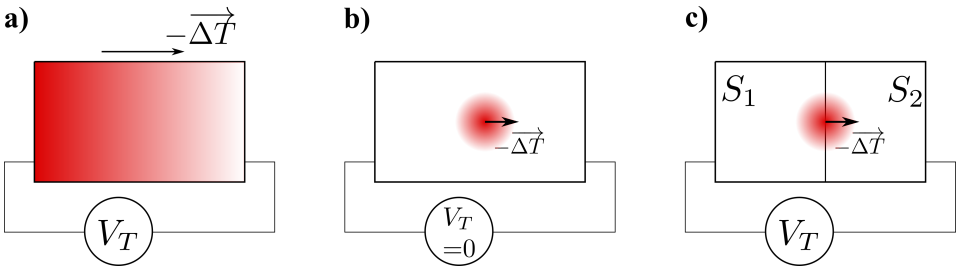

Figure 5.16: Magneto-Seebeck effect. **a)** Seebeck effect, a thermal gradient ΔT across the measurement contacts generates a thermal voltage V_T. **b)** A focused in-plane radial thermal gradient leads to no thermal voltage. **c)** However, if the radial thermal gradient sits at a boundary where the Seebeck coefficient changes then the thermal voltage does not cancel out. Due to the Magneto-Seebeck effect, magnetic domains with the Néel vector oriented along different axes exhibit correspondingly different Seebeck coefficients. Thus, this technique allows us to map domain walls.

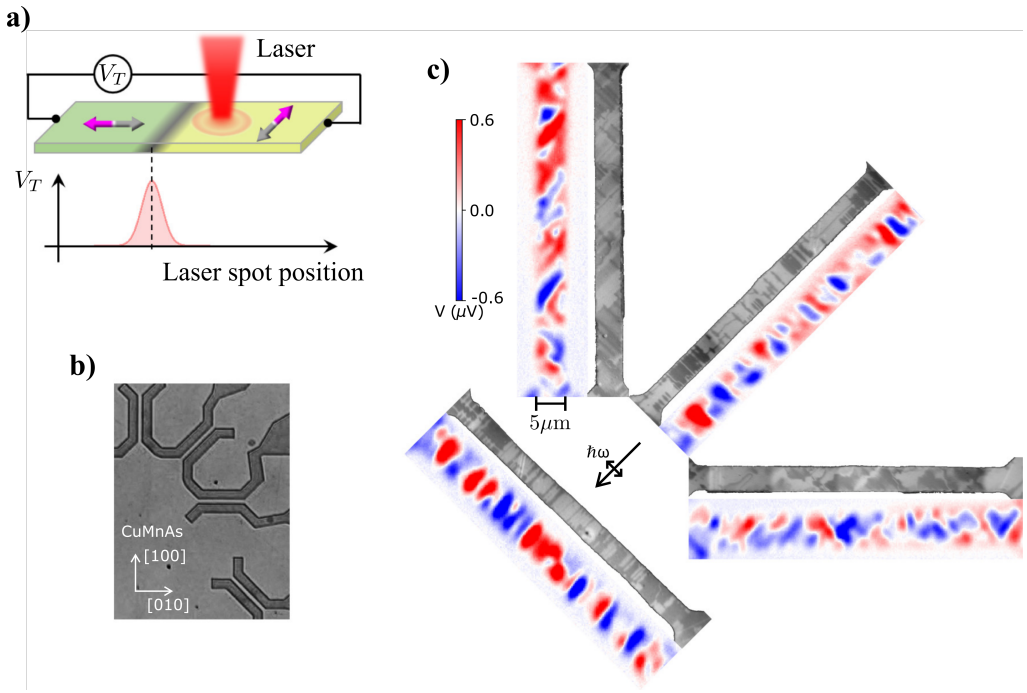

Figure 5.17: Comparison between XMLD-PEEM and SFOM. **a)** Schematics of the measurement setup for the SFOM and below the expected MSE response when scanning over a domain wall. **b)** Optical micrograph of four 50 μm long and 5 μm wide bars oriented along four different crystallographic axes of the CuMnAs. **c)** SFOM-MSE and XMLD-PEEM images side by side. The single and double-headed arrows indicate the in-plane projection of the X-ray propagation and the X-ray polarization, respectively. From [121].

measured by a lock-in amplifier.

The MSE behaves similarly to the usual Seebeck effect described above. Thus, if the induced thermal gradient is confined inside one single magnetic domain, where the Seebeck coefficient is uniform the thermal currents cancel out and no thermal signal is observed (same as in Fig. 5.16 (b)). Whereas, when the laser spot is scanned over a domain wall a net thermal current results in a finite V_T. Therefore, we conclude that our method is probing the position of domain walls and not the domains themselves, as illustrated in Fig. 5.17 (a). The signal's sign depends on which domain is on the left and right side of the domain wall.

First, we start by comparing the SFOM-MSE with the established XMLD-PEEM. We imaged four 50 μm long and 5 μm wide bars patterned along different crystallographic axes of a 45 nm thick CuMnAs film. An optical micrograph of the four devices is shown in Fig. 5.17 (b). In Fig. 5.17 (c), we compare side by side the output of both techniques. The XMLD-PEEM measurements were taken with the X-ray polarization along the $[1\bar{1}0]$. The observed light and dark contrast correspond to AFM domains with their Néel vector oriented parallel and perpendicular to the electric field of the X-ray [92]. Both domains with orthogonal axes are found, showing the dominant in-plane biaxial anisotropy.

Similar features are observed from both techniques, confirming that the main contribution to the MSE is the magnetic texture. Differences between the two images might stem from the lateral resolution and depth sensitivity of the two techniques. While the XMLD-PEEM reaches a resolution around 50 nm, the SFOM-MSE is limited by the 1 μm wide Gaussian-shaped laser spot. Despite the high lateral resolution, the XMLD-PEEM probes only a few nm from the surface layer. In turn, the MSE probes the full thickness of the thin film. Lastly, important to note is that these measurements are spaced in time. Over the 10 days gap, slight variations of the magnetic order could have taken place.

With a good agreement with the standard AFM imaging technique, we aimed to observe a correlation between SFOM-MSE and changes in the electrical resistance after current pulses. In a 5 μm wide cross bar, electrical pulses are sent through the vertical channel and the resistance $R_{\parallel}$ along the same channel is monitored. After each current pulse, a SFOM-MSE scan is performed in the area delimited by the dashed yellow box in Fig. 5.18 (a). Here, we simultaneously recorded the thermal voltage developed across the vertical and horizontal channels, V_T^V and V_T^H.

Fig. 5.18 (b) and (c) show both of the thermal signals after a train of pulses was applied with an amplitude of 9.6×10^{10} A/m^2 and duration of 20 ms. Both thermal voltages appear only when the laser shines on the respective cross channel, yielding a zero signal whenever no thermal gradient is induced inside their respective probing channels. Moreover, only the vertical channel, where the current pulses flowed, exhibits changes in the MSE maps. The horizontal channel registers no changes, besides in the intersection area. From here, we can already state that the MSE detects current-induced changes in the magnetic order.

The correlation with resistance variations is shown in Fig. 5.18 (d). We can confirm that changes in the SFOM-MSE are accompanied by changes in electrical resistance. The resistance $R_{\parallel}$ changes reversibly and reproducibly when changing the pulse polarity (inset figure). Here, our observed resistance variations of 4% are larger than the expected AMR due to a 90° reorientation of the Néel vector.

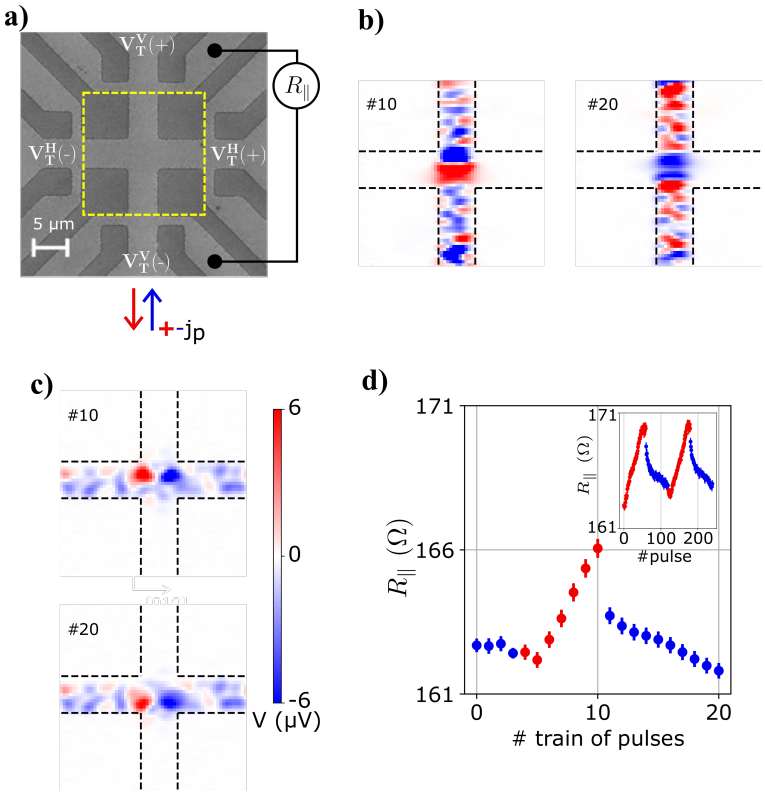

Figure 5.18: Current pulses induced changes in the SFOM-MSE maps and correlation to electrical resistance variations. **a)** SEM image of the 5 μm wide cross bar device, showing the measurement contacts geometry used. The yellow dashed line indicates the area scanned by SFOM-MSE. **b)** Vertical thermal voltage map after the pulse number 10 and 20, respectively. **c)** Same for the simultaneously measured horizontal thermal voltage. **d)** Corresponding variation of resistance after each pulse. Red and blue points corresponds to positive and negative pulses of 9.6×10^{10} A/m^2 and 20 ms. From [121].

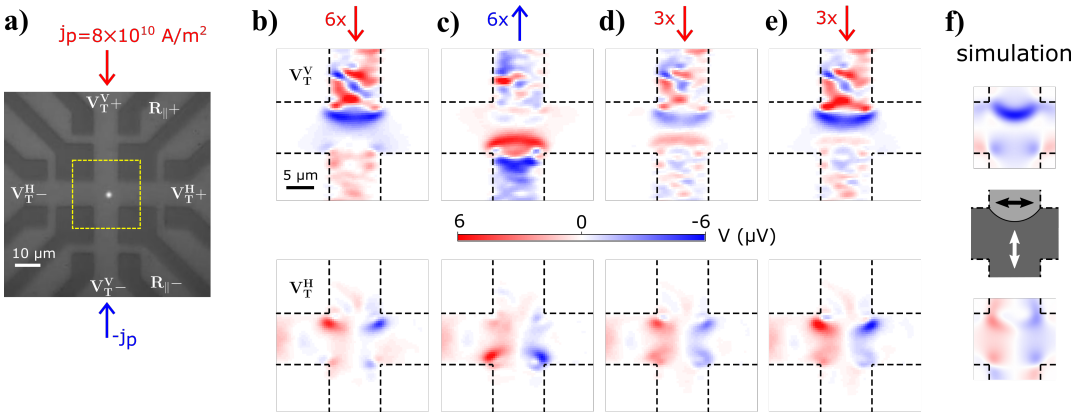

Figure 5.19: Reproducibility of the polarity-dependent switching. **a)** Micrograph of a 10 μm wide cross bar device, and the used measurement contacts geometry. The yellow dashed line indicates the area scanned by SFOM-MSE. **b) - e)** Sequence of MSE maps, vertical and horizontal thermal voltages, for alternating train of pulses. **f)** Simulated MSE maps of the vertical and horizontal voltages for a domain wall pinned at the cross corners (middle schematics). From [121].

An additional effect might be contributing to the overall variation of $R_{\parallel}$ in the multidomain CuMnAs.

The reproducibility of the electrical switching and hence of the SFOM-MSE maps is better visualized in Fig. 5.19 . The same experiment was carried out this time on a 10 μm wide cross bar device. We focused on observing the reversible switching controlled via the current polarity. To better observe it, we performed a MSE scan after each step of the following sequence of pulses $6 \times j_p, 6 \times -j_p, 3 \times j_p, 3 \times j_p$. Fig. 5.19 (b) and (c) show the MSE map after a train of 6 pulses with opposite polarities. By applying only a train of 3 pulses, an intermediate state is achieved. However, a repetition of a train of 3 pulses brings the sample to the same original state after the initial 6 positive pulses, Fig. 5.19 (e).

The Fig. 5.19 (f) offers a possible domain arrangement whose MSE signature resembles the arc-like feature observed inside the cross intersection. The calculated MSE maps for both vertical and horizontal thermal voltages are in good qualitative agreement with the measurements. It is assumed a bubble-like domain is pinned at the corners of the cross structure. The bubble domain enlarges or shrinks through an effective Zeeman gain from the staggered effective field [122, 123].

Until now, at these current densities, the electrical switching showed a reversible behavior both electrically and in the thermal scans. When applying pulses with 1.3×10^{11} A/m^2, the contrast on the MSE maps vanishes. This effect is illustrated in Fig. 5.20 . Fig. 5.20 (a) and (b) show the SFOM-MSE maps of a 5 μm wide bar before and after the current pulse. The diminishing contrast is ascribed to the shattering of the magnetic domains into sub μm sized domains. With multiple domains within our 1 μm resolution of the SFOM method, the thermal signal averages to zero. The interpretation is supported by the observation of a such phenomenon in XMLD-PEEM (Fig. 5.20 (d) and (e)).

Remarkably, when remeasuring the same device one week apart, not only the contrast is back as similar features are visible (Fig. 5.20 (c)). This hints into the role of structural defects as pinning and nucleation centers. In the XMLD-PEEM case, we have an image 4 hours after the pulse and small changes in the magnetic order are visible Fig. 5.20 (f).

The SFOM method, as a low-complexity and tabletop setup compared to the synchrotron-based XMLD-PEEM, already provides us with insightful information about the magnetic order of a fully compensated antiferromagnetic system. Yet, it faces a major limitation, its resolution is limited by the laser's wavelength and the diffraction limit. As we just discussed, the SFOM approach would be inefficient at detecting the quench switching, when the shattering results in submicron-sized domains. We propose the use of near-field optical microscopy instead of the far-field, as it is not diffraction limited achieving resolutions compared to the XMLD-PEEM in the tens of nm range.

To introduce the near-field approach or SNOM, we resolve 180° domain walls on a uniaxial CuMnAs film and their displacements induced by electrical current pulses. Fig. 5.21 (a) illustrates the mapping of a 180° domain wall with the SNOM-MSE method. In this case of a 180° domain wall, the MSE is characterized by two features together of opposite signs. Since only the changing Seebeck coefficient within the domain wall contributes to the thermal signal. Therefore, in order to visualize the domain wall, the induced thermal gradient should be of

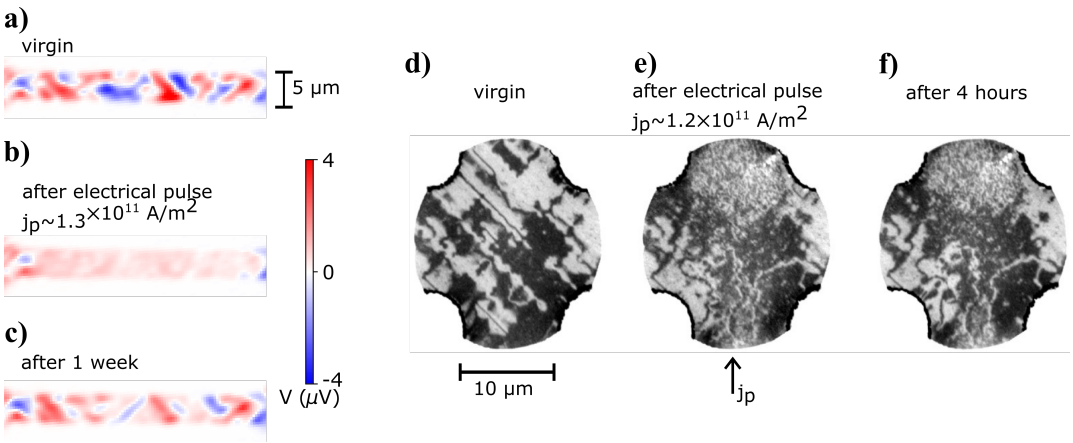

Figure 5.20: Shattering of the magnetic order. **a)** SFOM-MSE map of a 5 μm wide bar before the application of any electrical pulse. **b)** After a pulse with a current density of 1.3×10^{11} A/m^2. **c)** Thermal scan 1 week after the pulse. **d)** XMLD-PEEM image of a similar sample before a pulse, **e)** after a pulse of 1.3×10^{11} A/m^2, and **f)** 4 hours after. From [121].

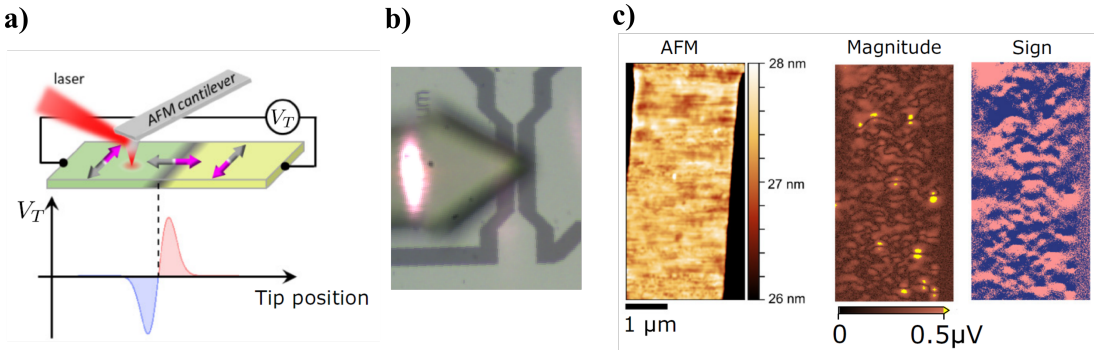

Figure 5.21: SNOM-MSE on a CuMnAs sample with uniaxial anisotropy. **a)** Schematics of the SNOM-MSE setup and expected MSE signal for a 180° domain wall. **b)** Micrograph of the scanned bar device, where the AFM tip is also visible. **c)** Result from the SNOM-MSE, from left to right: topography, magnitude of the MSE signal and its sign. From [121].

the order of the domain wall. Hence, we use the SNOM method, specifically the scattering type SNOM, where a laser light shines on and scatters off a metallic-coated tip. The SNOM was operated in tapping mode using a gold-coated Si cantilever with a tip diameter of less than 50 nm. Note that in a scattering SNOM, the spatial resolution is determined by the radius of curvature at the tip apex [119]. The thermal voltage is amplified by a low-noise preamplifier and after it demodulated at the tip-modulation frequency.

We present SNOM-MSE measurements performed on 2 μm wide bar devices patterned into a 20 nm thick CuMnAs film. Fig. 5.21 (b) shows a micrograph of the device under the AFM tip. The Fig. 5.21 (c) shows from left to right, the topography image, the magnitude of the thermal voltage V_T and its sign, all simultaneously detected. The 180° domain walls are identified as the meandering zero lines in the magnitude map accompanied by the sign change on the sign map. As most of these features have no counterpart in the topography scan, they are not correlated with defects.

In order to further build evidence on the thermal imaging of 180° domain walls, we apply current pulses and manipulate the magnetic textures back and forth by polarity-dependent switching, as shown in Fig. 5.22 . The thermal voltage is measured after each train of 22 pulses with alternating polarity. We observe that the domain walls are reversibly displaced depending on the current polarity. We found as well that a strong feature does not react to the pulses and acts as a pinning center to the domain wall. Possibly a crystal defect that pins the domain wall and contributes to a large thermal signal.

These changes observed in the SNOM-MSE are also correlated with resistance changes. The bistable switching corresponds to the resistance variation of 1 to 2 %. Since this is a uniaxial film, the AMR cannot explain it. Instead, we ascribe the change in resistance to magnetic scattering on the domain walls.

So far, we only considered a perfectly radially symmetric thermal gradient. If its radial symmetry is broken, then a net thermal current is expected along the axis that breaks the symmetry. That is, let us consider when the light spot (either far or near-field) shines at the edge of a bar device. It will lead to a net current flowing perpendicular to the bar direction. Considering the standard and isotropic Seebeck effect, it results in a thermal voltage across the bar's edges, which we have no access to. However, if the Seebeck coefficient is anisotropic, as is the case in MSE, a thermal current perpendicular to the bar might lead to a measurable voltage along the bar device. The described phenomenon or the transverse Seebeck effect is analogous to the transverse AMR. We take advantage of such an effect to support that our 20 nm thick CuMnAs film has a uniaxial anisotropy.

An asymmetric gradient at the edges of the bar devices leads to a transverse thermal voltage. Moreover, when considering the opposite edge, the net thermal gradient flips sign and hence so does the thermal voltage. This results in two edge signals with opposite polarity running across the bar. This argument still holds in a multidomain sample, given it has a uniaxial anisotropy. Since the MSE is even in magnetization, the polarity of the edge signal is not affected when scanning across a 180° domain wall.

The Fig. 5.23 (a) illustrates the transverse Seebeck effect, highlighting the edge signals and that to maximize them the Néel vector should be along one of

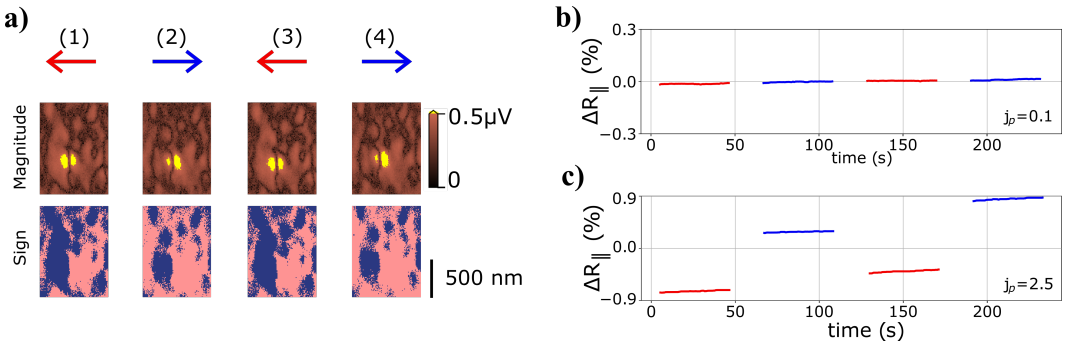

Figure 5.22: Reversible switching measured in SNOM-MSE. **a)** Maps of thermal voltage after the application of alternating pulses with a current density of 2.5×10^{11} A/m^2, indicated by the red and blue arrows on top. **b)** and **c)** Resistance variations after alternating pulses of 0.1 and 2.5 $\times 10^{11}$ A/m^2. From [121].

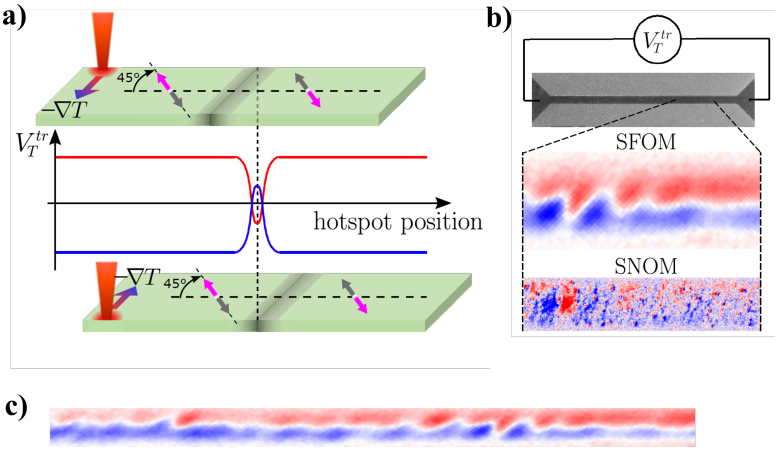

Figure 5.23: Transverse MSE. **a)** Illustration of the transverse MSE and the expected signal on a uniaxial sample with its easy axis at 45° with the bar. Comparison between SFOM and SNOM-MSE maps of a uniaxial film whose easy axis lies at 45° with respect to the bar direction. **c)** SFOM-MSE map of the whole bar device. From [121].

the axes at an angle of ±45° with the bar. In Fig. 5.23 (b), we show the MSE scans, for both methods SFOM and SNOM, in a bar device which is 45° rotated from the previous device. We observe the edge signals on both thermal maps, which were not present in Fig. 5.21 (c). This is in good agreement with our interpretation of the uniaxial anisotropy of the film. Consequently, the lack of the transverse Seebeck effect means that the sample in Fig. 5.21 is parallel or perpendicular to the easy axis. This observation is in agreement with previous studies where, CuMnAs films with thickness around and below 20 nm grown on GaP tend to exhibit a dominant uniaxial anisotropy along the [100] or [010] crystallographic direction in CuMnAs [88, 124].

When compared, the SNOM yields a higher spatial resolution map with a finer structure, which in the case of SFOM is mostly averaged out. Regardless, the edge signals are visible with both methods. Fig. 5.23 (c) shows the SFOM-MSE map of the whole bar device, and how the edge signal extends throughout the whole device.

To summarize, we introduced a tabletop technique to image the changes in the magnetic order due to the application of electrical current pulses. The exploitation of the thermoelectric effect MSE is compatible with far and near-field optical setups offering different ranges in resolution. With it, an in-plane radially symmetric induced thermal gradient allows us to map the position of domain walls within the sample. We observe changes correlated with polarity-dependent switching, as well as correlations with variations in the electrical resistance. Additionally, as a byproduct, we observed the fragmentation of the magnetic order into submicron-sized domains and its subsequent relaxation toward the original state before the pulse.

5.4 Imaging domains on the ncAFM Mn_3Sn

Lastly, we will show the detection of the order parameter in the noncollinear antiferromagnetic Mn_3Sn. This system, in contrast to CuMnAs, does not have a $\mathcal{PT}$ symmetry. Thus a net Berry curvature might be present and with it, an anomalous Hall and anomalous Nernst responses might be finite. With different symmetries, we can exploit different magneto-transport effects to obtain insight into the magnetic order. Namely, we will take advantage of the ANE response to infer the local magnetic structure.

To image the magnetic order of a Mn_3Sn sample, we use the same setup SFOM described above. A laser is focused on the sample's surface, generating an out-of-plane thermal gradient and consequently a thermal voltage due to the ANE. The thermal voltage is then recorded while scanning the laser's spot over the sample.

A key difference to the imaging in the CuMnAs is that with the MSE we are sensitive to the domain walls due to an in-plane thermal gradient. Now, for the Mn_3Sn, the thermal maps yield information from the magnetic domains stemming from the ANE and an out-of-plane thermal gradient. This highlights the versatility of the SFOM setup which allows us to exploit different thermoelectric effects depending on the material and its symmetries.

The 50 nm thick Mn_3Sn films were grown on a MgO (111) substrate with a thin Ru buffer layer of 5 nm. The films were grown along the [001] direction and were patterned into 5 μm wide Hall bars. The devices are placed inside an optical cryostat with access to a magnetic field along the perpendicular direction to the Hall bar. A micrograph of the device with the measurement scheme is shown in Fig. 5.24 (c).

As before, the SFOM setup comprises an 800 nm continuous wave laser focused on a $\approx 1\mu$m, with an intensity of 10 mW. The laser beam is modulated by an optical chopper at 1.7 kHz and the thermal voltage along the main channel of the Hall bar is measured by a lock-in amplifier at the modulation frequency.

Due to the measurement geometry, that is, an out-of-plane thermal gradient and thermal voltage measured along the y-axis, we can only resolve the x projection of the order parameter. An external field along the x-axis is used to polarize the magnetic structure between the two states that allow a finite Berry curvature along the field direction. The order parameter here denoted by the vector g is determined by the noncollinear structure and its symmetries. As discussed in section 4.3 and highlighted in Fig. 4.8 , the vector g will be perpendicular to the mirror symmetry within the system. The Fig. 5.24 (a) depicts both of the magnetic states with opposite g, set by opposite external fields. The thermal voltage due to ANE is proportional to $V_{ANE} \propto g \times \Delta T$, and when scanned over the sample it yields a map of the distribution of magnetic domains with $\pm g$ as shown in Fig. 5.24 (b) and (d).

We start by performing thermal scans at room temperature while sweeping the external field between ± 0.5 T. Fig. 5.25 (a) and (b) are very similar indicating a higher coercivity field than 0.5 T at 300 K. Yet, once the sample is warmed up to 400 K, the ± 0.5 T is enough to write uniform and opposite domains as shown in Fig. 5.25 (c) and (d). Note that the Néel temperature T_N is around 420 K.

In Fig. 5.25 (e), the average thermal signal is averaged and plotted against the external field at 400 K. We observe a clear hysteresis curve, with saturation,

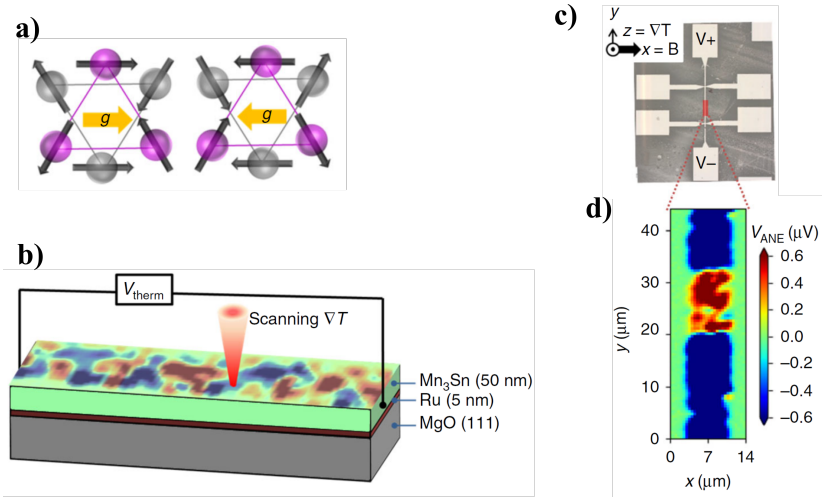

Figure 5.24: SFOM-ANE in Mn_3Sn. **a)** Magnetic domains with opposite g vector. **b)** Schematics of the SFOM-ANE and sample description. **c)** Microscope image of the Hall bar device and definition of the frame of reference. **d)** Example of a SFOM-MSE map where a red domain was prepared via heat-assisted writing. Adapted from [125].

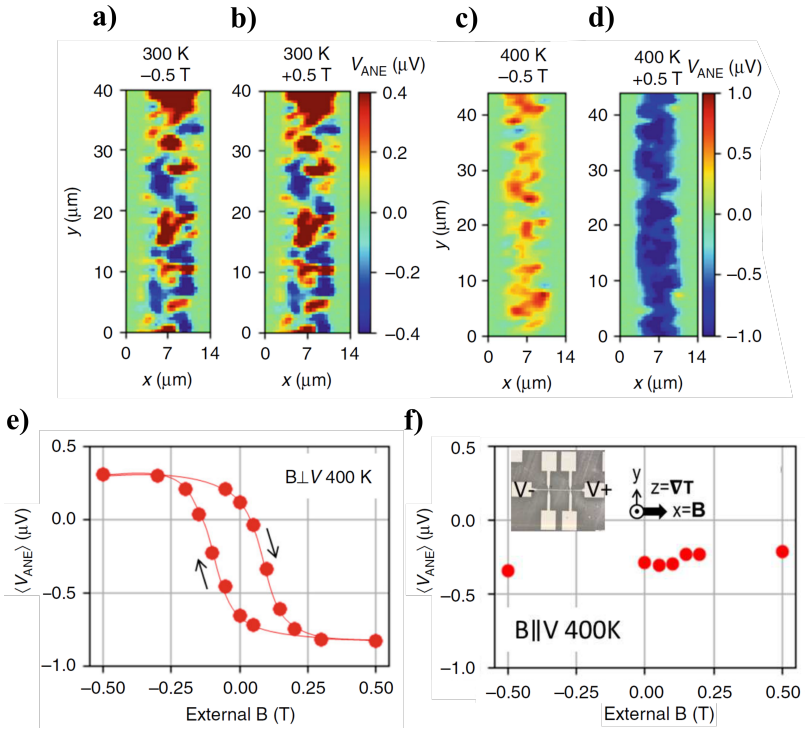

Figure 5.25: Magnetic field dependence of SFOM-ANE in Mn_3Sn. **a)** and **b)** SFOM-ANE maps at 300 K for ±0.5 T. **c)** and **d)** same at 400 K. **e)** and **f)** Average value of the thermal voltage across the device as a function of the external field for thermal voltage perpendicular and parallel to the field, respectively. Both at 400 K. Adapted from [125].

remanence and coercivity. However, if the thermal voltage is measured parallel to the applied field, no hysteresis is observed in Fig. 5.25 (f), following the ANE symmetry. This is then consistent with the measured signal coming from the ANE.

Additional support that the generated thermal signal stems from the ANE in the ncAFM, the temperature dependence of the thermal voltage response is compared to the reported ANE response from bulk Mn_3Sn crystals [69]. Multiple scans are carried out from 17 K up to 430 K, at zero field Fig. 5.26 (a-d). The Fig. 5.26 (e) shows a good agreement between the measured signal and the reported data, exhibiting a maximum signal at 150 K. Above the T_N, the ANE response vanishes as depicted in the inset of Fig. 5.26 (e).

Besides imaging the magnetic domains, a combination of the laser's power and external field allows us to manipulate the order parameter in a desired region. While imaging at 300 K with a 10 mW power, no changes in the magnetic order are observed (Fig. 5.25). However, if the laser's power is increased to 50 mW when applying ± 0.5 T, then the area under the beam's spot becomes susceptible and reorients itself according to the field's direction. Using this approach we can prepare a magnetic configuration at will, by "drawing" with the higher-power beam over the sample's surface. This heat-assisted writing is shown in Fig. 5.27 . First, we begin by resetting the whole area of interest by scanning it at 50 mW while a 0.5 T is applied. Fig. 5.27 (a) shows the mapping at 10 mW and zero field, after the writing step. Subsequently, the area enclosed by the dashed lines is scanned at 50 mW with the opposite field, followed by an entire scan at 10 mW Fig. 5.27 (b). Only the area exposed to the 50 mW beam flipped its magnetic order. The process is repeated for multiple steps of "writing" and "erasing" a red domain. Note how, the top and bottom parts of the imaged area remain as a blue domain, unaffected by the consecutive application of ± 0.5 T fields.

A closing remark on the thermal imaging techniques based on SFOM is that they do not provide a direct evaluation of the induced thermal gradient. And consequently, quantifying the thermoelectric effects is not easy, often requiring indirect methods such as simulations.

Here, we demonstrated that the magnetic order of the ncAFM Mn_3Sn can be spatially resolved, using a combination of the scanning far-field optical microscopy and the ANE present in Mn_3Sn. We showed that by warming up the sample close to its Néel temperature, an external field can be used to obtain a uniform domain distribution. The measured thermal voltage in our thin films follows the same temperature dependence as the ANE observed in bulk systems. And finally, we show that we can prepare domain patterns at will. It opens the possibility to further study other phenomena in similar systems. For instance, it allows for the preparation of magnetic domains differently oriented and study STT-induced domain wall motion [126].

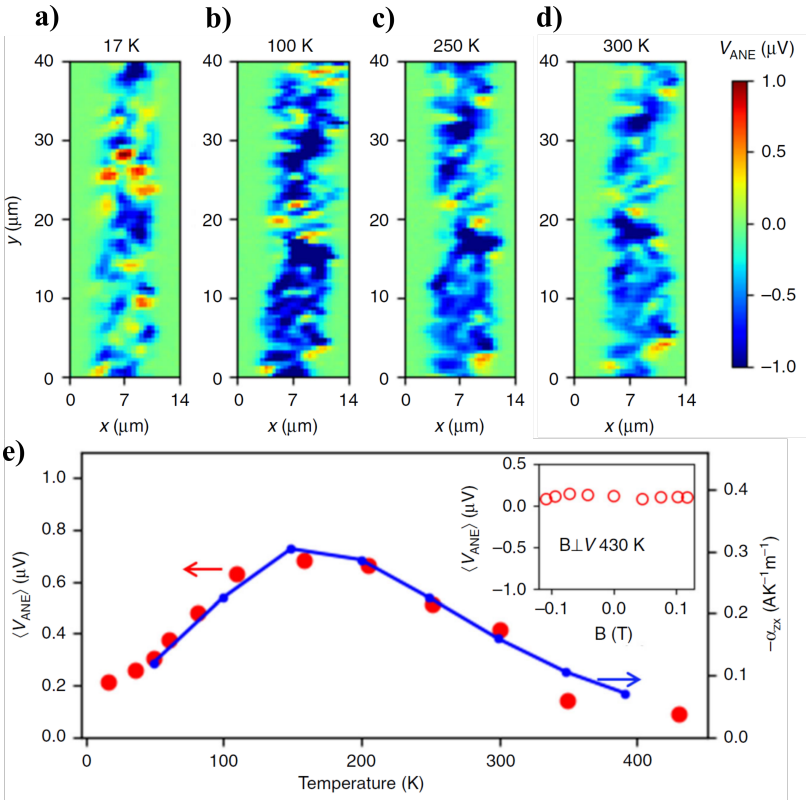

Figure 5.26: Temperature dependence of the ANE in Mn_3Sn. **a) - d)** SFOM-ANE maps at 17 K, 100 K, 250 K and 300 K. **e)** Average thermal signal (red circles) as a function of the temperature. The measured signal in our thin films exhibits a similar trend with the ANE observed for bulk systems in [69]. Adapted from [125].

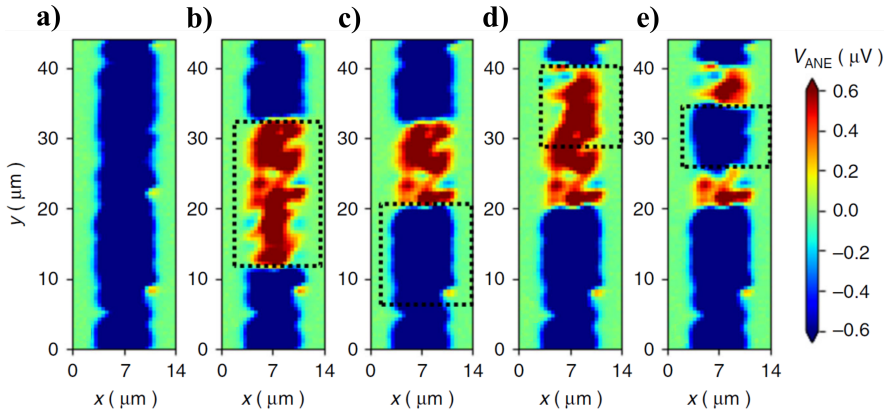

Figure 5.27: Heat-assisted domain writing in Mn_3Sn. **a)** Sample prepared into a single magnetic domain, by combining a 50 mW laser's power and 0.5 T field. **b) - e)** Sequence of writing and erasing a red domain. The red domain corresponds to the domain favored by −0.5 T. The dashed square encircles the area exposed to the 50 mW laser. All maps were obtained at 300 K and using 10 mW. Adapted from [125].

6. Outlook

Based on the experience acquired throughout this work, in this chapter, we discuss and propose possible future directions stemming from our results. We begin by introducing a possible future project on synthetic antiferromagnets, and after we revisit the thermal imaging done on CuMnAs with a possible additional contribution to our overall signal or an alternative explanation altogether.

6.1 AFM Spin-orbit Oscillators

Throughout this work, we took advantage of current-induced effective fields in order to electrically switch antiferromagnetic systems. Additionally, in our 2$^{\text{nd}}$ harmonic detection, we make use of the effective fields to periodically tilt the Néel vector and hence generate the nonlinear magnetoresistance response. We did not, however, explore the possibility to induce stable oscillations, that is, auto-oscillation of the magnetic order.

Auto-oscillation refers to the periodic motion of a system due to a power source that lacks any corresponding periodicity. An auto-oscillatory system comprises three main components, a resonant element that determines the frequency of the oscillations, a dissipative element and a source of energy [127]. The dissipative or damping element is inevitable in any real system where the system can dissipate energy via multiple mechanisms. The source element may be regarded as "negative damping" and in the dynamical equations of motion takes the same form as the damping term but with the opposite sign.

This phenomenon can be observed in magnetic systems, where a stable precession of the magnetic moment is induced by a DC current. The devices used to explore the magnetic auto-oscillations are categorized as spin-torque nano-oscillators (STNO) or spin-Hall nano-oscillators (SHNO), depending on whether the spin current injected into the oscillating magnetization originates from STT or SOT [18]. Within this framework, the LLG equation can be rewritten as:

$$\frac{\mathrm{d}M}{\mathrm{d}t} = \gamma\mu_0 M \times H_{eff} + \Gamma_+ + \Gamma_- \ , \tag{6.1}$$

where $\Gamma_\pm$ are the positive and negative damping terms, i.e., the Gilbert damping term and the Slonczewski (antidamping) torque respectively. The field-like torque is omitted in this analysis.

While the Gilbert damping Γ_+ depends only on the position (or oscillation's orbit), the Slonczewski term is also a function of the current amplitude, either in STT or SOT geometries. For zero electrical current, there is no negative damping $\Gamma_- = 0$ and we have a static solution with the moment aligned along H_{eff}. As the current's amplitude increases, the threshold for auto-oscillation is met. This threshold happens when the magnitude of the negative damping equals the positive damping $\Gamma_- = \Gamma_+$. This condition also defines the electrical current threshold to generate auto-oscillations. Above the threshold current, the oscillation orbit is determined such that the two damping terms remain equal, in order to create a stable limit cycle in the phase space. In other words, to reach

a stable auto-oscillation regime the energy losses should be compensated by the total energy supplied to the system.

The oscillation's frequency depends on the current's amplitude, even though the frequency is given by the conservative precession term which is not explicitly a function of the current, besides the Oersted field. The main reason for it is due to the demagnetizing field. With an increasing precession cone, the contribution of the demagnetizing field to the total effective field H_{eff} changes and thus the frequency changes as well. A second possible source of current-depend frequency is Joule heating and the consequently slight changes in the system parameters, as anisotropy fields.

With our comprehensive understanding of the SAF system, an interesting suggestion to consider would be the exploration of a SAF-based SHNO. Similar multilayer structures have been explored in STNO geometries, that is, where a robust FM layer polarizes the electrical current that is injected into the free FM layer. The spin current acts as the negative damping, resulting in a precession of the free FM layer. Note that in these spin-valve-like devices, the electrical current flows perpendicularly to the stack and *only* one FM layer has a dynamical motion, while the second layer remains static.

The proposed goal is to create a SOT-driven oscillator with both FM layers in motion, where the interlayer-exchange interaction plays a crucial role. Not only, we could take advantage of the exchange-enhanced dynamics of the antiferromagnetic system, but by exploring the current dependency of the angle between the two antiferromagnetically-coupled moments we can tune the oscillation's frequency.

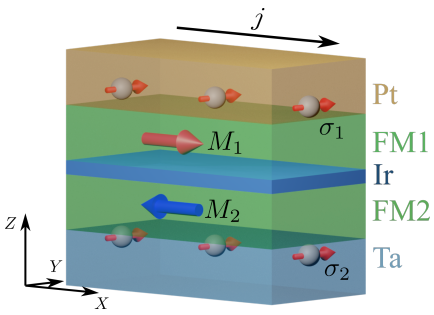

Figure 6.1: Proposed SAF system to observe current-induced auto-oscillations.

Macrospin simulations were performed to investigate the potential of a SAF-based SHNO, showing promising preliminary results. Similar structures to our out-of-plane SAF samples are considered, where the SAF is sandwiched between two heavy metal layers. Two key differences to the out-of-plane SAF samples are, 1) we consider now an in-plane system and 2) instead of two Pt layers we consider two heavy metals with opposite Hall angles. The proposed system is illustrated in Fig. 6.1 , where the chosen heavy metals are Pt and Ta. The system's dynamics are modeled using a set of two coupled LLG equations, which describe the behavior of two identical FM layers. We considered an external field H, an in-plane magnetic anisotropy H_u and interlayer exchange H_{ex}. The parameters used were the following: $\alpha = 0.01$, $H = 0.9$ T, $H_u = -0.1$ T and $H_{ex} = 0.5$ T. With these constants, the spin-flip field is at 1 T.

The Fig. 6.2 (a) shows preliminary results. In it, we observe stable auto-

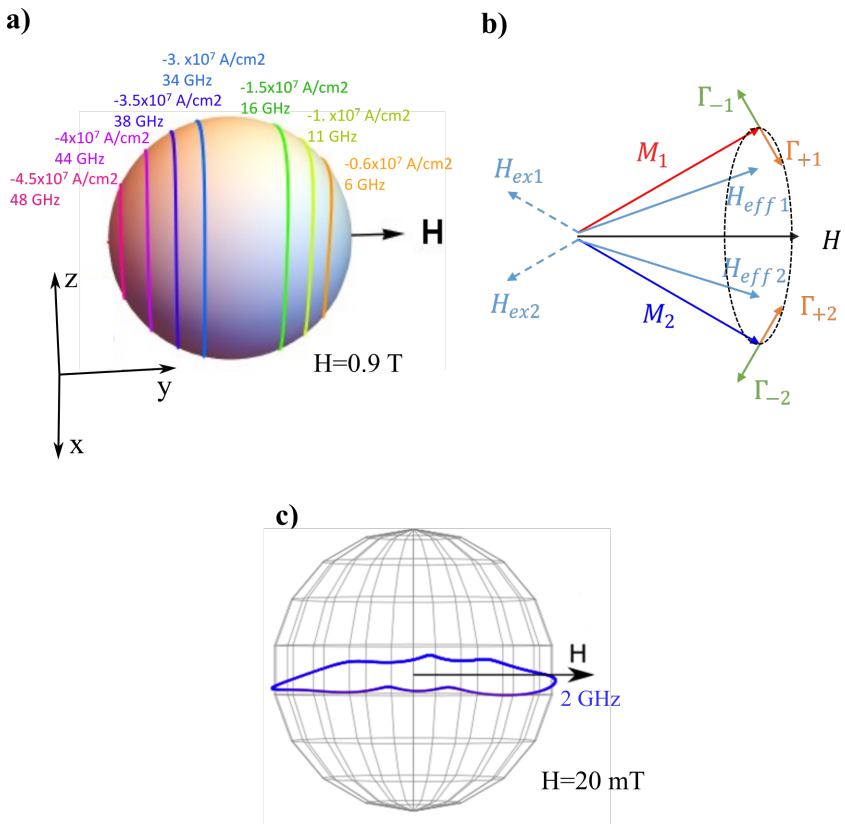

Figure 6.2: Macrospin simulation on a SAF-based spin Hall nano-oscillator. **a)** Stable auto-oscillation orbits for different current magnitudes at $H = 0.9$ T. The electrical current flows along the x-axis and the external field is applied along the y-axis. **b)** Illustration of the fields and torques during the auto-oscillation. **c)** Stable auto-oscillation orbit at $j = 2 \times 10^7$ A/cm^2 and $H = 20$ mT.

oscillations with an electrical current applied along the x-axis and the external field along the y-axis. The oscillation's orbit of both moments defines a cone around the applied field, where both moments are out-of-phase. This might be puzzling at why the moments precess around the applied field and not around their own effective field. However, due to the exchange field, the respective effective fields, H_{eff1} and H_{eff2}, are also periodically oscillating.

The Fig. 6.2 (b) shows a snapshot of the auto-oscillation with a schematic of the fields at play and both damping torques (Γ_+ and Γ_-). For small angles, the exchange field H_{ex} has an antiparallel component to the applied field, and therefore it reduces the total effective field H_{eff}. With a weaker effective field, the oscillation precession is slower. However, with an increasing current density, the orbit's cone opens and consequently the frequency increases. This is the exchange-spring effect. That is, higher current densities stabilize larger orbit cones which leads to the exchange field aligning and adding up to the external field. The gradual addition of the exchange to the external field results in stronger effective fields, and thus, faster dynamics. This exchange-spring effect could be an interesting mechanism for a SHNO with a tunable wide-range frequency.

Instead of requiring an applied field close to the spin-flip field, it would be interesting to investigate auto-oscillation regimes at low applied fields when the AFM order is mostly unperturbed. Fig. 6.2 (c) shows a stable orbit at $H = 20$

mT. In this case, the trajectory of both magnetizations lies mostly in the plane with small time-varying tilting in out-of-plane direction.

These findings provide valuable initial insights into a SAF-based SNHO. However, it should be noted that the macrospin model used in this study has limitations. Specifically, it lacks important contributions such as the demagnetizing field and the shape anisotropy of a realistic device. For instance, in the high-field regime, both of these fields would most likely restrict how wide the precession cone can open and it would also cause a deformation of the circular orbits into elliptic ones. Despite these limitations, the results of this study motivate further exploration of synthetic antiferromagnetic systems in the field of spin torque oscillators.

In future research, it would be relevant to conduct more complex simulations, such as micromagnetic simulations, that take into account these missing contributions. We see indications of auto-oscillations at low and high applied fields, comparatively to the spin-flip field. Simultaneously, the experimental observation would be valuable. The auto-oscillation dynamics are commonly detected electrically with a spectrum analyzer or optically via Brillouin light scattering spectroscopy. Such experiments could provide insights into the possibility of AFM oscillators and serve as a model system to test already existing theoretical work, including the possibility of chaotic auto-oscillation regimes [128].

6.2 Photocurrents in Mn_2Au

In this section, we will review our findings on the scanning thermal imaging of CuMnAs and contextualize them in light of recent findings published by Merte et al. on Arxiv [129]. In their work, they use first-principles methods to study the emergence of charge and spin photocurrents in Mn_2Au. We will briefly describe their findings focusing on the charge photocurrents.

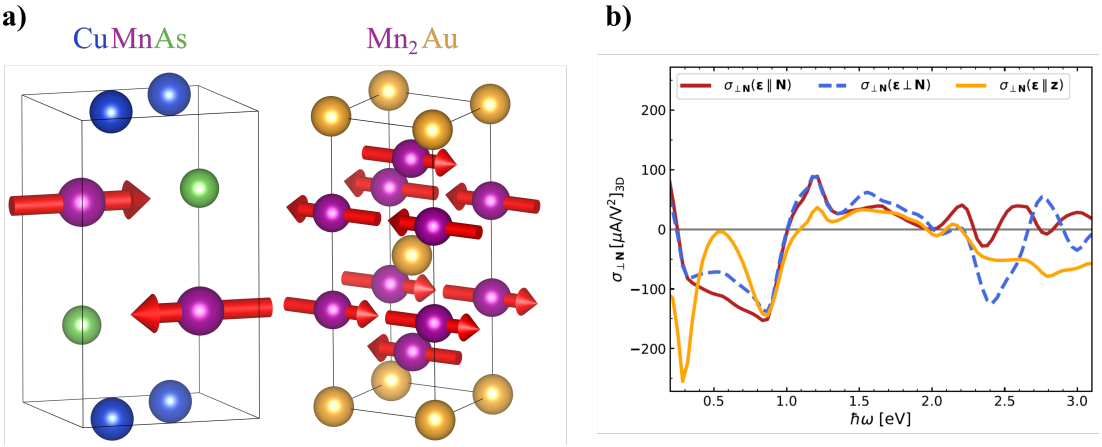

Figure 6.3: Photocurrent in Mn_2Au. **a)** Crystal structures of CuMnAs and Mn_2Au. The crystal structure of CuMnAs is shifted so that the inversion center of the nonmagnetic crystal is in the unit cell center. **b)** Frequency dependence of the conductivity tensor for the electric field polarized along three different axes, adapted from [129]. $\sigma_\perp$ corresponds to the conductivity perpendicular to the Néel vector, and ϵ the electric field polarization.

They investigated the second-order charge current induced by an electric field of a continuous laser. As we discussed in the previous chapter, second-order effects require a broken inversion symmetry. In Mn_2Au, the $\mathcal{P}$ symmetry is broken by the staggered magnetic moments as seen in Fig. 6.3 (a). Therefore, the photocurrents are expected to be of purely magnetic origin and to be dependent on the orientation of the Néel vector. From this point of view, we would like to already question whether the study done by Merte et al. can not be extended to the CuMnAs. From a symmetry perspective they are similar. Also in CuMnAs, the $\mathcal{P}$ symmetry of the crystal is broken by the magnetic sublattices. In Fig. 6.3 (a), the crystal structure of CuMnAs is shifted so that the inversion center of the nonmagnetic crystal is in the unit cell center.

They found that the photocurrent flowing perpendicularly to the Néel vector is larger than the photocurrent flowing parallel to it. Moreover, the perpendicular current is maximized for linearly polarized light, while the parallel response is only driven by circularly polarized light. Regarding the symmetry of the generated photocurrent, it follows that:

$$J_y(N \parallel x; \epsilon \parallel y) = -J_x(N \parallel y; \epsilon \parallel x) \tag{6.2}$$

$$J_y(N \parallel x; \epsilon \parallel x) = -J_x(N \parallel y; \epsilon \parallel y) \ , \tag{6.3}$$

with J_x and J_y the photocurrents along x and y axes, N the Néel vector and ϵ the light's polarization.

Besides the polarization dependence, this second-order optical effect also depends on the light's wavelength as shown in Fig. 6.3 (b). Not only the magnitude, but the signal's sign also changes with the color of the laser.

We have already brought up the question, what about the same nonlinear effect in CuMnAs? We expect it to be equally possible while being difficult to predict the amplitude of such effects. If so, is it present in our scanning thermal imaging signals? Could it be an additional contribution or an alternative interpretation of the generated signal altogether? In our interpretation, the incident beam shines on the sample warming it up, and thereby generating a temperature gradient. The thermal gradient, in turn, induces the thermoelectric signal. On the other hand, in the predicted second-order optical effect it is the electric field on the incident beam that drives the photocurrent. Both of our setups, SFOM and SNOM, can induce both effects, the thermal and the nonlinear. To identify the respective contributions to the overall measured signal, as highlighted in the Fig. 6.3 (b), we can exploit the wavelength and polarization dependences. In hindsight, these dependences might have been overlooked since these should not significantly affect the generation of the temperature gradient. In this regard, the wavelength dependence might provide a useful tool to disentangle the two contributions. For the Mn_2Au case, depending on the wavelength the nonlinear signal can change sign. In contrast to the thermal signal which is not expect to flip sign.

One particularity of the results of Merte et al. is a photocurrent driven by a z-polarized electric field. In an optical setup where the beam has a normal incidence to the sample, it is not possible in the far-field regime. It would mean an electric field along the Poynting vector. However, an electric field perpendicularly polarized to the sample's interface is possible in the SNOM setup. Fig. 6.4 illustrates the difference between SFOM and SNOM regarding the electric field's

polarization ϵ. In the far-field microscopy, the polarization is either along the x-axis or y-axis as shown in Fig. 6.4 (a). Or alternatively, a combination of the two resulting in the circularly polarized light. In the SNOM setup, when an incident beam is focused on the AFM tip, it induces a point dipole at its apex. Consequently, the tip emits a near-field electric field which is along the sample's normal, as depicted in Fig. 6.4 (b). The nonlinear photocurrent can then be expected to be present in both microscopies, far and near-field, exploiting either the in-plane or the out-of-plane polarizations.

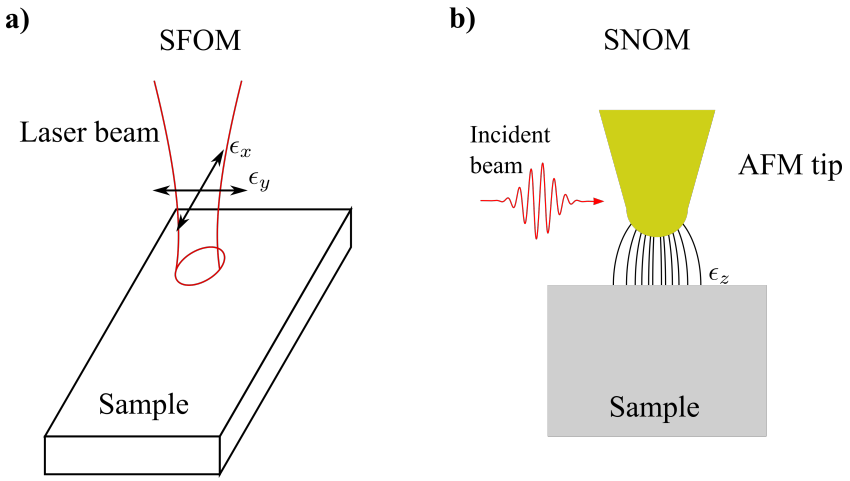

Figure 6.4: Electric field polarization in SFOM and SNOM. **a)** SFOM setup with in-plane polarization ϵ_x and ϵ_y. **b)** SNOM setup where an incident beam on the tip of an AFM induces a point dipole at the tip's apex, generating an electric field towards the sample with z polarization ϵ_z.

The nonlinear signal predicted in their work stems from the magnetic domains, in contrast to the magneto-Seebeck effect which senses the domain walls. Thus, the nonlinear photocurrent could explain one puzzling observation from our MSE maps, why some of the features extend for longer regions than the expected domain-wall width.

These promising new findings justify further investigation and experimental confirmation. It could provide a new mechanism to map the Néel order in cAFM with the inversion symmetry broken by the magnetic order. Secondly, it does not rely on stabilizing a temperature gradient and thus it allows for a faster detection method. Simultaneously, revisiting our results on the thermal imaging of CuMnAs would be worthwhile as they might already contain a first hint of nonlinear photocurrents.

7. Conclusion

The fundamental question behind this Ph.D. work was: How to detect the magnetic order in antiferromagnets, and more specifically, how to electrically identify the Néel vector reversal in $\mathcal{PT}$ symmetric systems. Special attention was dedicated to the tetragonal antiferromagnetic CuMnAs. This system sparked interest in the spintronics field, after the initial prediction and later demonstration of magnetic reorientation via Néel spin-orbit torque. An important milestone toward an AFM-based spintronics device. While the AMR offered a way to detect a 90° rotation of the order parameter, the distinction between reversed states remained elusive.

We started by considering a model system for the CuMnAs, a multilayered system comprising an out-of-plane SAF with two adjacent Pt layers. When electrical current flows through, due to the Pt layers a staggered spin accumulation develops at the interfaces. Such spin accumulation will in turn interact with the local magnetization of the neighboring ferromagnetic layer. We take advantage of this current-induced manipulation of the moments to, not only switch the magnetic state by reversing the Néel vector but to slightly tilt the moments out of their equilibrium positions. The small displacement from the equilibrium position results in an additional current-dependent term to the measured magnetoresistance - the second-order magnetotransport coefficient.

We make use of a homodyne detection technique to probe the second-order response of the magnetoresistance. We showed that when applying an AC current through a device, the higher-order term is contained in a signal oscillating at double the excitation frequency. Thus, the technique is also called 2^{nd} harmonic detection. Measuring the 2^{nd} harmonic signal after reversing the Néel vector via an external field, and comparing it to the domain distribution imaged in MFM, we build evidence that this signal can probe the reversal of the magnetic order. Moreover, without the requirement of a net magnetic moment, not allowed in $\mathcal{PT}$ symmetric systems. As a model system for collinear antiferromagnets, the SAF allows us to more intuitively grasp the mechanisms at play and develop an electrical method to differentiate oppositely oriented antiferromagnetic domains. With these tools, we moved to the CuMnAs thin films.

The knowledge acquired for the SAF system carries over and is equally applicable to the CuMnAs. We showed that the 2^{nd} harmonic signal can probe resistance variations in a current polarity-dependent switching, that is not detected by the resistance's linear term. The CuMnAs allows the presence of the Néel spin-orbit torque. Thanks to it, there is no need for adjacent heavy metal layers in order to act on the magnetic moments. Another key advantage of the CuMnAs is the possibility of field-free writing and reading of the magnetic order, in contrast to the out-of-plane SAF.

In both systems, the nonlinear response exhibits long stability, paving a way for antiferromagnetic memory devices. In addition to it, in the SAF we observe a multilevel switching that shows a memristive behavior, potentially interesting for neuromorphic applications.

Along with the electric detection of the magnetic order, we also explored imaging via thermoelectric effects. We showed how the thermoelectric maps change

in a reproducible way with the application of electrical current pulses, and that these changes are correlated with variations in electrical resistance. The thermal signal arises from the magneto-Seebeck effect, which yields a net voltage when the thermal gradient is generated in a region with a varying magnetic texture. The magneto-Seebeck maps are consequently sensitive to domain walls rather than the domains themselves.

The thermal imaging was obtained via two different methods, first using far-field and later near-field optical microscopy. While using far-field light, the resolution of our scans is around 1 μm. However, the not diffraction-limited near-field microscopy reaches resolutions of tens of nm. The SFOM was used to investigate current polarity switching on biaxial CuMnAs samples. In addition, the shattering of the magnetic order into fragmented submicron-sized domains and their subsequent relaxation was observed in SFOM. CuMnAs samples exhibiting a uniaxial anisotropy were imaged using SNOM, where we observed the reproducible back-and-forth motion of a 180° domain wall.

Lastly, using the same SFOM setup, we thermally wrote and imaged magnetic domains in the noncollinear antiferromagnet Mn_3Sn. We started by showing the thermal response is compatible with originating from the anomalous Nernst effect. We further showed that by combining a laser beam with higher power and an external field, we can define a magnetic pattern at will.

Bibliography

[1] J. Železný, H. Gao, K. Výborný, J. Zemen, J. Mašek, Aurélien Manchon, J. Wunderlich, Jairo Sinova, and T. Jungwirth. Relativistic Néel-Order Fields Induced by Electrical Current in Antiferromagnets. *Physical Review Letters*, 113(15):157201, oct 2014.

[2] P. Wadley, B. Howells, J. Železný, C. Andrews, V. Hills, R. P. Campion, V. Novák, K. Olejník, F. Maccherozzi, S. S. Dhesi, S. Y. Martin, T. Wagner, J. Wunderlich, F. Freimuth, Y. Mokrousov, J. Kuneš, J. S. Chauhan, M. J. Grzybowski, A. W. Rushforth, Kw Edmond, B. L. Gallagher, and T. Jungwirth. Spintronics: Electrical switching of an antiferromagnet. *Science*, 351(6273):587–590, 2016.

[3] S. Yu. Bodnar, L. Šmejkal, I. Turek, T. Jungwirth, O. Gomonay, J. Sinova, A. A. Sapozhnik, H.-J. Elmers, M. Kläui, and M. Jourdan. Writing and reading antiferromagnetic Mn2Au by Néel spin-orbit torques and large anisotropic magnetoresistance. *Nature Communications*, 9(1):348, 2018.

[4] W. H. Meiklejohn and C. P. Bean. New Magnetic Anisotropy. *Phys. Rev.*, 105(3):904–913, feb 1957.

[5] I. Dzyaloshinsky. A thermodynamic theory of "weak" ferromagnetism of antiferromagnetics. *Journal of Physics and Chemistry of Solids*, 4(4):241–255, 1958.

[6] Tôru Moriya. Anisotropic superexchange interaction and weak ferromagnetism. *Physical Review*, 120(1):91–98, oct 1960.

[7] Börge Göbel, Ingrid Mertig, and Oleg A. Tretiakov. Beyond skyrmions: Review and perspectives of alternative magnetic quasiparticles. *Physics Reports*, 895:1–28, 2021.

[8] L. Berger. Emission of spin waves by a magnetic multilayer traversed by a current. *Phys. Rev. B*, 54(13):9353–9358, oct 1996.

[9] J. C. Slonczewski. Current-driven excitation of magnetic multilayers. *Journal of Magnetism and Magnetic Materials*, 159(1-2):L1–L7, 1996.

[10] J. C. Slonczewski. Excitation of spin waves by an electric current. *Journal of Magnetism and Magnetic Materials*, 195(2):L261–L268, 1999.

[11] M. Tsoi, A. G. M. Jansen, J. Bass, W. C. Chiang, M. Seck, V. Tsoi, and P. Wyder. Excitation of a magnetic multilayer by an electric current. *Physical Review Letters*, 80(19):4281–4284, may 1998.

[12] E. B. Myers, D. C. Ralph, J. A. Katine, R. N. Louie, and R. A. Buhrman. Current-induced switching of domains in magnetic multilayer devices. *Science*, 285(5429):867–870, aug 1999.

[13] J. A. Katine, F. J. Albert, R. A. Buhrman, E. B. Myers, and D. C. Ralph. Current-driven magnetization reversal and spin-wave excitations in Co/Cu/Co pillars. *Physical Review Letters*, 84(14):3149–3152, apr 2000.

[14] J. Grollier, V. Cros, A. Hamzic, J. M. George, H. Jaffrès, A. Fert, G. Faini, J. Ben Youssef, and H. Legall. Spin-polarized current induced switching in Co/Cu/Co pillars. *Applied Physics Letters*, 78(23):3663–3665, may 2001.

[15] Andrew D. Kent and Daniel C. Worledge. A new spin on magnetic memories. *Nature Nanotechnology*, 10(3):187–191, 2015.

[16] Dmytro Apalkov, Bernard Dieny, and J. M. Slaughter. Magnetoresistive Random Access Memory: Magnetoresistive random access memory (MRAM) and particularly spin-transfer-torque MRAM is a nonvolatile memory with very high endurance and scalability. It is based on an array of magnetic tunnel junctions with magn. *Proceedings of the IEEE*, 104(10):1796–1830, 2016.

[17] R. K. Dumas, S. R. Sani, S. M. Mohseni, E. Iacocca, Y. Pogoryelov, P. K. Muduli, S. Chung, P. Dürrenfeld, and J. Åkerman. Recent Advances in Nanocontact Spin-Torque Oscillators. *IEEE Transactions on Magnetics*, 50(6):1–7, 2014.

[18] T. Chen, R. K. Dumas, A. Eklund, P. K. Muduli, A. Houshang, A. A. Awad, P. Dürrenfeld, B. G. Malm, A. Rusu, and J. Åkerman. Spin-Torque and Spin-Hall Nano-Oscillators. *Proceedings of the IEEE*, 104(10):1919–1945, 2016.

[19] Mohammad Haidar, Ahmad A. Awad, Mykola Dvornik, Roman Khymyn, Afshin Houshang, and Johan Åkerman. A single layer spin-orbit torque nano-oscillator. *Nature Communications*, 10(1):2362, 2019.

[20] P. Němec, E. Rozkotová, N. Tesařová, F. Trojánek, E. De Ranieri, K. Olejník, J. Zemen, V. Novák, M. Cukr, P. Malý, and T. Jungwirth. Experimental observation of the optical spin transfer torque. *Nature Physics*, 8(5):411–415, 2012.

[21] K. Ando, S. Takahashi, J. Ieda, H. Kurebayashi, T. Trypiniotis, C. H. W. Barnes, S. Maekawa, and E. Saitoh. Electrically tunable spin injector free from the impedance mismatch problem. *Nature Materials*, 10(9):655–659, 2011.

[22] A. Manchon and S. Zhang. Theory of spin torque due to spin-orbit coupling. *Physical Review B - Condensed Matter and Materials Physics*, 79(9):94422, mar 2009.

[23] Xiufeng Han, Xiao Wang, Caihua Wan, Guoqiang Yu, and Xiaorong Lv. Spin-orbit torques: Materials, physics, and devices. *Applied Physics Letters*, 118(12):120502, mar 2021.

[24] A. Manchon, J. Železný, I. M. Miron, T. Jungwirth, J. Sinova, A. Thiaville, K. Garello, and P. Gambardella. Current-induced spin-orbit torques in ferromagnetic and antiferromagnetic systems. *Reviews of Modern Physics*, 91(3):35004, sep 2019.

[25] G. Dresselhaus. Spin-orbit coupling effects in zinc blende structures. *Physical Review*, 100(2):580–586, oct 1955.

[26] E. I. Rashba. Properties of semiconductors with an extremum loop I. Cyclotron and combinational resonance in amagnetic field perpendicular to the plane of the loop. *Sov. Phys. Solid State*, 2:1109–1122, 1960.

[27] Yu A. Bychkov and E. I. Rashba. Oscillatory effects and the magnetic susceptibility of carriers in inversion layers. *Journal of Physics C: Solid State Physics*, 17(33):6039–6045, 1984.

[28] Ioan Mihai Miron, Gilles Gaudin, Stéphane Auffret, Bernard Rodmacq, Alain Schuhl, Stefania Pizzini, Jan Vogel, and Pietro Gambardella. Current-driven spin torque induced by the Rashba effect in a ferromagnetic metal layer. *Nature Materials*, 9(3):230–234, 2010.

[29] Luqiao Liu, Chi-Feng Pai, Y. Li, H. W. Tseng, D. C. Ralph, and R. A. Buhrman. Spin-Torque Switching with the Giant Spin Hall Effect of Tantalum. *Science*, 336(6081):555–558, may 2012.

[30] V. M. Edelstein. Spin polarization of conduction electrons induced by electric current in two-dimensional asymmetric electron systems. *Solid State Communications*, 73(3):233–235, 1990.

[31] S. D. Ganichev, E. L. Ivchenko, V. V. Bel'kov, S. A. Tarasenko, M. Sollinger, D. Weiss, W. Wegscheider, and W. Prettl. Spin-galvanic effect. *Nature*, 417(6885):153–156, may 2002.

[32] A. W. Rushforth, K. Výborný, C. S. King, K. W. Edmonds, R. P. Campion, C. T. Foxon, J. Wunderlich, A. C. Irvine, V. Novák, K. Olejník, A. A. Kovalev, Jairo Sinova, T. Jungwirth, and B. L. Gallagher. The origin and control of the sources of AMR in (Ga,Mn)As devices. *Journal of Magnetism and Magnetic Materials*, 321(8):1001–1008, 2009.

[33] T. McGuire and R. Potter. Anisotropic magnetoresistance in ferromagnetic 3d alloys. *IEEE Transactions on Magnetics*, 11(4):1018–1038, 1975.

[34] Philipp Ritzinger and Karel Vyborny. Anisotropic magnetoresistance: materials, models and applications, 2022.

[35] I. Fina, X. Marti, D. Yi, J. Liu, J. H. Chu, C. Rayan-Serrao, S. Suresha, A. B. Shick, J. Železný, T. Jungwirth, J. Fontcuberta, and R. Ramesh. Anisotropic magnetoresistance in an antiferromagnetic semiconductor. *Nature Communications*, 5(1):4671, 2014.

[36] X. Marti, I. Fina, C. Frontera, Jian Liu, P. Wadley, Q. He, R. J. Paull, J. D. Clarkson, J. Kudrnovský, I. Turek, J. Kuneš, D. Yi, J.-H. Chu, C. T. Nelson, L. You, E. Arenholz, S. Salahuddin, J. Fontcuberta, T. Jungwirth, and R. Ramesh. Room-temperature antiferromagnetic memory resistor. *Nature Materials*, 13(4):367–374, 2014.

[37] D. Kriegner, H. Reichlova, J. Grenzer, W. Schmidt, E. Ressouche, J. Godinho, T. Wagner, S. Y. Martin, A. B. Shick, V. V. Volobuev, G. Springholz, V. Holý, J. Wunderlich, T. Jungwirth, and K. Výborný. Magnetic anisotropy in antiferromagnetic hexagonal MnTe. *Physical Review B*, 96(21):214418, dec 2017.

[38] M. N. Baibich, J. M. Broto, A. Fert, F. Nguyen Van Dau, F. Petroff, P. Etienne, G. Creuzet, A. Friederich, and J. Chazelas. Giant Magnetoresistance of (001)Fe/(001)Cr Magnetic Superlattices. *Physical Review Letters*, 61(21):2472–2475, nov 1988.

[39] G. Binasch, P. Grünberg, F. Saurenbach, and W. Zinn. Enhanced magnetoresistance in layered magnetic structures with antiferromagnetic interlayer exchange. *Physical Review B*, 39(7):4828–4830, mar 1989.

[40] J. Barnaś, A. Fuss, R. E. Camley, P. Grünberg, and W. Zinn. Novel magnetoresistance effect in layered magnetic structures: Theory and experiment. *Physical Review B*, 42(13):8110–8120, nov 1990.

[41] C. H. Marrows, Nathan Wiser, B. J. Hickey, T. P. A. Hase, and B. K. Tanner. Giant magnetoresistance and oscillatory exchange coupling in disordered Co/Cu multilayers. *Journal of Physics: Condensed Matter*, 11(1):81, 1999.

[42] S. Ikeda, J. Hayakawa, Y. Ashizawa, Y. M. Lee, K. Miura, H. Hasegawa, M. Tsunoda, F. Matsukura, and H. Ohno. Tunnel magnetoresistance of 604diffusion in CoFeB/MgO/CoFeB pseudo-spin-valves annealed at high temperature. *Applied Physics Letters*, 93(8):82508, aug 2008.

[43] E. H. Hall. On a New Action of the Magnet on Electric Currents. *American Journal of Mathematics*, 2(3):287–292, feb 1879.

[44] Naoto Nagaosa, Jairo Sinova, Shigeki Onoda, A. H. MacDonald, and N. P. Ong. Anomalous Hall effect. *Reviews of Modern Physics*, 82(2):1539–1592, may 2010.

[45] N. A. Sinitsyn. Semiclassical theories of the anomalous Hall effect. *Journal of Physics: Condensed Matter*, 20(2):23201, 2008.

[46] Hua Chen, Qian Niu, and A. H. MacDonald. Anomalous Hall Effect Arising from Noncollinear Antiferromagnetism. *Physical Review Letters*, 112(1):17205, jan 2014.

[47] J. Kubler and C. Felser. Non-collinear antiferromagnets and the anomalous Hall effect. *Europhysics Letters*, 108(6):67001, 2014.

[48] Satoru Nakatsuji, Naoki Kiyohara, and Tomoya Higo. Large anomalous Hall effect in a non-collinear antiferromagnet at room temperature. *Nature*, 527(7577):212–215, 2015.

[49] Libor Šmejkal, Rafael González-Hernández, T. Jungwirth, and J. Sinova. Crystal time-reversal symmetry breaking and spontaneous Hall effect in collinear antiferromagnets. *Science Advances*, 6(23):eaaz8809, 2020.

[50] Zexin Feng, Xiaorong Zhou, Libor Šmejkal, Lei Wu, Zengwei Zhu, Huixin Guo, Rafael González-Hernández, Xiaoning Wang, Han Yan, Peixin Qin, Xin Zhang, Haojiang Wu, Hongyu Chen, Ziang Meng, Li Liu, Zhengcai Xia, Jairo Sinova, Tomáš Jungwirth, and Zhiqi Liu. An anomalous Hall effect in altermagnetic ruthenium dioxide. *Nature Electronics*, 5(11):735–743, 2022.

[51] Robert Karplus and J. M. Luttinger. Hall Effect in Ferromagnetics. *Physical Review*, 95(5):1154–1160, sep 1954.

[52] T. Jungwirth, Qian Niu, and A. H. MacDonald. Anomalous Hall Effect in Ferromagnetic Semiconductors. *Physical Review Letters*, 88(20):207208, may 2002.

[53] Zhong Fang, Naoto Nagaosa, Kei S. Takahashi, Atsushi Asamitsu, Roland Mathieu, Takeshi Ogasawara, Hiroyuki Yamada, Masashi Kawasaki, Yoshinori Tokura, and Kiyoyuki Terakura. The Anomalous Hall Effect and Magnetic Monopoles in Momentum Space. *Science*, 302(5642):92–95, oct 2003.

[54] Taishi Chen, Takahiro Tomita, Susumu Minami, Mingxuan Fu, Takashi Koretsune, Motoharu Kitatani, Ikhlas Muhammad, Daisuke Nishio-Hamane, Rieko Ishii, Fumiyuki Ishii, Ryotaro Arita, and Satoru Nakatsuji. Anomalous transport due to Weyl fermions in the chiral antiferromagnets Mn3X, X = Sn, Ge. *Nature Communications*, 12(1):572, 2021.

[55] Naoto Nagaosa and Yoshinori Tokura. Emergent electromagnetism in solids. *Physica Scripta*, 2012(T146):14020, 2012.

[56] Shigeki Onoda and Naoto Nagaosa. Spin Chirality Fluctuations and Anomalous Hall Effect in Itinerant Ferromagnets. *Physical Review Letters*, 90(19):196602, may 2003.

[57] P. Bruno, V. K. Dugaev, and M. Taillefumier. Topological Hall Effect and Berry Phase in Magnetic Nanostructures. *Physical Review Letters*, 93(9):96806, aug 2004.

[58] A. Neubauer, C. Pfleiderer, B. Binz, A. Rosch, R. Ritz, P. G. Niklowitz, and P. Böni. Topological Hall Effect in the *A* Phase of MnSi. *Physical Review Letters*, 102(18):186602, may 2009.

[59] Christoph Sürgers, Gerda Fischer, Patrick Winkel, and Hilbert V. Löhneysen. Large topological Hall effect in the non-collinear phase of an antiferromagnet. *Nature Communications*, 5(1):3400, 2014.

[60] M. I. Dyakonov and V. I. Perel. Current-induced spin orientation of electrons in semiconductors. *Physics Letters A*, 35(6):459–460, 1971.

[61] Y. K. Kato, R. C. Myers, A. C. Gossard, and D. D. Awschalom. Observation of the Spin Hall Effect in Semiconductors. *Science*, 306(5703):1910–1913, dec 2004.

[62] J. Wunderlich, B. Kaestner, J. Sinova, and T. Jungwirth. Experimental Observation of the Spin-Hall Effect in a Two-Dimensional Spin-Orbit Coupled Semiconductor System. *Physical Review Letters*, 94(4):47204, feb 2005.

[63] Shuichi Murakami, Naoto Nagaosa, and Shou-Cheng Zhang. Dissipationless Quantum Spin Current at Room Temperature. *Science*, 301(5638):1348–1351, sep 2003.

[64] Jairo Sinova, Dimitrie Culcer, Q. Niu, N. A. Sinitsyn, T. Jungwirth, and A. H. MacDonald. Universal Intrinsic Spin Hall Effect. *Physical Review Letters*, 92(12):126603, mar 2004.

[65] E. Saitoh, M. Ueda, H. Miyajima, and G. Tatara. Conversion of spin current into charge current at room temperature: Inverse spin-Hall effect. *Applied Physics Letters*, 88(18):182509, may 2006.

[66] S. O. Valenzuela and M. Tinkham. Direct electronic measurement of the spin Hall effect. *Nature*, 442(7099):176–179, 2006.

[67] T. Kimura, Y. Otani, T. Sato, S. Takahashi, and S. Maekawa. Room-Temperature Reversible Spin Hall Effect. *Physical Review Letters*, 98(15):156601, apr 2007.

[68] Gerrit E. W. Bauer, Eiji Saitoh, and Bart J. van Wees. Spin caloritronics. *Nature Materials*, 11(5):391–399, 2012.

[69] Muhammad Ikhlas, Takahiro Tomita, Takashi Koretsune, Michi-To Suzuki, Daisuke Nishio-Hamane, Ryotaro Arita, Yoshichika Otani, and Satoru Nakatsuji. Large anomalous Nernst effect at room temperature in a chiral antiferromagnet. *Nature Physics*, 13(11):1085–1090, 2017.

[70] Guang-Yu Guo and Tzu-Cheng Wang. Large anomalous Nernst and spin Nernst effects in the noncollinear antiferromagnets Mn_3X ($X = \mathrm{Sn}, \mathrm{Ge}, \mathrm{Ga}$). *Physical Review B*, 96(22):224415, dec 2017.

[71] Xiaodong Zhou, Jan-Philipp Hanke, Wanxiang Feng, Stefan Blügel, Yuriy Mokrousov, and Yugui Yao. Giant anomalous Nernst effect in noncollinear antiferromagnetic Mn-based antiperovskite nitrides. *Physical Review Materials*, 4(2):24408, feb 2020.

[72] S. Meyer, Y.-T. Chen, S. Wimmer, M. Althammer, T. Wimmer, R. Schlitz, S. Geprägs, H. Huebl, D. Ködderitzsch, H. Ebert, G. E. W. Bauer, R. Gross, and S. T. B. Goennenwein. Observation of the spin Nernst effect. *Nature Materials*, 16(10):977–981, 2017.

[73] Arnab Bose and Ashwin A. Tulapurkar. Recent advances in the spin Nernst effect. *Journal of Magnetism and Magnetic Materials*, 491:165526, 2019.

[74] K. Uchida, S. Takahashi, K. Harii, J. Ieda, W. Koshibae, K. Ando, S. Maekawa, and E. Saitoh. Observation of the spin Seebeck effect. *Nature*, 455(7214):778–781, 2008.

[75] K. Uchida, J. Xiao, H. Adachi, J. Ohe, S. Takahashi, J. Ieda, T. Ota, Y. Kajiwara, H. Umezawa, H. Kawai, G. E. W. Bauer, S. Maekawa, and E. Saitoh. Spin Seebeck insulator. *Nature Materials*, 9(11):894–897, 2010.

[76] Ken-ichi Uchida, Hiroto Adachi, Takeru Ota, Hiroyasu Nakayama, Sadamichi Maekawa, and Eiji Saitoh. Observation of longitudinal spin-Seebeck effect in magnetic insulators. *Applied Physics Letters*, 97(17):172505, oct 2010.

[77] Hiroto Adachi, Ken-ichi Uchida, Eiji Saitoh, and Sadamichi Maekawa. Theory of the spin Seebeck effect. *Reports on Progress in Physics*, 76(3):36501, 2013.

[78] R. A. Duine, Kyung-Jin Lee, Stuart S. P. Parkin, and M. D. Stiles. Synthetic antiferromagnetic spintronics. *Nature Physics*, 14(3):217–219, 2018.

[79] Takahiro Moriyama, Weinan Zhou, Takeshi Seki, Koki Takanashi, and Teruo Ono. Spin-Orbit-Torque Memory Operation of Synthetic Antiferromagnets. *Physical Review Letters*, 121(16):167202, oct 2018.

[80] Michael S. Ackermann and Satoru Emori. Switching of biaxial synthetic antiferromagnets: A micromagentic study. *Journal of Applied Physics*, 124(22):223901, dec 2018.

[81] Chong Bi, Hamid Almasi, Kyle Price, Ty Newhouse-Illige, Meng Xu, Shane R. Allen, Xin Fan, and Weigang Wang. Anomalous spin-orbit torque switching in synthetic antiferromagnets. *Physical Review B*, 95(10):104434, mar 2017.

[82] G. Y. Shi, C. H. Wan, Y. S. Chang, F. Li, X. J. Zhou, P. X. Zhang, J. W. Cai, X. F. Han, F. Pan, and C. Song. Spin-orbit torque in MgO/CoFeB/Ta/CoFeB/MgO symmetric structure with interlayer antiferromagnetic coupling. *Physical Review B*, 95(10):104435, mar 2017.

[83] R. Q. Zhang, J. Su, J. W. Cai, G. Y. Shi, F. Li, L. Y. Liao, F. Pan, and C. Song. Spin valve effect induced by spin-orbit torque switching. *Applied Physics Letters*, 114(9):92404, mar 2019.

[84] See-Hun Yang, Kwang-Su Ryu, and Stuart Parkin. Domain-wall velocities of up to 750 m/s driven by exchange-coupling torque in synthetic antiferromagnets. *Nature Nanotechnology*, 10(3):221–226, 2015.

[85] Vetle Risinggård and Jacob Linder. Universal absence of Walker breakdown and linear current-velocity relation via spin-orbit torques in coupled and single domain wall motion. *Physical Review B*, 95(13):134423, apr 2017.

[86] T. Newhouse-Illige, Yaohua Liu, M. Xu, D. Reifsnyder Hickey, A. Kundu, H. Almasi, Chong Bi, X. Wang, J. W. Freeland, D. J. Keavney, C. J. Sun,

Y. H. Xu, M. Rosales, X. M. Cheng, Shufeng Zhang, K. A. Mkhoyan, and W. G. Wang. Voltage-controlled interlayer coupling in perpendicularly magnetized magnetic tunnel junctions. *Nature Communications*, 8(1):15232, 2017.

[87] Xichao Zhang, Yan Zhou, and Motohiko Ezawa. Magnetic bilayer-skyrmions without skyrmion Hall effect. *Nature Communications*, 7(1):10293, 2016.

[88] P. Wadley, V. Hills, M. R. Shahedkhah, K. W. Edmonds, R. P. Campion, V. Novák, B. Ouladdiaf, D. Khalyavin, S. Langridge, V. Saidl, P. Nemec, A. W. Rushforth, B. L. Gallagher, S. S. Dhesi, F. Maccherozzi, J. Železný, and T. Jungwirth. Antiferromagnetic structure in tetragonal CuMnAs thin films. *Scientific Reports*, 5(1):17079, 2015.

[89] M. Wang, C. Andrews, S. Reimers, O. J. Amin, P. Wadley, R. P. Campion, S. F. Poole, J. Felton, K. W. Edmonds, B. L. Gallagher, A. W. Rushforth, O. Makarovsky, K. Gas, M. Sawicki, D. Kriegner, J. Zubáč, K. Olejník, V. Novák, T. Jungwirth, M. Shahrokhvand, U. Zeitler, S. S. Dhesi, and F. Maccherozzi. Spin flop and crystalline anisotropic magnetoresistance in CuMnAs. *Physical Review B*, 101(9):94429, mar 2020.

[90] Xiuwen Zhang, Qihang Liu, Jun-Wei Luo, Arthur J. Freeman, and Alex Zunger. Hidden spin polarization in inversion-symmetric bulk crystals. *Nature Physics*, 10(5):387–393, 2014.

[91] V. M. T. S. Barthem, C. V. Colin, H. Mayaffre, M.-H. Julien, and D. Givord. Revealing the properties of Mn2Au for antiferromagnetic spintronics. *Nature Communications*, 4(1):2892, 2013.

[92] Peter Wadley, Sonka Reimers, Michal J. Grzybowski, Carl Andrews, Mu Wang, Jasbinder S. Chauhan, Bryan L. Gallagher, Richard P. Campion, Kevin W. Edmonds, Sarnjeet S. Dhesi, Francesco Maccherozzi, Vit Novak, Joerg Wunderlich, and Tomas Jungwirth. Current polarity-dependent manipulation of antiferromagnetic domains. *Nature Nanotechnology*, 13(5):362–365, 2018.

[93] M. J. Grzybowski, P. Wadley, K. W. Edmonds, R. Beardsley, V. Hills, R. P. Campion, B. L. Gallagher, J. S. Chauhan, V. Novak, T. Jungwirth, F. Maccherozzi, and S. S. Dhesi. Imaging Current-Induced Switching of Antiferromagnetic Domains in CuMnAs. *Physical Review Letters*, 118(5):1–5, 2017.

[94] Sonka Reimers, Dominik Kriegner, Olena Gomonay, Dina Carbone, Filip Krizek, Vit Novák, Richard P. Campion, Francesco Maccherozzi, Alexander Björling, Oliver J. Amin, Luke X. Barton, Stuart F. Poole, Khalid A. Omari, Jan Michalička, Ondřej Man, Jairo Sinova, Tomáš Jungwirth, Peter Wadley, Sarnjeet S. Dhesi, and Kevin W. Edmonds. Defect-driven antiferromagnetic domain walls in CuMnAs films. *Nature Communications*, 13(1):724, 2022.

[95] K. Olejník, V. Schuler, X. Marti, V. Novák, Z. Kašpar, P. Wadley, R. P. Campion, K. W. Edmonds, B. L. Gallagher, J. Garces, M. Baumgartner, P. Gambardella, and T. Jungwirth. Antiferromagnetic CuMnAs multi-level memory cell with microelectronic compatibility. *Nature Communications*, 8(1):15434, 2017.

[96] Kamil Olejník, Tom Seifert, Zdenek Kašpar, Vít Novák, Peter Wadley, Richard P. Campion, Manuel Baumgartner, Pietro Gambardella, Petr Nemec, Joerg Wunderlich, Jairo Sinova, Petr Kužel, Melanie Müller, Tobias Kampfrath, and Tomas Jungwirth. Terahertz electrical writing speed in an antiferromagnetic memory. *Science Advances*, 4(3):eaar3566, mar 2018.

[97] K. A. Omari, L. X. Barton, O. Amin, R. P. Campion, A. W. Rushforth, A. J. Kent, P. Wadley, and K. W. Edmonds. Low-energy switching of antiferromagnetic CuMnAs/GaP using sub-10 nanosecond current pulses. *Journal of Applied Physics*, 127(19):193906, may 2020.

[98] Z. Kašpar, M. Surýnek, J. Zubáč, F. Krizek, V. Novák, R. P. Campion, M. S. Wörnle, P. Gambardella, X. Marti, P. Němec, K. W. Edmonds, S. Reimers, O. J. Amin, F. Maccherozzi, S. S. Dhesi, P. Wadley, J. Wunderlich, K. Olejník, and T. Jungwirth. Quenching of an antiferromagnet into high resistivity states using electrical or ultrashort optical pulses. *Nature Electronics*, 4(1):30–37, 2021.

[99] Filip Krizek, Sonka Reimers, Zdeněk Kašpar, Alberto Marmodoro, Jan Michalička, Ondřej Man, Alexander Edström, Oliver J. Amin, Kevin W. Edmonds, Richard P. Campion, Francesco Maccherozzi, Samjeet S. Dhesi, Jan Zubáč, Dominik Kriegner, Dina Carbone, Jakub Železný, Karel Výborný, Kamil Olejník, Vít Novák, Jan Rusz, Juan Carlos Idrobo, Peter Wadley, and Tomas Jungwirth. Atomically sharp domain walls in an antiferromagnet. *Science Advances*, 8(13):eabn3535, mar 2022.

[100] T. Nagamiya, S. Tomiyoshi, and Y. Yamaguchi. Triangular spin configuration and weak ferromagnetism of Mn3Sn and Mn3Ge. *Solid State Communications*, 42(5):385–388, 1982.

[101] Shōichi Tomiyoshi. Polarized Neutron Diffraction Study of the Spin Structure of Mn3Sn. *Journal of the Physical Society of Japan*, 51(3):803–810, mar 1982.

[102] Gautam Gurung, Ding-Fu Shao, Tula R. Paudel, and Evgeny Y. Tsymbal. Anomalous Hall conductivity of noncollinear magnetic antiperovskites. *Physical Review Materials*, 3(4):44409, apr 2019.

[103] Xiaokang Li, Liangcai Xu, Linchao Ding, Jinhua Wang, Mingsong Shen, Xiufang Lu, Zengwei Zhu, and Kamran Behnia. Anomalous Nernst and Righi-Leduc Effects in Mn_3Sn: Berry Curvature and Entropy Flow. *Physical Review Letters*, 119(5):56601, aug 2017.

[104] Girish Sharma, Pallab Goswami, and Sumanta Tewari. Nernst and magnetothermal conductivity in a lattice model of Weyl fermions. *Physical Review B*, 93(3):35116, jan 2016.

[105] Hao Yang, Yan Sun, Yang Zhang, Wu-Jun Shi, Stuart S. P. Parkin, and Binghai Yan. Topological Weyl semimetals in the chiral antiferromagnetic materials Mn3Ge and Mn3Sn. *New Journal of Physics*, 19(1):15008, 2017.

[106] Jakub Železný, Yang Zhang, Claudia Felser, and Binghai Yan. Spin-Polarized Current in Noncollinear Antiferromagnets. *Physical Review Letters*, 119(18):187204, nov 2017.

[107] Peixin Qin, Han Yan, Xiaoning Wang, Hongyu Chen, Ziang Meng, Jianting Dong, Meng Zhu, Jialin Cai, Zexin Feng, Xiaorong Zhou, Li Liu, Tianli Zhang, Zhongming Zeng, Jia Zhang, Chengbao Jiang, and Zhiqi Liu. Room-temperature magnetoresistance in an all-antiferromagnetic tunnel junction. *Nature*, 613(7944):485–489, 2023.

[108] Xianzhe Chen, Tomoya Higo, Katsuhiro Tanaka, Takuya Nomoto, Hanshen Tsai, Hiroshi Idzuchi, Masanobu Shiga, Shoya Sakamoto, Ryoya Ando, Hidetoshi Kosaki, Takumi Matsuo, Daisuke Nishio-Hamane, Ryotaro Arita, Shinji Miwa, and Satoru Nakatsuji. Octupole-driven magnetoresistance in an antiferromagnetic tunnel junction. *Nature*, 613(7944):490–495, 2023.

[109] Junyeon Kim, Jaivardhan Sinha, Masamitsu Hayashi, Michihiko Yamanouchi, Shunsuke Fukami, Tetsuhiro Suzuki, Seiji Mitani, and Hideo Ohno. Layer thickness dependence of the current-induced effective field vector in Ta—CoFeB—MgO. *Nature Materials*, 12(3):240–245, 2013.

[110] Masamitsu Hayashi, Junyeon Kim, Michihiko Yamanouchi, and Hideo Ohno. Quantitative characterization of the spin-orbit torque using harmonic Hall voltage measurements. *Phys. Rev. B*, 89(14):144425, apr 2014.

[111] H. Reichlová, D. Kriegner, V. Holý, K. Olejník, V. Novák, M. Yamada, K. Miura, S. Ogawa, H. Takahashi, T. Jungwirth, and J. Wunderlich. Current-induced torques in structures with ultrathin IrMn antiferromagnets. *Phys. Rev. B*, 92(16):165424, oct 2015.

[112] J. Grollier, D. Querlioz, K. Y. Camsari, K. Everschor-Sitte, S. Fukami, and M. D. Stiles. Neuromorphic spintronics. *Nature Electronics*, 3(7):360–370, 2020.

[113] Steven Lequeux, Joao Sampaio, Vincent Cros, Kay Yakushiji, Akio Fukushima, Rie Matsumoto, Hitoshi Kubota, Shinji Yuasa, and Julie Grollier. A magnetic synapse: multilevel spin-torque memristor with perpendicular anisotropy. *Scientific Reports*, 6(1):31510, 2016.

[114] J. Godinho, H. Reichlová, D. Kriegner, V. Novák, K. Olejník, Z. Kašpar, Z. Šobáň, P. Wadley, R. P. Campion, R. M. Otxoa, P. E. Roy, J. Železný, T. Jungwirth, and J. Wunderlich. Electrically induced and detected Néel vector reversal in a collinear antiferromagnet. *Nature Communications*, 9(1):4686, dec 2018.

[115] Takahiro Moriyama, Kent Oda, Takuo Ohkochi, Motoi Kimata, and Teruo Ono. Spin torque control of antiferromagnetic moments in NiO. *Scientific Reports*, 8(1):14167, 2018.

[116] S. Yu. Bodnar, M. Filianina, S. P. Bommanaboyena, T. Forrest, F. Maccherozzi, A. A. Sapozhnik, Y. Skourski, M. Kläui, and M. Jourdan. Imaging of current induced Néel vector switching in antiferromagnetic Mn_2Au. *Physical Review B*, 99(14):140409, apr 2019.

[117] M. S. Wörnle, P. Welter, Z. Kašpar, K. Olejník, V. Novák, R. P. Campion, P. Wadley, T. Jungwirth, C. L. Degen, and P. Gambardella. Current-induced fragmentation of antiferromagnetic domains, 2019.

[118] Mathias Weiler, Matthias Althammer, Franz D. Czeschka, Hans Huebl, Martin S. Wagner, Matthias Opel, Inga-Mareen Imort, Günter Reiss, Andy Thomas, Rudolf Gross, and Sebastian T. B. Goennenwein. Local Charge and Spin Currents in Magnetothermal Landscapes. *Physical Review Letters*, 108(10):106602, mar 2012.

[119] David Richards, Anatoly Zayats, Fritz Keilmann, and Rainer Hillenbrand. Near-field microscopy by elastic light scattering from a tip. *Philosophical Transactions of the Royal Society of London. Series A: Mathematical, Physical and Engineering Sciences*, 362(1817):787–805, apr 2004.

[120] E. Pfitzner, X. Hu, H. W. Schumacher, A. Hoehl, D. Venkateshvaran, M. Cubukcu, J.-W. Liao, S. Auffret, J. Heberle, J. Wunderlich, and B. Kästner. Near-field magneto-caloritronic nanoscopy on ferromagnetic nanostructures. *AIP Advances*, 8(12):125329, dec 2018.

[121] T. Janda, J. Godinho, T. Ostatnicky, E. Pfitzner, G. Ulrich, A. Hoehl, S. Reimers, Z. Šobáň, T. Metzger, H. Reichlová, V. Novák, R. P. Campion, J. Heberle, P. Wadley, K. W. Edmonds, O. J. Amin, J. S. Chauhan, S. S. Dhesi, F. Maccherozzi, R. M. Otxoa, P. E. Roy, K. Olejník, P. Němec, T. Jungwirth, B. Kaestner, and J. Wunderlich. Magneto-Seebeck microscopy of domain switching in collinear antiferromagnet CuMnAs. *Physical Review Materials*, 4(9):94413, sep 2020.

[122] J. Wunderlich, D. Ravelosona, C. Chappert, F. Cayssol, V. Mathet, J. Ferre, J. P. Jamet, and A. Thiaville. Influence of geometry on domain wall propagation in a mesoscopic wire. *IEEE Transactions on Magnetics*, 37(4):2104–2107, 2001.

[123] T. Janda, P. E. Roy, R. M. Otxoa, Z. Šobáň, A. Ramsay, A. C. Irvine, F. Trojanek, M. Surýnek, R. P. Campion, B. L. Gallagher, P. Němec, T. Jungwirth, and J. Wunderlich. Inertial displacement of a domain wall excited by ultra-short circularly polarized laser pulses. *Nature Communications*, 8(1):15226, 2017.

[124] V. Saidl, P. Němec, P. Wadley, V. Hills, R. P. Campion, V. Novák, K. W. Edmonds, F. Maccherozzi, S. S. Dhesi, B. L. Gallagher, F. Trojánek, J. Kuneš, J. Železný, P. Malý, and T. Jungwirth. Optical determination of the Néel vector in a CuMnAs thin-film antiferromagnet. *Nature Photonics*, 11(2):91–96, 2017.

[125] Helena Reichlova, Tomas Janda, Joao Godinho, Anastasios Markou, Dominik Kriegner, Richard Schlitz, Jakub Zelezny, Zbynek Soban, Mauricio Bejarano, Helmut Schultheiss, Petr Nemec, Tomas Jungwirth, Claudia Felser, Joerg Wunderlich, and Sebastian T. B. Goennenwein. Imaging and writing magnetic domains in the non-collinear antiferromagnet Mn3Sn. *Nature Communications*, 10(1):5459, 2019.

[126] Satoshi Sugimoto, Yoshinobu Nakatani, Yuta Yamane, Muhammad Ikhlas, Kouta Kondou, Motoi Kimata, Takahiro Tomita, Satoru Nakatsuji, and Yoshichika Otani. Electrical nucleation, displacement, and detection of antiferromagnetic domain walls in the chiral antiferromagnet Mn3Sn. *Communications Physics*, 3(1):111, 2020.

[127] A. Slavin and V. Tiberkevich. Nonlinear Auto-Oscillator Theory of Microwave Generation by Spin-Polarized Current. *IEEE Transactions on Magnetics*, 45(4):1875–1918, 2009.

[128] Benjamin Wolba, Olena Gomonay, and Volodymyr P. Kravchuk. Chaotic antiferromagnetic nano-oscillator driven by spin torque. *Physical Review B*, 104(2):24407, jul 2021.

[129] M. Merte, F. Freimuth, D. Go, T. Adamantopoulos, F. R. Lux, L. Plucinski, O. Gomonay, S. Blügel, and Y. Mokrousov. Photocurrents, inverse Faraday effect and photospin Hall effect in Mn_2Au, 2023.

List of Figures

List of Abbreviations

AFM	Antiferromagnet
AHE	Anomalous Hall effect
AMR	Anisotropic magnetoresistance
ANE	Anomalous Nernst effect
cAFM	collinear Antiferromagnet
FM	Ferromagnet
GMR	Giant Magnetoresistance
MSE	Magneto-Seebeck effect
ncAFM	noncollinear Antiferromagnet
SAF	Synthetic Antiferromagnet
SFOM	Scanning far-field optical microscopy
SHE	Spin Hall effect
SNOM	Scanning near-field optical microscopy
SOT	Spin-Orbit Torque
STT	Spin-Transfer Torque

List of publications

1. D. Kriegner, H. Reichlova, J. Grenzer, W. Schmidt, E. Ressouche, J. Godinho, T. Wagner, S. Y. Martin, A. B. Shick, V. V. Volobuev, G. Springholz, V. Holý, J. Wunderlich, T. Jungwirth, K. Výborný, **Magnetic anisotropy in antiferromagnetic hexagonal MnTe**, Physical Review B 96, 214418 (2017)

2. J. Godinho, H. Reichlová, D. Kriegner, V. Novák, K. Olejník, Z. Kašpar, Z. Šobáň, P. Wadley, R. P. Campion, R. M. Otxoa, P. E. Roy, J. Železný, T. Jungwirth, J. Wunderlich, **Electrically induced and detected Néel vector reversal in a collinear antiferromagnet**, Nature Communications 9, 4686 (2018)

3. H. Reichlova, T. Janda, J. Godinho, A. Markou, D. Kriegner, R. Schlitz, J. Zelezny, Z. Soban, M. Bejarano, H. Schultheiss, P. Nemec, T. Jungwirth, C. Felser, J. Wunderlich, S. T. B. Goennenwein, **Imaging and writing magnetic domains in the non-collinear antiferromagnet Mn3Sn**, Nature Communications 10, 5459 (2019)

4. T. Janda, J. Godinho, T. Ostatnicky, E. Pfitzner, G. Ulrich, A. Hoehl, S. Reimers, Z. Šobáň, T. Metzger, H. Reichlová, V. Novák, R. P. Campion, J. Heberle, P. Wadley, K. W. Edmonds, O. J. Amin, J. S. Chauhan, S. S. Dhesi, F. Maccherozzi, R. M. Otxoa, P. E. Roy, K. Olejník, P. Němec, T. Jungwirth, B. Kaestner, J. Wunderlich, **Magneto-Seebeck microscopy of domain switching in collinear antiferromagnet CuMnAs**, Physical Review Materials 4, 94413 (2020)

5. R. M. Otxoa, P. E. Roy, R. Rama-Eiroa, J. Godinho, K. Y. Guslienko, J. Wunderlich, **Walker-like domain wall breakdown in layered antiferromagnets driven by staggered spin–orbit fields**, Communications Physics 3, 190 (2020)

6. F. Johnson, J. Kimák, J. Zemen, Z. Šobáň, E. Schmoranzerová, J. Godinho, P. Němec, S. Beckert, H. Reichlová, D. Boldrin, J. Wunderlich, L. F. Cohen, **Identifying the octupole antiferromagnetic domain orientation in Mn3NiN by scanning anomalous Nernst effect microscopy**, Applied Physics Letters 120, 232402 (2022)

7. S. Beckert, J. Godinho, F. Johnson, J. Kimák, E. Schmoranzerová, J. Zemen, Z. Šobáň, K. Olejník, J. Železný, J. Wunderlich, P. Němec, D. Kriegner, A. Thomas, S. T. B. Goennenwein, L. F. Cohen, H. Reichlová, **Anomalous Nernst effect in Mn_3NiN thin films**, submitted to Physical Review B

8. J. Godinho, P. K. Rout, R. Salikhov, O. Hellwig, Z. Šobáň, R. M. Otxoa, K. Olejník, T. Jungwirth, and J. Wunderlich, **Non-Volatile Spin-Orbit Torque Driven Antiferromagnetic Memristor**, in preparation